# Silicon Isotope Investigation of Low Temperature Authigenic Siliceous Deposits and High Temperature Planetary Materials

A Dissertation Presented to

the Faculty of the Department of Earth and Atmospheric Sciences

University of Houston

In Partial Fulfillment

of the Requirements for the Degree of

Doctor of Philosophy

By

Xinyang Chen

August 2016

# Silicon Isotope Investigation of Low Temperature Authigenic Siliceous Deposits and High Temperature Planetary Materials

Xinyang Chen

APPROVED:

Dr. Henry S. Chafetz, Chairman

Dr. Thomas J. Lapen

Dr. Qi Fu

Dr. Patrick Rush
Core Laboratories

Dr. Dan Wells
Dean, College of Natural Sciences and Mathematics

# Acknowledgements

This work would not have happened without the support and encouragement from numerous individuals over the past five years. First, and foremost, I would like to thank my supervisor Henry Chafetz, I am deeply indebted to him for the scientific discussions, numerous corrections and guidance I have enjoyed over the years. I am grateful to Tom Lapen, Rasmus Anderesen, and Minako Righter who taught me a great deal about isotope measurements and column chemistry. I would like to thank Patrick Rush and Qi Fu for being part of my Ph.D. committee and giving me great advice. I express my gratitude to James Meen and Karoline Mueller at the Texas Center for Superconductivity for the training and guidance for X-ray diffraction and SEM analyses. I thank my fellow graduate students and the entire Earth and Atmospheric Sciences department for all the support. Finally, this dissertation is dedicated to my family, especially my wife Xi, without whom none of this would have happened.

# Silicon Isotope Investigation of Low Temperature Authigenic Siliceous Deposits and High Temperature Planetary Materials

An Abstract of a Dissertation

Presented to

the Faculty of the Department of Earth and Atmospheric Sciences

University of Houston

In Partial Fulfillment

of the Requirements for the Degree of

Doctor of Philosophy

By

Xinyang Chen

August 2016

# Abstract

Despite the ubiquity of the element silicon (Si) in silicate rocks and minerals, there is still no clear understanding of how the Si isotopes fractionate during Earth's surface processes (e.g., the formation of low temperature siliceous deposits) and during early Solar System processes (e.g., nebular differentiation and metal-silicate differentiation). With recent advances in analytical techniques, the analytical precision has been greatly improved, which allows straightforward determination of Si isotope variations during both low and high temperature fractionations.

The first part of this study investigates the petrogenesis and paleoenvironments of Phanerozoic siliceous deposits using a suite of euhedral megaquartz crystals in the Cretaceous Edwards Formation from Central Texas. Si isotopic mapping across the megaquartz crystals show that $\delta^{30}Si_{(NBS\ 28)}$ values range from -2.72 to +2.94 ‰. The range of $\delta^{30}Si$ values in megaquartz crystals is interpreted using a two stage model in which amorphous silica from sponge spicules is dissolved and re-precipitated as megaquartz in a closed system during diagenesis. Based on temperature estimates of 23 to 30 °C for megaquartz precipitation, the fractionation factor was determined to be between -0.95 to -1.46 ‰. The estimated average $\delta^{30}Si$ value of the Late Cretaceous seawaters is +2.3 to +2.8 ‰, significantly higher than modern seawater.

The second part of the study investigates the Si isotope compositions of a unique ungrouped achondrite NWA 7325 and a suite of other meteorite and terrestrial rock samples to better understand Si isotopic variation in planetary materials and the relationship

between NWA 7325 and other meteorite groups. NWA 7325 is a reduced, Mg-rich cumulate olivine gabbro that was thought to have originated from planet Mercury. The $\delta^{30}Si$ value of NWA 7325 is -0.45±0.05 ‰ (n=8), indistinguishable from chondrites. Bulk silicate Earth (BSE) and angrites have higher $\delta^{30}Si$ values than chondrites, which is better explained by nebular fractionation rather than core formation. The difference in $\delta^{30}Si$ values between planetary materials could be caused by variable forsterite and nebular gas mixing. NWA 7325 may have accreted from materials that inherited similar proportions of early gas and condensates as chondrites, but distinct from those of the angrite and the Earth-Moon system.

# Contents

# List of figures

# List of tables

# Chapter 1

# Introduction

## 1.1 Stable Si isotopes

Silicon (Si) is the second most abundant element in the Earth's crust, after oxygen. Continental crust contains around 28 wt.% Si on average (Rudnick and Gao, 2014) with the upper crust slightly enriched due to the interaction with the more evolved biosphere. From the wider perspective, it is the eighth most abundant element in the solar system. Si has three stable isotopes: $^{28}$Si, $^{29}$Si, and $^{30}$Si with the average abundance of 92.23%, 4.68% and 3.09%, respectively.

Despite the ubiquity of Si, the application of stable silicon isotopic analysis ($^{28}$Si, $^{29}$Si, and $^{30}$Si) has gained more interest during the last two decades. Early studies during the 50's and 60' discovered very limited fractionation of Si isotopes in natural samples. Douthitt (1982) conducted silicon isotope analyses in great detail on terrestrial samples from various environments and demonstrated systematic differences between silica-rich materials. Ding et al. (1996) compiled data for more than 1000 geologic samples and summarized that the ($\delta^{30}$Si) values range from -3.4 ‰ to +3.4 ‰. Most of the early work has been done using gas-source mass spectrometry (GS-MS). Recent advances in analytical techniques, especially the advent of multi-collector inductively coupled-plasma mass spectrometry (MC-ICP-MS) have greatly improved the analytical precision and expanded the application of stable Si isotopes in geology and biogeochemistry.

## 1.2 Si isotopes in sedimentary rocks and global Si cycle

Basile-Doelsch et al. (2005) reported strongly $^{30}Si$ depleted silcretes with a $\delta^{30}Si$ value as low as -5.7 ‰, whereas Ding et al. (2005) reported $\delta^{30}Si$ values as high as +6.1 ‰ in rice grains. Isotopic ratios show significant variations in a wide range of environments, allowing the use of silicon isotopes as a diagnostic tracer for depositional settings of silica-rich rocks and for aiding in determining the origin of the silica (Basile-Doelsch, 2006).

Previous studies have used Si isotopes to trace the origin of Archean and Proterozoic chert and the geochemistry of the Precambrian Ocean (Robert and Chaussidon, 2006; van den Boorn et al., 2010; Chakrabarti et al., 2012; Marin-Carbonne et al., 2012). Robert and Chaussidon (2006) reported that sea water temperature changes from about 70 °C in the early Archaean to about 20 °C 800 million years ago based on oxygen and silicon isotopes. Heck et al. (2011) combined *in situ* silicon and oxygen isotope analyses for quartz from banded iron formations (BIF) and found that $\delta^{30}Si$ of BIF quartz varies on the microscale, whereas the $\delta^{18}O$ values in individual samples are more homogeneous. This indicated that metamorphism probably reset oxygen isotopic composition in BIF quartz and that silicon isotopes are less susceptible to metamorphic exchange. Chakrabarti et al. (2012) reported a wide range of $\delta^{30}Si$ in Precambrian chert samples (-4.29 to +2.85 ‰) and suggested a Rayleigh type kinetic isotope fractionation model. $\delta^{30}Si$ values can be used to delineate chert that has precipitated from seawater compared to hydrothermal chert (van den Boorn et al., 2007, 2010).

In addition to those studies of ancient cherts, there has been a growing interest in the study of Si isotopes in modern samples because of the close link of Si to other elements in global biogeochemical cycles. Silicon isotopic compositions have been measured in a

wide range of natural samples that include dissolved and biogenic (diatom and sponge) silica from marine and fresh waters (De La Rocha et al., 1997, 2000; De La Rocha, 2003; Ding et al., 2005; Fripiat et al., 2007; Georg et al., 2009; Hendry et al., 2010; Ding et al., 2011), soils and silcrete (Basile-Doelsch et al., 2005; Opfergelt et al., 2009; Steinhoefel et al., 2011), as well as silica secreting plants (Ding et al., 2005; Opfergelt et al., 2006). Furthermore, experimental studies have been carried out to understand the mechanism and factors that control Si isotopes fractionation during precipitation and dissolution (Demarest et al., 2009; Geilert et al., 2014; Oelze et al., 2014; Wetzel et al., 2014).

The dominant influx of dissolved silicic acid to the modern ocean is the product of continental weathering and it is transported in river waters, which have an average $\delta^{30}$Si value of +0.8 ‰ (De La Rocha et al., 2000) (Fig. 1.1). Bulk igneous rocks show small variation in $\delta^{30}$Si values with an average of -0.3 ‰ (Douthitt, 1982; Ding et al., 1996; Savage et al., 2010). This led to the discovery of low $\delta^{30}$Si pools on the continent, namely, the clay minerals from weathering process (Ding et al., 1996) and pedogenic silcretes (Basile-Doelsch et al., 2005). Lighter Si isotopes react faster in chemical weathering of silicates therefore secondary clay minerals are usually $^{30}$Si-depleted. Experimental determination of Si isotope fractionation between kaolinite and quartz at 27 °C is estimated at -1.6 ‰ (Méheut et al., 2007), which is consistent with our modeled range. Hydrothermal fluids and seafloor basalt weathering represent other major contributors (Tréguer et al., 1995). $\delta^{30}$Si values for modern hydrothermal fluids from the East Pacific Rise (De La Rocha et al., 2000) are almost identical to those of terrestrial igneous rocks, whereas the siliceous deposits from hydrothermal systems show very negative $\delta^{30}$Si values similar to siliceous sinter deposits from continental hot springs, which can be explained by Rayleigh-

type kinetic fractionation due to the large drop in temperature around hydrothermal spring orifices (Ding et al., 1996).

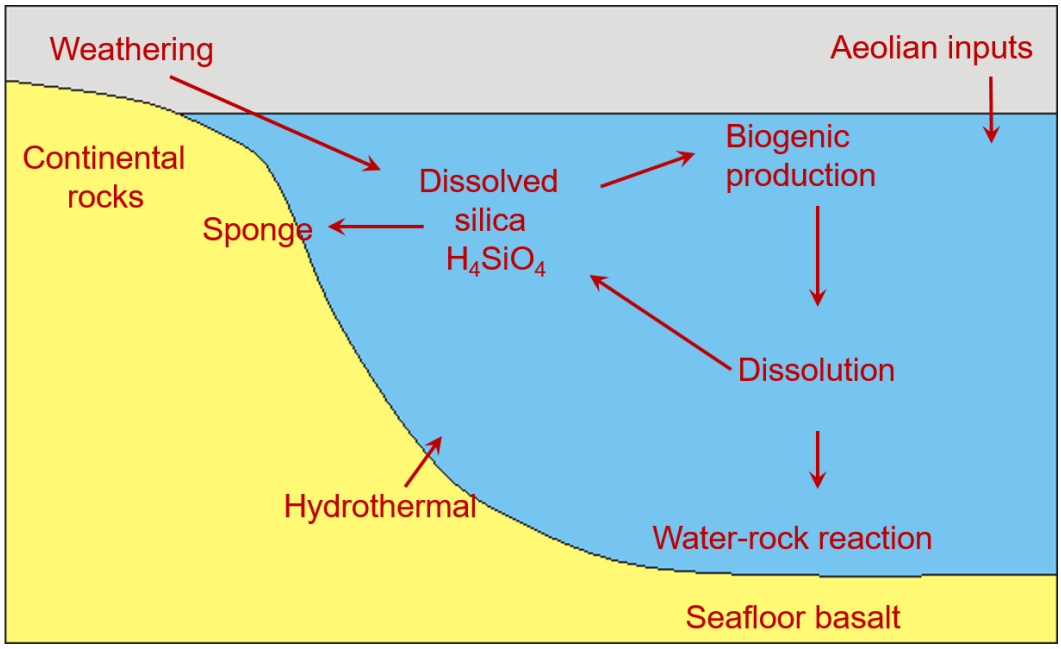


**Figure 1.1**: Global Si cycle. The arrows represent the Si fluxes between different Si pools.

In the modern ocean, dissolved Si is present in the form of silicic acid ($H_4SiO_4$). Marine silica-secreting organisms, particularly diatoms utilize the dissolved Si in seawater in assembling their opaline skeletons (Fig. 1.1). The mean $\delta^{30}$Si value of modern seawater estimated by De La Rocha et al. (2000) is +1.1 ‰. Because most diatoms live in the photic zone, the surface waters in modern oceans are strongly undersaturated. The biologic uptake of Si discriminates against the heavier isotopes. The fractionation factor between biologic opal and the dissolved silicic acid was estimated to be -1 ‰ for diatoms and -3.8 ‰ for marine sponges (De La Rocha et al., 1997; De La Rocha, 2003). It is also been documented

that the biologic uptake of Si is dependent on the concentration of $H_4SiO_4$ with greater fractionation in higher concentrations (Hendry and Robinson, 2012). Average concentration of $H_4SiO_4$ in modern oceanwater is only 2 ppm, largely due to the draw down by diatoms (Tréguer et al., 1995). In contrast, Mesozoic oceans probably contained much higher concentrations of $H_4SiO_4$ as diatoms first appeared during the Jurassic and did not evolve to become the dominant marine producer of Si until the Oligocene (Wells, 1983; De La Rocha, 2007). It is conceivable that a sponge dominated marine environment would have produced a different Si isotopic signature in biogenic silica.

## 1.3 Si isotopes in meteorites

### 1.3.1 Planet formation process

Nucleosyntheses inside stars and supernovae are responsible for creating elements and isotopes heavier than hydrogen. The explosion of earlier formed stars and supernovae eject these elements and isotopes as gas and dust into the interstellar medium forming dense molecular cloud. The gravitational collapse of one such molecular cloud led to the formation of our solar system. The center of the cloud is heated to form the proto-sun. The gravitational contraction and the rotation makes the surrounding nebula flatten into a disc shape. Planets formed from the disc-shaped cloud of gas and dust left over after the Sun's formation. The planets began as tiny dust grains coagulating and settling out of the midplane of the protoplanetary disc. This is accompanied with a number of processes, including evaporation, condensation, and melting, which led to the formation of refractory calcium-aluminum rich inclusions (CAIs) and chondules. These early objects, upon further

colliding, form larger planetesimals, which then accreted to form planets through gravitation in a run-away fashion (Fig. 1.2). During the formation of planets, the heat from gravitation collapse and short-lived radionuclides decay caused melting and differentiation of silicates from the metal.

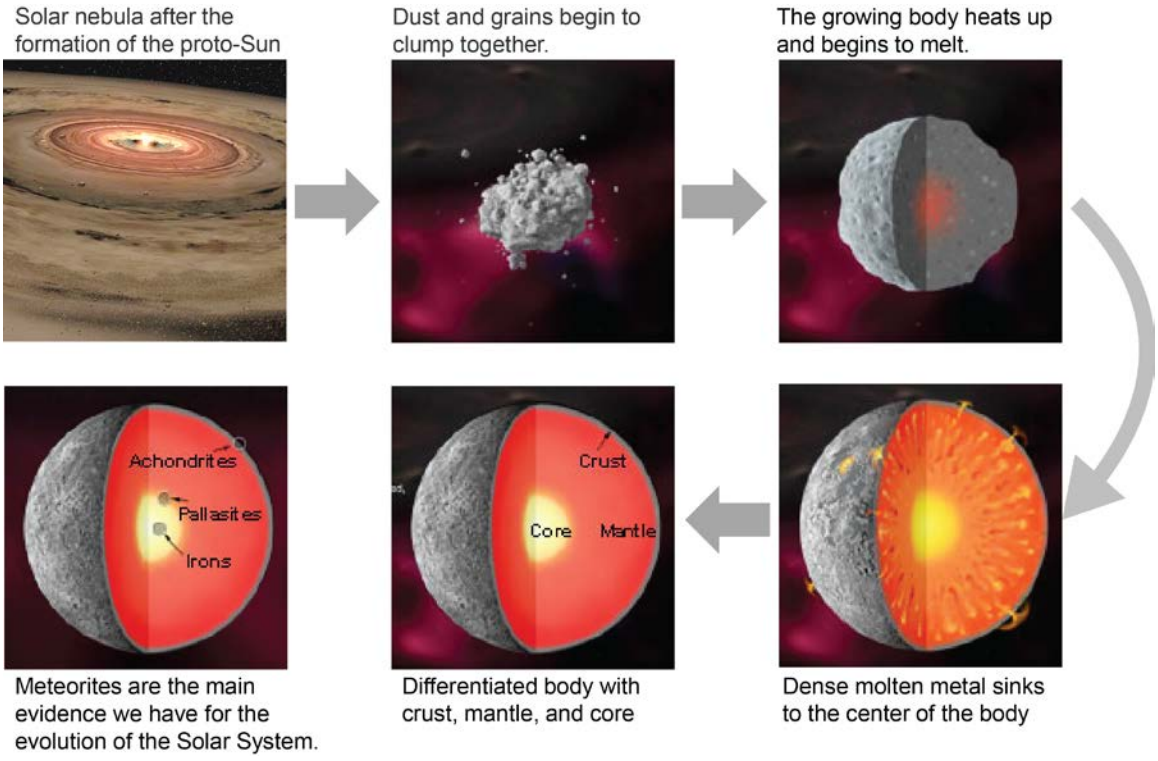


**Figure 1.2**: Planet formation processes. Images courtesy of Smithsonian National Musuem of Natural history.

### 1.3.2 Classification of meteorites

Meteorites, solid extraterrestrial material that fall on Earth, are often classified into two categories by composition and texture: chondrites and nonchondritic meteorites (Krot et al., 2014). Non-chondritic meteorites are further divided into achondrites, iron, and stony iron meteorites (Fig. 1.3).

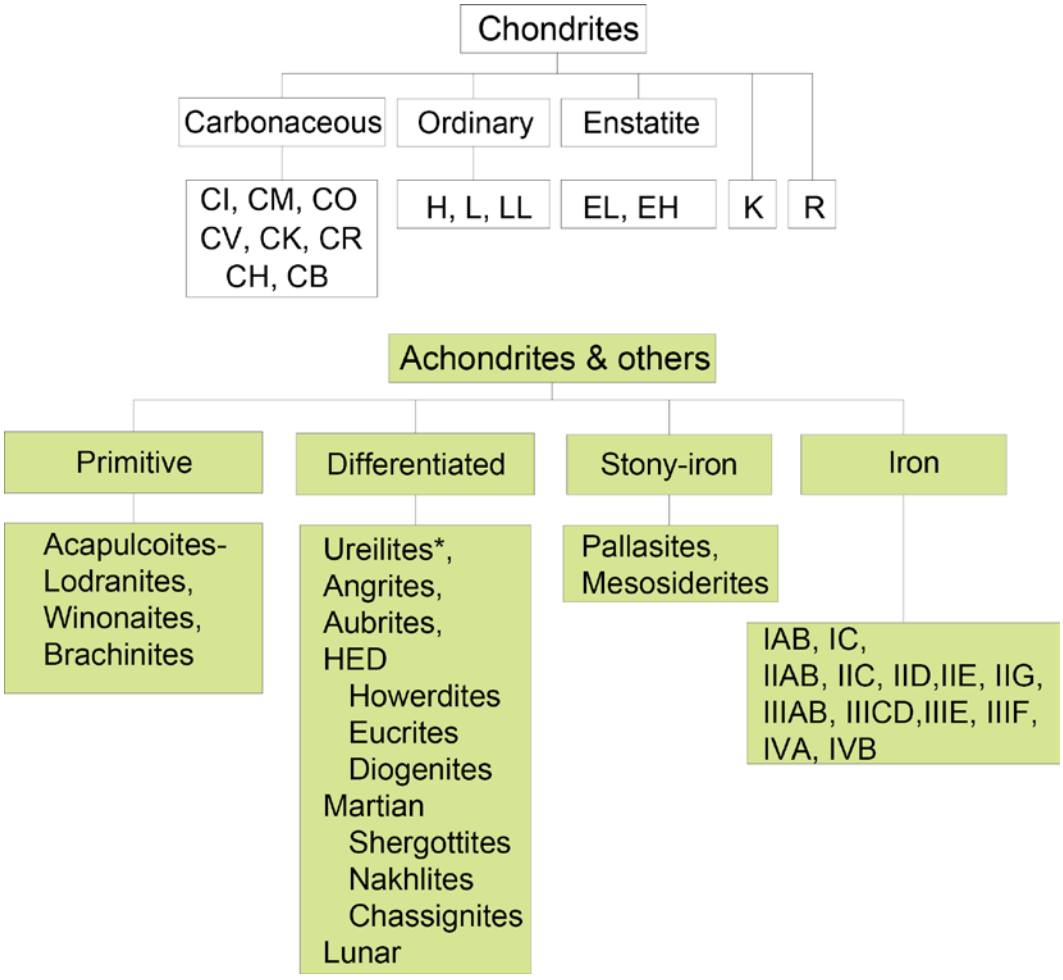


**Figure 1.3**: Classification of meteorites based on texture and bulk composition (Krot et al., 2014). The asterisk designated groups are sometimes also classified as primitive achondrites.

Chondrites, as the name implies, contain chondules, solidified partially or complete molten silicate spherules. Other components in chondrites include CAIs, metal, sulfides, and matrix. Although most chondrites have experienced thermal alteration processes in their parent asteroids, these meteorites have not undergone melting and igneous differentiation and thus preserves the physical and chemical characteristics of the solar nebula.

Nonchondritic meteorites lack chondules. These meteorites formed from partial or complete melting and planetary differentiation of chondritic precursors or large planets. Achondrites represent the silicate portion, whereas iron meteorites are thought to represent the metal portion of a differentiated parent body. Stony iron meteorites are mixtures of metal and silicates. Detailed classification of achondrites is provided in Chapter 5.

## 1.4 Motivation for this study

The aims of this dissertation were to reappraise some of the caveats of the Si isotope analysis methods proposed by Georg et al. (2006), establish accurate and precise analytical routines, regardless of the sample matrix and apply it to both low and high temperature geochemistry. These goals were achieved by conducting the following studies:

Chapter 3: It has not been conclusive whether the presence of some matrix species, particularly sulfur (S) in the sample solution could compromise the accuracy of Si isotope analysis. The aims of the study covered in this chapter are to test whether S-doping can yield accurate and precise Si isotope ratio measurements of terrestrial and extraterrestrial samples with variable S/Si ratios. Sample preparation and analytical methods are proposed that seem to eliminate potential issues with variable S/Si ratios in measured Si solutions and address the issue of Fe hydroxide precipitation that fractionates Si in sample solutions

before cation-exchange ion chromatography. These methods have been successfully applied to a variety of well characterized samples and standards.

Chapter 4: This chapter combines laser ablation (LA) *in situ* and solution-based bulk Si isotope analyses on doubly terminated authigenic euhedral megaquartz crystals collected from the Cretaceous Edwards Formation at Lake Georgetown Spillway, central Texas, to better understand the paleoenvironmental conditions during the euhedral authigenic quartz crystals formation. Further, a two-stage Rayleigh-type kinetic model was used to constrain abiotic Si isotope fractionation factors during quartz formation. The results showed that the Cretaceous ocean waters have higher $\delta^{30}$Si value than the modern seawater.

Chapter 5: A suite of meteorite samples, including the unique ungrouped achondrite NWA 7325 were measured to better constrain its origin and its implications for early solar system processes. The results support the hypothesis that nebular fractionation rather than metal-silicate differentiation is most likely responsible for the variations of Si isotopic compositions in the inner solar system. NWA 7325 has chondritic bulk Si isotopic values, suggesting it may have originated from the asteroid belt.

# Chapter 2

# Analytical method

## 2.1 Introduction

Silicon (Si) is a major element in Earth's mantle and crust. However, the application of stable silicon isotopic analysis has only become a routine geochemical technique in the last two decades. Early pioneering works used complex extraction procedures and highly hazardous chemicals (e.g., $F_2$ and $BrF_5$), which requires large quantities of samples and are not ideal. These studies were based on gas source mass spectrometry (GS-MS) that requires volatile Si species (e.g., $SiF_3^+$) be introduced in the mass spectrometer, which was done by converting silicate to $BaSiF_6$ and subsequently decomposing to $SiF_4$ (Reynold and Verhoogen, 1953) or by in-line direct fluorination. Several fluorination reagents were utilized, including HF (Allenby, 1954), a mixture of HF and $F_2$ (Taylor and Epstein, 1970), and $BrF_5$ (Clayton et al., 1974).

The precision of these early Si isotope studies were 0.15 to 0.6 ‰, which was insufficient to resolve any sub per mil variations. It became clear that the natural variation in Si isotopic composition is rather small, which requires high precision mass spectrometry. Douthitt (1982) was the first to conduct silicon isotope analyses in great detail on terrestrial samples from various environments and demonstrated systematic differences between silica-rich materials. The constant improvement in the precision using GS-MS (Ding et al., 1996; De La Rocha and Brzezinski, 1996) has contributed to continuous interest in Si isotope analysis, especially in dissolved and biogenic silica in waters (De La Rocha et al.,

1996, 2000; Ding et al., 2005). However, converting $SiO_2$ to gaseous $SiF_4$ involves complex extraction system and dangerous gases such as $F_2$.

Recent advances in multi-collector inductively coupled plasma mass spectrometry (MC-ICP-MS) have made Si isotopic measurements faster and more reliable than using GS-MS while maintaining similar precision. Sample extraction techniques such as HF digestion (De La Rocha, 2002; Cardinal et al., 2003), NaOH Parr Bomb digestion (van den Boorn et al., 2006), and NaOH fusion (Georg et al., 2006) have been used in combination with column chemistry. The plasma source is capable of ionize most elements regardless of the species, which made the NaOH extraction technique more desirable as it avoids the use of dangerous chemicals. In addition, using HF for sample digestion introduces fluorine (F) into the mass spectrometer, which has a high $1^{st}$ ionization potential that will suppress the ionization efficiency and compromise the instrumental sensitivity. More importantly, F tends to react with Si and form volatile compounds in the mass spectrometer, which induces artificial fractionation of Si isotopes. The procedures to analyze Si isotopes in this study is based on alkaline fusion and cation exchange column chemistry method (Georg et al., 2006).

## 2.2 Sample preparation

### 2.2.1 Alkaline fusion

All natural samples were in powder form when received or subsequently ground to powder using an alumina mortar and pestle. Sample digestion was carried out using the alkaline fusion technique adapted from Georg et al. (2006). Alkaline fusion method has been widely used in geochemistry to digest silicate rock samples and the theory can be

found in Potts' Handbook of Silicate Rock Analysis (Potts, 1987). Alkaline flux (NaOH) melts in a silver crucible upon heating and forms a strongly alkaline liquid that completely dissolves silicate material. The product is water soluble and Si can be separated using simple column chemistry. The advantage of the fusion method is the short processing time. It typically takes less than 48 hours from rock powders to solutions ready for isotope measurement. Additional advantage of this fusion method is that it only adds Na to the solution, which can be easily removed through cation-exchange chromatography.

Between 2.5 to 10 mg of powdered sample was weighed into a silver crucible (made in-house from 99.99 % pure sheet Ag, Alfa-Aesar) along with ca. 200 mg of NaOH flux (analytical grade, pellet form, Merck). The silver crucible was then heated at 730 °C for 10 minutes in a muffle furnace. After fusion, the crucible was taken out and allowed to cool for 40 s. The fusion product, together with the crucible, were subsequently dropped into a 50-ml Teflon beaker containing 30 ml 18.2 MΩ ultrapure water. Then capped and left to react for 24 h. Before transferring into pre-cleaned LDPE bottles, the Teflon beaker was placed in an ultrasonic bath for 15 minutes to assist the dissolution of fusion products. The crucible was rinsed several times in ultrapure water to ensure all samples were transferred. The sample was subsequently diluted with additional water and acidified with 6 M HCl to pH = 2. Final solution was stored in LDPE bottles with a Si concentration of 30 to 90 ppm.

### 2.2.2 Cation exchange chromatography

The plasma source does not discriminate with regards to what element is introduced in the mass spectrometer. As a result, most elements in the sample will be ionized and get transferred into the analyzer, including the matrix elements other than the analyte. The abundance of the matrix elements are variable depending on the chemical composition of the sample and will influence the instrument, producing biased isotope data. It is necessary, therefore, to quantitatively remove the matrix and purify the sample solution before it can be accurately analyzed.

In this study, samples were purified for Si isotope analysis using ion-chromatography based on a cation-exchange process. Each 10 ml BioRAD column was loaded with 1.8 ml BioRAD AG50W X8 (200-400 mesh) cation-exchange resin for Si separation. This exchange method is made possible by the fact that between pH 2 - 8, Si is in the form of either anionic ($H_3SiO_4^-$) or neutral ($H_4SiO_4$) species, which is not retained by the cation resin, allowing a quantitative separation from other cations by elution with ultrapure water (Georg et al., 2006). Because this method only separates Si from cations, the presence of other anions may be problematic. The potential matrix effect caused by other anion species in the sample solution is further discussed in Chapter 3. Complete separation procedure is listed in Table 2.1. The final solution is typically around 5 ml with a Si concentration of 2.8 to 5 ppm. Sample solutions were acidified to 0.15 M HCl before isotope analysis.

**Table 2.1**: Column chemistry procedure for Si separation

| Step | Volume | Concentration | Reagent |
|---|---|---|---|
| Pre-cleaning | 10ml | 2.5M | HCl |
| | 6ml | 6M | HCl |
| | 5ml | 6M | $HNO_3$ |
| | 3 ml | 6M | HCl |
| | 3 ml | 2.5M | HCl |
| Rinse | 6 ml | | $H_2O$ |
| Load | 0.3 ml (15 μg) | | Acidified sample solution |
| Elution | 5 ml | | $H_2O$ |
| Result | | 5.3 ml at 2.8 ppm Si | |

## 2.3 Mass spectrometry

### 2.3.1 General principles of MC-ICP-MS

Silicon isotopes ($^{28}Si$, $^{29}Si$, and $^{30}Si$) were analyzed simultaneously using a Nu-Plasma II (Nu Instruments, UK) multi-collector inductively coupled plasma mass spectrometer (MC-ICP-MS) at the University of Houston (Fig. 2.1). In essence, a mass spectrometer utilizes a magnet to separate ion beams according to their mass to charge ratio (m/z). The advantage of MC-ICP-MS is the application of multiple faraday cups to collect ion beams so that multiple isotopes can be analyzed simultaneously. This approach avoids the potential fluctuations in ion-beam intensity that may cause biased results. The Nu Plasma II is composed of four main components: (1) sample introduction; (2) ion source; (3) mass analyser; and (4) ion detector (Fig. 2.1)

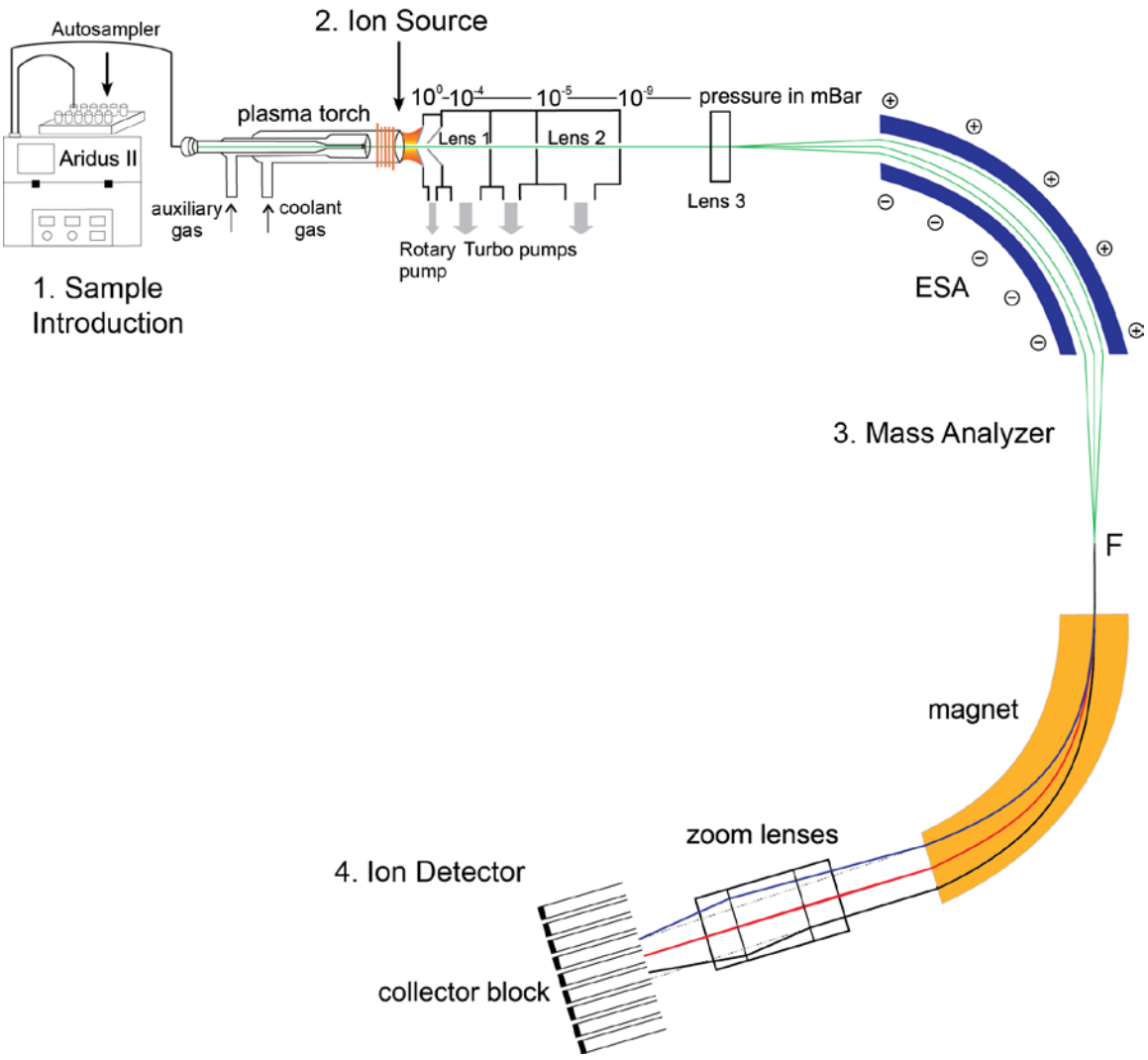


**Figure 2.1**: Schematic diagram of the Nu Plasma II, showing the sample introduction, ion source, mass analyzer and ion detector (modified from Nu Plasma II user manual).

### 2.3.2 Sample introduction

When analyzed in solution mode, it usually has a high solvent to analyte ratio due to the presence of water and HCl, which may reduce the instrument sensitivity and increase the formation of polyatomic interferences for certain analytes. It is therefore, necessary to remove the solvent before the sample was transferred into the plasma. This is achieved by using a Teledyne Cetac Technologies *Aridus II* desolvating nebulizer system with a

20 μl/min Teflon nebulizer. This ensures the samples introduced into the instrument is in aerosol form so they can be effectively ionized in the plasma. The *Aridus* removes up to 99% of the solvent, which helps prevent the formation of oxides and hydrides that interfere with the analyte. The sample solution is aspirated into a heated spray chamber through the nebulizer and form droplets of aerosols that then pass through a heated hydrophobic membrane. The vaporized solvent is removed by a counter flow sweep gas (Ar) while the sample can be further passed into the ion source through the torch.

### 2.3.3 Ion source

The mass spectrometer separates ion beams based on their mass to charge ratio, hence neutral species cannot be analyzed and need to be ionized. A number of ion sources have been utilized in the field of mass spectrometry. The Nu Plasma II MC-ICP-MS employs an inductively coupled plasma (ICP) source, which uses Ar as the plasma gas. A radio frequency (RF) induction coil powered by a 27 MHz RF generator induces a strong oscillating electromagnetic field in the ICP torch. When a high voltage spark is provided, the flux of electrons will interact with Ar gas and strips off the electrons. The free electrons and ions in the strong electromagnetic field are accelerated, increasing the kinetic energy, which in turn, ionize more particles. The plasma can reach temperature up to 6000 K, efficient enough to ionize most elements.

### 2.3.4 Mass analyzer

The key component of a mass spectrometer is its mass analyzer. In the case of the Nu Plasma II, it utilizes a double-focusing system with an electrostatic analyzer (ESA) and

an electromagnet to split a single ion beam into discrete beams and create a “mass spectrum”. The basic principle of a magnet is that any ion beam entering the magnet is subject to the magnet field and will be deflected by the Lorentz force that is orthogonal to the travel path. The curvature of the beam is controlled by the mass to charge ratio and the kinetic energy. The heavier ions will experience less force and travel in a wider curvature than the lighter ones so that the ion beams can be separated. However, one of the inherent disadvantages of an ICP source is the wide spread of kinetic energy of the ions. Therefore, a single magnet cannot separate particles based solely on their masses. The ESA, positioned before the magnet, focuses ions based on their kinetic energy, giving a trajectory that is independent of the mass. The combination of ESA and magnet allows ions with the same m/z but different kinetic energy to be focused in the same collector.

### 2.3.5 Ion detector

The ion detection assembly in Nu Plasma II includes 16 Faraday collectors and 5 ion-counting multipliers. Because of the large mass differences in Si isotopes, a wide array of the collectors are used to achieve precise isotope measurements. In this study, the Faraday cups used to detect Si ion beam intensities are L4 ($^{28}$Si), H1 ($^{29}$Si), and H8 ($^{30}$Si). When the high speed ions travel through the fly tubes and impact the Faraday collector, the charges are transferred and it creates a current detected by the electronic circuitry. The signal is amplified by the multipliers and can be measured. The Faraday collectors enables simultaneous measurement of all three isotopes of Si, which avoids any sensitivity fluctuations in the instrument causing mass bias. This allows precise determination of isotope ratios.

## 2.4 Stable Si isotope analysis using Nu Plasma II MC-ICP-MS

The polyatomic interferences derived from gaseous and dissolved molecular species include $^{14}N_2^+$ and $^{12}C^{16}O^+$ (on $^{28}Si$), $^{13}C^{16}O^+$ and $^{28}Si^1H^+$ (on $^{29}Si$), and $^{12}C^{18}O^+$, $^{14}N^{16}O^+$, $^{28}Si^2H^+$, and $^{29}Si^1H^+$ (on $^{30}Si$) can be resolved in the Nu Plasma II in medium mass resolution mode. This mode yields a resolving power of around 4000. The polyatomic ions usually have higher mass than the analyte. All three stable Si isotopes can be measured simultaneously on the flat plateau on the interference-free low mass side of the Si peaks. Peak centering was done for every analysis after 60 s of on-peak-zero baseline measurement; each analysis consists of 400 s integration in 80 5 s cycles.

Instrumental mass fractionation was corrected using a standard-sample-standard bracketing technique. The results are reported relative to the standard reference material NBS28 in the delta notation according to Coplen (2011) in per mil (‰) by multiplication of equations (2.1) and (2.2) with a factor of $10^3$:

$$\delta^{30}Si = [(^{30}Si/^{28}Si_{sample}) / (^{30}Si/^{28}Si_{NBS28})-1] \quad (2.1)$$

$$\delta^{29}Si = [(^{29}Si/^{28}Si_{sample}) / (^{29}Si/^{28}Si_{NBS28})-1] \quad (2.2)$$

# Chapter 3

# Accurate and precise silicon isotope analysis of sulfur and iron-rich samples by MC-ICP-MS

## Abstract

Silicon isotope analysis of sulfur-rich samples by MC-ICP-MS can be challenging because cation-exchange chromatography methods used for Si purification do not efficiently remove anionic sulfur species. Results of pure Si standard solutions with addition of sulfate show shifts of up to +1.04±0.10 ‰ (2SD) in $\delta^{30}$Si values. Doping of both standards and samples with S to a fixed S/Si ratio can eliminate the relative change in instrumental mass fractionation due to variable S/Si in samples and also boosts the relative sensitivity of Si by up to 66 %. Silicon isotope analysis of Fe-rich samples can be complicated by Fe hydroxide precipitation during sample processing, which adsorbs Si resulting in isotopic fractionations of the Si left in solution. Tests using Fe-rich meteorite samples show that this can be a major factor for observed shifts in $\delta^{30}$Si values. Acidification of the sample and standard solutions to a pH < 1 and subsequent pH adjustments to a range of 2 to 3 by adding ultra-pure NaOH solutions prior to cation-exchange chromatography ensures no Fe hydroxide precipitation and full recovery of Si. The combination of sulfur doping and pH treatment is proven to be reliable for Si isotope analysis for S and Fe-rich materials.

## 3.1 Introduction

High-precision silicon isotope analysis by multi-collector inductively coupled plasma mass spectrometry (MC-ICP-MS) requires quantitative extraction and purification of silicon from matrices that can cause spectral interferences and/or changes in instrumental mass fractionation (IMF). A recent study used an alkaline fusion technique at 730 °C employing pure NaOH flux to decompose samples (Georg et al., 2006). A similar method used solid NaOH monoxide to decompose sample material at ~200 °C (van den Boorn et al., 2006). Both methods utilized cation-exchange chromatography to quantitatively recover silicon and separate it from cations in the sample solution. These methods have been applied to various natural samples such as terrestrial rocks (e.g., Savage et al., 2010; Savage et al., 2012; Savage et al., 2013), lunar rocks (Armytage et al., 2012), and meteorites (Georg et al., 2007; Fitoussi et al., 2009; Chakrabarti and Jacobsen, 2010; Armytage et al., 2011; Savage and Moynier, 2013; Zambardi et al., 2013) to understand Earth and planetary processes.

The combination of alkaline-fusion digestion and ion chromatography allows fast and effective sample preparation with high silicon yield. However, samples with complex and unusual matrices, such as meteorite samples may cause unexpected results. For example, studies have shown that when Fe-rich rock samples were digested, the resultant solution is typically brownish due to the precipitation of Fe hydroxide (e.g., van den Boorn et al., 2009; Zambardi and Poitrasson, 2011), in contrast to clear solutions produced by high purity silicon samples (e.g., the $SiO_2$ standard NBS 28). It has been demonstrated that Fe hydroxide selectively adsorb light silicon isotopes (Delstanche et al., 2009), which can induce significant isotopic fractionation in the solution prior to ion chromatography.

Another issue is that the cation-exchange chromatography does not separate Si from any anion species, which may cause significant differences in IMF compared to pure Si standards. Georg et al. (2006) investigated the effect of $SO_4^{2-}$ and $NO_3^-$ by doping Si standard solutions with sulfate or nitrates and observed no significant isotopic offset when compared to non-doped solutions. However, van den Boorn et al. (2009) showed significant offset (up to +1.4 ‰) when S/Si mass ratio exceeds 0.007 ($SO_4$/Si = 0.02). Large mass-dependent isotopic shifts due to the presence of sulfur in the samples have also been noted for other elements such as thallium (Nielsen et al., 2004).

Several purification processes have been proposed to remove sulfur prior to column chemistry (van den Boorn et al., 2009; Geilert et al., 2015). Others have suggested that instead of removing sulfur, doping both samples and bracketing standards with sulfur to the same S/Si mass ratio is valid for sulfate-rich rocks and river water samples (e.g., Hughes et al., 2011). Reproducible shifts in mass bias utilizing the same S/analyte mass ratio has also been successfully done for other elements (e.g., Tl, Nielsen et al., 2004). The aims of this study are to test whether S-doping can yield accurate and precise Si isotope ratio measurements of terrestrial and extraterrestrial samples with variable S/Si ratios. Sample preparation and analytical methods are proposed that seem to eliminate potential issues with variable S/Si ratios in measured Si solutions and address the issue of Fe hydroxide precipitation that fractionates Si in sample solutions before cation-exchange ion chromatography. These methods have been successfully applied to a variety of well-characterized samples and standards.

## 3.2 Experimentation

### 3.2.1 Material and sample preparation

The effect of sulfur was investigated by doping a pure Si standard solution (PlasmaCAL, SCP Science) with a sulfate standard (in $H_2SO_4$ form, Inorganic Ventures) to achieve S/Si mass ratios that ranged from 0 to 0.45 (molar ratios 0 to 0.39), similar to that of van den Boorn et al. (2009). To test the effect of Fe hydroxide precipitations and the feasibility of the sulfur-doping technique, three commonly measured silicon isotope reference materials (RMs) and five meteorite samples with different matrices and Fe contents were used: BHVO-2 (basalt, USGS), BIR-1 (basalt, USGS), Diatomite (opal standard), Allende (CV3, carbonaceous chondrite), NWA 3134 (EL6, enstatite chondrite), NWA 1068 (shergottite), EET 87520 (eucrite), and Pena Blanca Spring (aubrite). Among all the samples measured, Allende has the most abundant sulfur up to 2 wt.% (Wasson and Kallemeyn, 1988). Both Allende and NWA 3134 contain > 20 wt.% of Fe (Wasson and Kallemeyn, 1988). These same types of meteorites have been extensively measured for Si isotopes by various laboratories (Reynolds et al., 2006; Georg et al., 2007; Fitoussi et al., 2009; Chakrabarti and Jacobsen 2010; Armytage et al., 2011; Zambardi and Poitrasson 2011; Savage and Moynier 2013; Zambardi et al., 2013), allowing accurate assessment of this new procedure. Rock samples were measured in 3 sessions (1) S-undoped & Fe-untreated, (2) S-doped & Fe-untreated, and (3) S-doped & Fe-treated.

All natural samples were in powder form when received or subsequently ground to powder using an alumina mortar and pestle. Sample digestion was carried out using the alkaline fusion technique adapted from Georg et al. (2006). Around 5 to 10 mg of sample material was mixed with one 200 mg NaOH pellet in a silver crucible (made in-house from

99.99% pure silver sheet, Alfa-Aesar) at 730 °C for 12 min. After brief cooling, the sample-bearing crucibles were immersed in 50 ml Teflon containers filled with 20 ml 18.2 MΩ water. After 24 hours, the containers were treated in an ultrasonic bath for 15 min. Crucibles were subsequently removed and rinsed with 18.2 MΩ water, which was transferred into the Teflon container. The solution was then acidified using HCl (to avoid additional $NO^+$ polyatomic interference) and diluted. Bio-Rad (Bio-Rad laboratories Inc.) 50W-X8 (200-400 mesh) cation exchange resin was used to carry out the ion chromatography following the procedures described by Georg et al. (2006).

### 3.2.2 Instrumentation

Si isotope analysis was conducted in medium resolution using a Nu Plasma II MC-ICP-MS (University of Houston) with a resolving power of about 4000. Samples were introduced into the mass spectrometer by the Aridus II desolvating system (CETAC Technologies) with a micro-concentric Teflon nebulizer in dry plasma mode. The three Si isotopes ($^{28}Si$, $^{29}Si$, and $^{30}Si$) were measured simultaneously on the flat plateau of the Si peaks on the interference-free low mass end. A 60 second on-peak-zero baseline measurement was recorded for each analysis followed by peak centering. The typical background signal in $^{28}Si$ was ~ 3 mV. Each measurement consisted of 80 cycles each with 5 s of integration time, for a total of 400 seconds of on-peak measurement. Instrumental mass bias and drift were corrected using a standard-sample-standard bracketing approach with NBS 28 as the bracketing standard, taken through the same digestion and chemical separation procedure as the samples. The results are reported with δ notation in per mil (‰) relative to NBS 28.

## 3.3 Results and discussion

### 3.3.1 Sulfur-doped standards

The results of the S-doped PlasmaCAL standards are consistent with the findings from van den Boorn et al. (2009). There is a strong and non-linear correlation between the shifts in $\delta^{30}Si$ values and the S/Si mass ratios (Fig. 3.1A). Also observed during this test is the increase in ion intensity caused by higher S/Si mass ratios (Fig. 3.1B). Significant shifts of $\delta^{30}Si$ values (expressed as $\Delta^{30}Si$) relative to undoped standards were observed (> 0.70‰) when S/Si mass ratios are higher than 0.05. Samples with S/Si ratios between 0.25 and 0.45 show the same magnitude of offset ($\Delta^{30}Si = +1.04 \pm 0.10$ ‰), indicating the maximum offset is likely reached when the S/Si mass ratio is higher than 0.25, which also corresponds to an average of 66 % increase in total Si ion beam intensity. The results show that the greatest shifts in $\Delta^{30}Si$ occur at S/Si mass ratios up to about 0.1. Thus, even trace amounts of sulfur could induce substantial shifts of $\delta^{30}Si$ values which can compromise the accuracy of the Si isotope ratio measurements (van den Boorn et al., 2009; Hughes et al., 2011). In order to eliminate the sulfur effect during Si isotope measurements, additional purification steps have been suggested to remove sulfur, which include ignition of the sample at 1350 °C (van den Boorn et al., 2009) and addition of Ba to form $BaSO_4$ precipitates (Geilert et al., 2015). However, ignition requires special equipment and the products from ignition usually form sinters that are difficult to recover. Adding Ba introduces another cation into the solution and may not completely remove all sulfates. Recent studies showed that doping Mg to the sample and standard solutions as an internal standard can correct for the instrumental mass bias (Cardinal et al., 2003; Engström et al., 2006; Zambardi and Poitrasson, 2011). But this approach requires a more complex analytical protocol. Doping the samples and

bracketing standards with excessive sulfur has been demonstrated to be a valid technique (Nielsen et al., 2004; Hughes et al., 2011). Indeed, the sulfur-doped PlasmaCAL standards show that samples with S/Si mass ratio greater than 0.25 display identical shifts in $\delta^{30}$Si values, indicating that the sulfur effect can be eliminated when samples and bracketing standards are all doped with sulfur to a fixed S/Si mass ratio that is greater than 0.25.

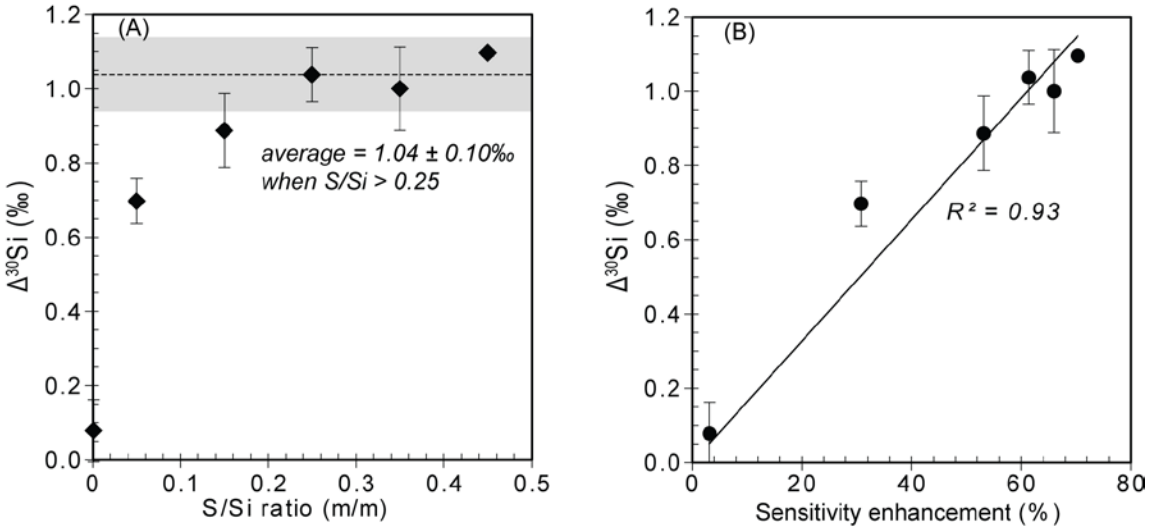


**Figure 3.1**: (A) Effect of sulfur on Si isotope measurements. $\Delta^{30}$Si represents shift in $\delta^{30}$Si values of S-doped standard relative to pure standard. Error bars are 2SE of $\Delta^{30}$Si values from three separate measurements. The average shift of $\Delta^{30}$Si values when S/Si ratios are greater than 0.25 is shown by the dashed line and the 2SD by the grey band. (B) $\Delta^{30}$Si vs. the sensitivity enhancement of Si defined as ($BI_{sample}/BI_{standard}$-1) ×100% (BI = total Si ion-beam intensity). The sensitivity enhancements for samples with S/Si > 0.25 are almost identical.

### 3.3.2 Sulfur-induced effect in rock samples

The sulfur doping method was further tested by adding pure sulfate to the solutions of rock samples after cation-exchange chromatography. Excessive amounts of sulfur was added to ensure all samples and bracketing standards have a S/Si mass ratio of 10, which

is significantly higher than natural abundances. This technique eliminates the intrinsic mass bias caused by various sulfur contents of different samples. Sulfur-rich samples that are not artificially doped with sulfur yield variable and anomalous $\delta^{30}$Si values compared to the S-doped results (Table 3.1). Chondrite samples show the largest shifts to heavier $\delta^{30}$Si values. The three achondrite samples show moderate offsets, whereas the basalt standards do not show such a shift in their $\delta^{30}$Si values (Fig. 3.2). Chondrites have the highest S/Si mass ratios, whereas terrestrial basalts have relatively low sulfur contents. The S/Si mass ratios of CV carbonaceous chondrite and EL enstatite chondrite are 0.14 and 0.18, respectively (Wasson and Kallemeyn, 1988), significantly higher than the threshold of 0.007 reported by van den Boorn et al. (2009). This implies the $\delta^{30}$Si values for carbonaceous chondrite and enstatite chondrite would be shifted to the heavy values by *ca.* +0.90 ‰ based on the estimates from the S-doped standards experiments (Fig. 3.2). The measured offsets of $\delta^{30}$Si values for Allende and NWA 3134 between S-doped and S-undoped sessions are +0.73 ‰ and +0.88 ‰, respectively, in close agreement with predicted offsets (Figure 3.2).

The basalt standard BHVO-2 shows nearly no effect due to sulfur because it has the lowest S/Si mass ratio of $5.7 \times 10^{-4}$ (Erdman et al., 2014), three orders of magnitude lower than the chondrite samples and one order of magnitude lower than the threshold reported by van den Boorn et al. (2009). The three analyzed achondrites have similar sulfur contents with an average S/Si mass ratio of 0.006 (Gibson et al., 1985; Ding et al., 2015), slightly below the threshold reported by van den Boorn et al. (2009). Even with such a low S/Si ratio, offsets of *ca.* +0.29 ‰ were observed for achondrite samples, suggesting that the sulfur effect on Si isotope measurements is greater than previously estimated. The non-linear relationship between S/Si mass ratio and $\Delta^{30}$Si (Figure 3.1A) of the sulfur-doped

PlasmaCAL standards results predicts *ca.* +0.35 ‰ shifts in $\delta^{30}$Si values for the analyzed achondrites, which is what was observed in the experimental data (Table 3.1). Thus, for accurate and precise measurement of Si isotopic composition in high S/Si content rocks, this sulfur effect must be addressed.

**Table 3.1**: $\delta^{30}$Si values for 3 sessions of measurements.

| | | S-undoped Fe-untreated | | | S-doped Fe-untreated | | | S-doped Fe-treated | | |
|---|---|---|---|---|---|---|---|---|---|---|
| Sample | Type | $\delta^{30}$Si(‰) | 2SE | n | $\delta^{30}$Si(‰) | 2SE | n | $\delta^{30}$Si(‰) | 2SE | n |
| BHVO-2 | basalt | -0.17 | 0.10 | 5 | -0.23 | 0.06 | 12 | -0.28 | 0.03 | 21 |
| BIR-1a | basalt | -0.30 | 0.15 | 7 | n.a. | | | -0.33 | 0.03 | 22 |
| Allende | CV3 | +0.64 | 0.22 | 3 | -0.09 | 0.10 | 13 | -0.42 | 0.04 | 22 |
| NWA 3134 | EL6 | +0.57 | 0.29 | 2 | -0.31 | 0.08 | 12 | -0.52 | 0.03 | 22 |
| NWA 1068 | shergottite | -0.15 | 0.19 | 2 | -0.43 | 0.09 | 12 | -0.37 | 0.03 | 9 |
| EET 87520 | eucrite | -0.12 | 0.36 | 2 | -0.41 | 0.08 | 12 | -0.46 | 0.05 | 21 |
| PBS | aubrite | -0.30 | 0.07 | 2 | -0.60 | 0.04 | 12 | -0.59 | 0.03 | 22 |
| Diatomite | opal | | | | | | | +1.25 | 0.04 | 13 |

Uncertainties are given as 2SE (standard error), calculated from SE = SD/√ n, where n is the number of single analysis and SD is the standard deviation. PBS=Pena Blanca Spring

The S-doped BHVO-2 and three achondrite samples yield $\delta^{30}$Si values that are in close agreement with previously published data, whereas the two S-doped chondrites, Allende and NWA 3134, yield $\delta^{30}$Si values that are still at least +0.20 ‰ higher than previous studies (Georg et al., 2007; Fitoussi et al., 2009; Chakrabarti and Jacobsen, 2010; Armytage et al., 2011; Zambardi and Poitrasson, 2011; Savage and Moynier, 2013; Zambardi et al., 2013). The sulfur effect is likely accountable for the total shifts in $\delta^{30}$Si values of basalt standards and achondrites. But only about 70 % shift in $\delta^{30}$Si values can be explained by

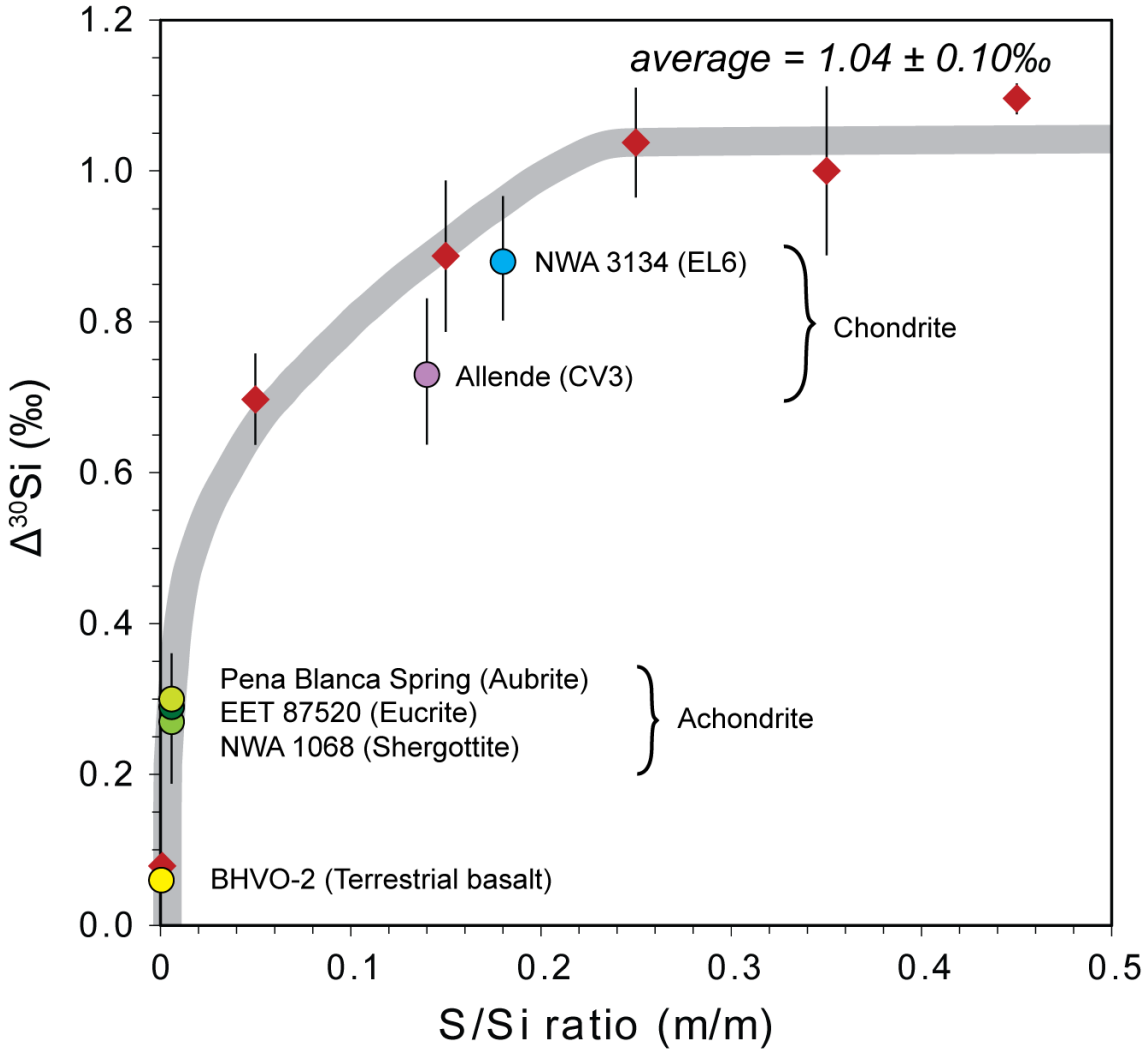


**Figure 3.2**: $\Delta^{30}Si$ (difference between S-doped and S-undoped) of rock samples vs. their S/Si mass ratios. Error bars are 2SE. Chondrites have the highest S/Si mass ratios, corresponding to the largest offsets. Achondrite show moderate offset, whereas terrestrial basalt show virtually no offset. The measured offset in $\delta^{30}Si$ values are in close agreement with the predict values from S-doped PlamaCAL experiment.

the presence of sulfur for carbonaceous chondrite and 80 % for enstatite chondrite. Other processes likely occurred during sample preparation for Allende and NWA 3134 that fractionate Si isotopes. Fitoussi et al. (2009) suggested that the solution pH plays an important role during sample preparation and the precipitation of Fe hydroxide for terrestrial samples

may cause offset in Si isotopic measurements. Delstanche et al. (2009) demonstrated that Si can adsorb onto Fe hydroxide and form surface complexes, which is accompanied by Si isotope fractionation with a fractionation factor of -1.06 ‰ for ferrihydrite and -1.59 ‰ for goethite, resulting in solutions with higher $\delta^{30}$Si values. However, the Fe effect during sample preparation on Si isotope measurement, especially for Fe-rich meteorite samples need further quantitative assessment.

### 3.3.3 The effect of Si adsorption onto Fe hydroxide precipitates during sample preparation

Alkaline fusion products have high pH because of the NaOH flux; thus these need to be acidified before cation-exchange ion-chromatography. Monosilicic acid ($H_4SiO_4$) is most stable from polymerization at pH 2 to 3 (Alexander, 1954; Iler, 1979). Therefore, in this study, samples after fusion and dissolution were acidified directly to pH 2 to 3 using 6 mol $l^{-1}$ HCl. The final solution of the two basalt standards appeared to have formed trace amounts of tannish to light-brownish Fe hydroxide precipitates. The two chondrite samples had the highest content of Fe hydroxide precipitates, which is expected because the chondrites have the highest relative Fe contents (*ca.* 22 %, Wasson and Kallemeyn, 1988). Previous studies have shown similar Fe hydroxide precipitation after sample acidification (Fitoussi et al., 2009; Zambardi and Poitrasson, 2011). The results of this study show that directly bringing down the solution pH to 2 to 3 cannot eliminate the precipitation of Fe hydroxide. Additional heating steps were also tested but failed to produce clear solutions. The offsets in Si isotope ratios for Fe-rich Allende and NWA 3134 with sulfur-doping compared to values in the literature is likely the result of Si adsorption onto Fe precipitates.

High pH of sample solutions (4 – 10) without enough acidification may not only cause more Fe precipitates, but also substantially increase the Si adsorption onto Fe hydroxide (Jones and Handreck, 1963). A new step is therefore proposed to eliminate the precipitation of Fe hydroxide prior to ion-exchange chromatography. This is done by acidifying the solution with HCl to a pH < 1. This step dissolves all of the Fe hydroxide resulting in clear solutions. Before loading solutions on ion-exchange columns, the pH was adjusted to a range of 2 to 3 by slowly adding a 1 mol $l^{-1}$ NaOH solution. This step did not result in any Fe hydroxide precipitates. Overall, Fe-treated and S-doped samples produced the best match with previously published data with less scattered $\delta^{30}$Si values.

### 3.3.4 Accuracy and precision

Silicon isotope results of RM from the Fe-treated and sulfur-doped experiments are listed in Table 3.2. BHVO-2 yielded $\delta^{30}$Si = -0.28±0.13 ‰ (2SD, n = 21, where n is the number of single analysis) and $\delta^{29}$Si = -0.14±0.06 ‰ (2SD). This result is consistent with published values for BHVO-2 (Abraham et al., 2008; Fitoussi et al., 2009; van den Boorn et al., 2009; Zambardi and Poitrasson, 2010). International Si isotope RM Diatomite, a sample of purified diatomite prepared and distributed by Mark Brzezinski of UCSB (Reynolds et al., 2007), was also measured through Fe-treatment and S-doping with a $\delta^{30}$Si composition of +1.25±0.14 ‰ (2SD, n = 13), in agreement with the well calibrated value for Diatomite (+1.26±0.10 ‰, 1SD, Reynolds et al., 2007). The reproducibility of BHVO-2 standard was ±0.13 ‰ (2SD) for $\delta^{30}$Si values and ±0.06 ‰ (2SD) for $\delta^{29}$Si values (Fig 3.3). The meteorite samples after Fe-treatment and S-doping yield results that are within uncertainty of previously published data (Georg et al., 2007; Fitoussi et al., 2009; Ziegler

et al., 2010; Armytage et al., 2011; Savage and Moynier, 2013) (Fig. 3.4). These results suggest that the combination of sulfur doping and Fe treatment is valid for Si isotope analyses for sulfur and iron-rich samples.

**Table 3.2**: Results of Fe-treated and S-doped analyses for BHVO-2 and Diatomite and inter-laboratory comparison.

| Sample | $\delta^{30}$Si(‰) | 2SD | $\delta^{29}$Si(‰) | 2SD | n[a] |
|---|---|---|---|---|---|
| **BHVO-2** | | | | | |
| This study | -0.28 | 0.14 | -0.14 | 0.06 | 21 |
| Abraham et al., (2008) | -0.31 | 0.26 | -0.17 | 0.13 | 19 |
| Zambardi and Poitrasson (2008) | -0.27 | 0.08 | -0.14 | 0.05 | 42 |
| Fitoussi et al., (2009) | -0.32 | 0.04* | -0.16 | 0.04* | 14 |
| Armytage et al., (2011) | -0.28 | 0.14 | -0.15 | 0.08 | 223 |
| Savege et al., (2011) | -0.29 | 0.09 | -0.15 | 0.08 | 188 |
| Savege and Moynier (2013) | -0.28 | 0.09 | -0.15 | 0.06 | 44 |
| **BIR-1** | | | | | |
| This study | -0.33 | 0.13 | -0.16 | 0.06 | 22 |
| Zambardi and Poitrasson (2008) | -0.27 | 0.07 | -0.12 | 0.04 | 6 |
| **Diatomite** | | | | | |
| This study | 1.25 | 0.14 | 0.66 | 0.12 | 13 |
| Reynolds et al., (2007) | 1.26 | 0.20 | 0.64 | 0.14 | 100 |
| Fitoussi et al., (2009) | 1.24 | 0.02* | 0.64 | 0.01* | 89 |
| Chakrabarti and Jacobsen (2010) | 1.23 | 0.03* | 0.61 | 0.02* | 41 |
| Ziegler et al., (2010) | 1.22 | 0.18* | 0.63 | 0.02* | 1 |
| Armytage et al., (2011) | 1.23 | 0.15 | 0.63 | 0.10 | 400 |
| Savege et al., (2011) | 1.23 | 0.10 | 0.64 | 0.08 | 177 |
| Savege and Moynier (2013) | 1.22 | 0.10 | 0.63 | 0.06 | 43 |

[a] number of single analysis

* Uncertainties are given as 2SE.

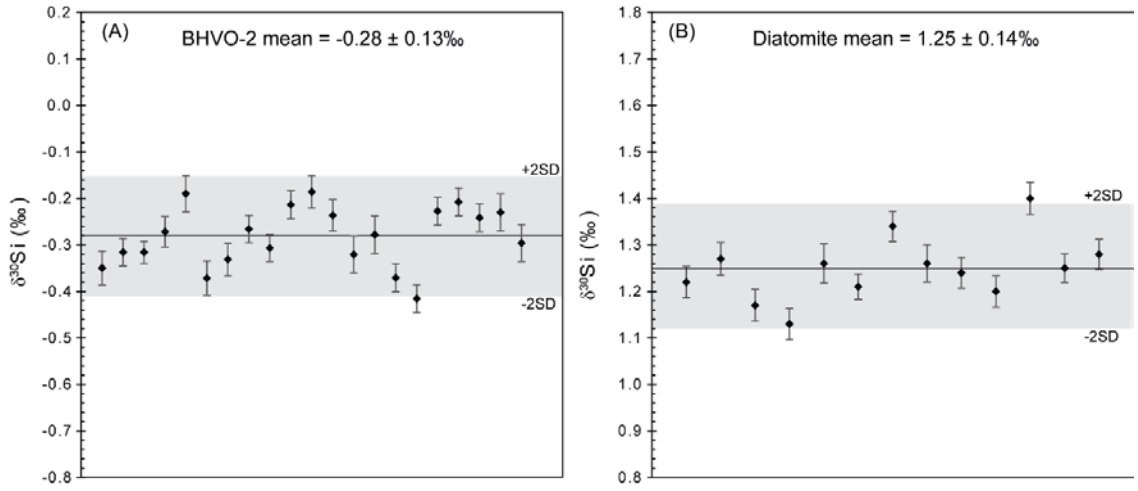


**Figure 3.3**: The Fe-treated and S-doped experiments give precise and accurate results of RMs. (A) Reproducibility of terrestrial basalt RM BHVO-2 is ±0.13 ‰ (2SD) for $\delta^{30}$Si values. (B) International Si isotope RM Diatomite gives a reproducibility of ±0.14 ‰ (2SD) for $\delta^{30}$Si values. The shaded field indicates the 2SD of the analyses.

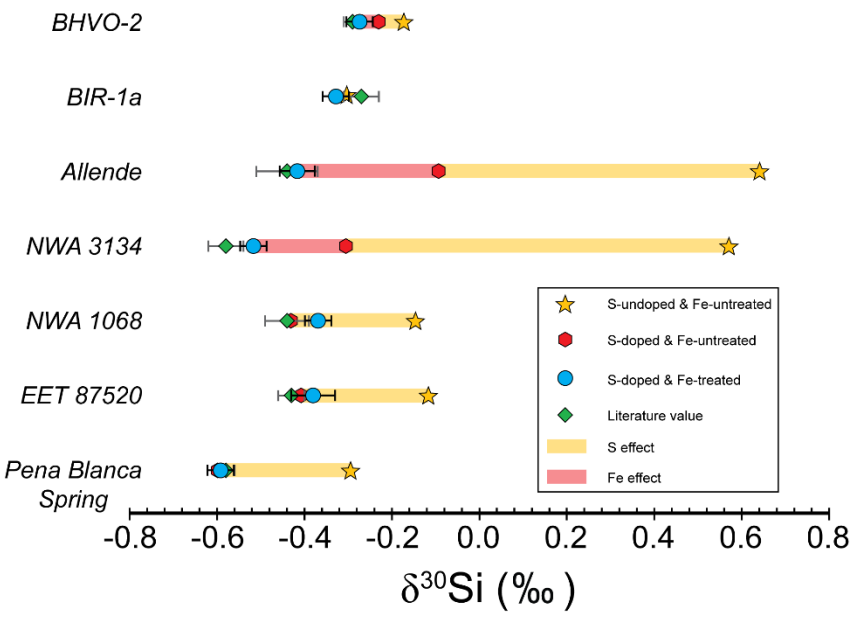


**Figure 3.4**: Results of $\delta^{30}$Si values for terrestrial rock RMs and meteorite samples in 3 sessions (1) S-undoped & Fe-untreated, (2) S-doped & Fe-untreated, and (3) S-doped & Fe-treated compared with the literature values (Reynolds et al., 2007; Abraham et al., 2008; Fitoussi et al., 2009; Armytage et al., 2011; Armytage et al., 2012; Ziegler et al., 2012; Savage and Moynier, 2013; Zambardi et al., 2013). Bars represent the shift in $\delta^{30}$Si values induced by the presence of sulfur and iron during the sample preparation processes. Error bars are 2SE.

## 3.4 Conclusions

This study confirms that sulfur can cause significantly biased Si-isotopic measurements. Results of pure Si standard solutions with addition of sulfate show shifts of up to +1.04±0.10‰ (2SD) in $\delta^{30}$Si values. Meteorite samples yield anomalous $\delta^{30}$Si values, which may be partially explained by the presence of sulfur. The experiments show that the precipitation of Fe hydroxide during sample preparation may be another process that causes shift in $\delta^{30}$Si values. A relative simple approach is proposed to eliminate the effects of sulfur and Fe hydroxide by a combination of sulfur-doping and careful pH adjustments. This technique ensures quantitative recovery of Si and also has the benefit of increasing Si-ion intensity during MC-ICP-MS analysis. The modified method was proven to be suitable for S and Fe-rich samples.

# Chapter 4

# Silicon isotope compositions of euhedral authigenic quartz crystals: implications for abiotic fractionation at surface temperatures[1]

## Abstract

Silicon (Si) isotopes have been demonstrated as proxies for the paleoenvironmental conditions of various silica deposits. In an effort to investigate the petrogenesis and paleoenvironments of Phanerozoic silica deposits, a suite of euhedral megaquartz crystals in the Cretaceous Edwards Formation from central Texas was petrographically analyzed and their Si isotopic compositions analyzed by bulk and *in situ* techniques. Petrographic analysis shows a close relationship between megaquartz and evaporite minerals. The lithologic association of silica with evaporite-bearing dolomitized carbonate strata suggests that the silicification probably developed in a back-reef tidal-flat environment in which quartz crystals formed after the primary calcite cementation and partial dissolution of evaporites. Silicon isotopic mapping across the megaquartz crystals show that $\delta^{30}Si_{(NBS28)}$ values range from -2.90 to +2.94‰. These values span the majority of published silicon isotopic values observed in nature and indicate complex growth histories. The negative $\delta^{30}Si$ values are attributed to the dissolution of sponge spicules, which likely act as the primary source of the authigenic megaquartz.

[1] A version of this chapter has been published as "Silicon isotope compositions of euhedral authigenic quartz crystals: Implications for abiotic fractionation at surface temperatures" Chen, X., Chafetz, H. S., Andreasen, R., and Lapen, T. J., 2016. Chemical Geology, v. 423, p. 61-73.

The observed range of $\delta^{30}Si$ values in megaquartz crystals is interpreted using a two stage model in which amorphous silica from sponge spicules is dissolved and re-precipitated as megaquartz in a closed system during diagenesis. This Rayleigh-type fractionation model also adds a new level of insight into the abiotic fractionation factor between dissolved and precipitated silica. Based on temperature estimates of 20 to 50 °C for megaquartz precipitation, the fractionation factor was determined to be between -1.8 to -2.1 ‰. The estimated average $\delta^{30}Si$ value of Early Cretaceous seawater is +2.7 to +3.0 ‰, significantly higher than modern seawater.

## 4.1 Introduction

Silicification in carbonates has occurred throughout the geological record from the Precambrain to Quaternary (Knauth and Epstein, 1976; Bustillo, 2010). Silica is a common diagenetic constituent in shallow marine carbonate that occurs in a variety of crystal forms and morphologies (Pittman, 1959; Folk and Pittman, 1971; Chowns and Elkins, 1974; Knauth, 1979; Milliken, 1979; Geeslin and Chafetz, 1982; Chafetz and Zhang, 1998; Scholle and Ulmer-Scholle, 2003). Knauth (1992) classified authigenic silica into 3 types of amorphous opal (opal-A, opal-CT, and opal-C) and 5 types of quartz (granular microcrystalline quartz, megaquartz, length-fast chalcedony, length-slow chalcedony, and zebraic chalcedony). Some of these silica samples have been considered as proxies for paleoenvironmental conditions. For example, a number of studies have investigated oxygen isotopic compositions ($\delta^{18}O$) in chert to infer climatic temperatures through time (Dengens and Epstein, 1962; Knauth and Epstein, 1976; Knauth and Lowe, 2003), whereas others

have attributed zebraic chalcedony to the presence of sulfur in the water and the association of evaporites (Milliken, 1979; Geeslin and Chafetz, 1982). However, the mechanism of silicification is not well constrained. Authigenic silica can be formed by: (1) recrystallization of an amorphous silica precursor upon diagenesis (Hesse, 1989; Knauth, 1994); (2) direct precipitation from aqueous solutions (Mackenzie and Gees, 1971; Guidry and Chafetz, 2002; Marin et al., 2010); and (3) replacement of preexisting carbonate rocks (Hesse, 1989; Knauth, 1994). Several possible explanations have been suggested for the replacement of carbonate. These include silica precipitation induced by local decrease in pH that is caused by either biological production of $CO_2$ (Siever, 1962), oxidation of sulfide into sulfate (Clayton, 1986; Chafetz and Zhang, 1998), or by mixing of marine and meteoric waters (Knauth, 1979).

In addition to the uncertainty in the factors controlling precipitation, the sources of silica and their relative contributions are still not well understood. The silica may originate from silica secreting organisms (e.g., diatom frustules, sponge spicules, and radiolarians) or through abiotic processes. Abiotic silica sources in carbonate rocks include volcanic ash, by-products of chemical weathering during clay formations and hydrothermal fluids (Scholle and Ulmer-Scholle, 2003). Furthermore, the timing of silicification is not well-constrained because examples of early, intermediate, and late silicification have all been described in the literature (e.g., Hesse, 1989). Bustillo (2010) suggested that the silicification in carbonates during early, shallow burial may occur under quite different conditions than those from later burial stages. Understanding the timing and environmental conditions of silicification along with the sources of silica are crucial in understanding the nature of their diagenesis.

Recent studies (Robert and Chaussidon, 2006; van den Boorn et al., 2010; Chakrabarti et al., 2012; Marin-Carbonne et al., 2012) have used Si isotopes to trace the origin of Archean and Proterozoic chert and the environment of the Precambrian Ocean. Chakrabarti et al. (2012) reported a range of $\delta^{30}$Si in Precambrian chert samples between -4.29 and +2.85 ‰ and suggested a Rayleigh-type kinetic fractionation model to explain the observed range of $\delta^{30}$Si values. Additionally, it has been demonstrated that $\delta^{30}$Si can be used to delineate chert that has precipitated directly from seawater compared to hydrothermal chert (van den Boorn et al., 2007, 2010). Studies of Phanerozoic samples are used to constrain global biogeochemical cycles. Silicon isotope compositions have been measured in a wide range of natural samples that include abiogenic and biogenic (diatom and sponge) silica from marine and fresh waters (De La Rocha et al., 1997, 2000; De La Rocha, 2003; Ding et al., 2005; Fripiat et al., 2007; Georg et al., 2009; Hendry et al., 2010; Ding et al., 2011), soils and silcrete (Basile-Doelsch et al., 2005; Opfergelt et al., 2009; Steinhoefel et al., 2011), as well as silica secreting plants (Ding et al., 2005; Opfergelt et al., 2006). Despite the renewed interest in the application of stable Si isotopes in geologic and biogeochemical problems, there is still a gap between the Precambrian and modern silica samples. Stable Si isotopes of Phanerozoic silica have not been characterized in the literature. Although diatoms, among silica secreting organisms, almost completely control the modern silicon cycle, the dissolved silicic acid concentration and its isotopic composition in the Mesozoic marine waters may be quite different because diatoms did not evolve until the Oligocene (Wells, 1983; De La Rocha, 2007). De La Rocha and Bickle (2005) suggested that average values of $\delta^{30}$Si in marine silicic acid in the “pre-diatom” ocean waters may have been considerably higher than those of the modern ocean.

Experimental studies have been carried out to understand the mechanism and factors that control Si isotopes fractionation during precipitation and dissolution (Demarest et al., 2009; Geilert et al., 2014; Oelze et al., 2014; Wetzel et al., 2014). However, the Si isotope fractionation factor between precipitates and dissolved silica in fluids ($\Delta^{30}Si_{prec\text{-}diss}$) is still not well constrained. There is a large discrepancy between laboratory experiments and studies of natural samples. Temperature, reaction rate, saturation state, reactive surface area, and flow regime (Li et al., 1995; Delstanche et al., 2009; Geilert et al., 2014) have all been shown to affect the fractionation. For instance, Li et al. (1995) conducted batch experiments on silica precipitation and observed that only under low temperature and very fast precipitation rate will the fractionation factor reach its maximum. Recently, Geilert et al. (2014) used flow-through experiments to produce silica precipitation in the 10 to 60 °C temperature range and observed a negative relationship between the fractionation factor and temperature. A similar temperature dependent trend has also been reported by Roerdink et al. (2015). Basile-Doelsch et al. (2005) used an average $\Delta^{30}Si_{prec\text{-}diss}$ value of -1.5 ‰ in their pedogenic and groundwater silcrete studies. Other values of $\Delta^{30}Si_{prec\text{-}diss}$ = -2.3 ‰ (van den Boorn et al., 2010), -2.0 and -3.0 ‰ (both in Chakrabarti et al., 2012) have also been used in the literature. It appears that solid-fluid Si isotope fractionation in natural surface condition is poorly constrained and system dependent.

In this study, laser ablation (LA) *in situ* and solution-based bulk Si isotope analyses were applied to doubly terminated authigenic euhedral megaquartz crystals collected from the Cretaceous Edwards Formation at Lake Georgetown Spillway, central Texas. The high spatial-resolution Si isotope data in concert with petrographic and petrologic observations constrain models of the paleoenvironmental conditions during the euhedral authigenic

quartz crystals formation. Further, a two-stage Rayleigh-type kinetic model is used to constrain abiotic Si isotope fractionation factors during quartz formation. Finally, the hypothesis that the "pre-diatom" ocean waters may have higher $\delta^{30}$Si value than the modern seawater was tested.

## 4.2 Geologic background

The Upper Albian Edwards Formation in central Texas is characterized by rudist reefs and associated inter-reef deposits which were formed on an extensive warm shallow marine carbonate platform known as the Comanche Platform (Fisher and Rodda, 1969; Mukherjee et al., 2010). The platform was bounded by the deep water Ancestral Gulf of Mexico on the southeast and the shallow marine North Texas - Tyler Basin on the north and west (Fisher and Rodda, 1969; Mukherjee et al., 2010). In central Texas, the Edwards is the youngest formation of the Lower Cretaceous Fredericksburg Group, conformably underlain by the Glen Rose Formation and disconformably overlain by the Georgetown Formation (Rose, 1972). The surface exposure of the Edwards Formation in central Texas generally parallels the Balcones Fault Zone. On the down-thrown side of the fault zone, the Edwards Formation is found in the subsurface in south-central Texas. Fisher and Rodda (1969) recognized four depositional facies of the Edwards Formation that include: (1) rudist bioherm facies, (2) platform grainstone facies, (3) lagoonal facies, and (4) diagenetic dolomitic facies. Lithologically, the Edwards Formation is composed of both primary and diagenetic limestone, dolomite, chert, and evaporites (Nelson, 1973). The study area is located in the spillway of Lake Georgetown (Fig. 4.1) near the city of Georgetown,

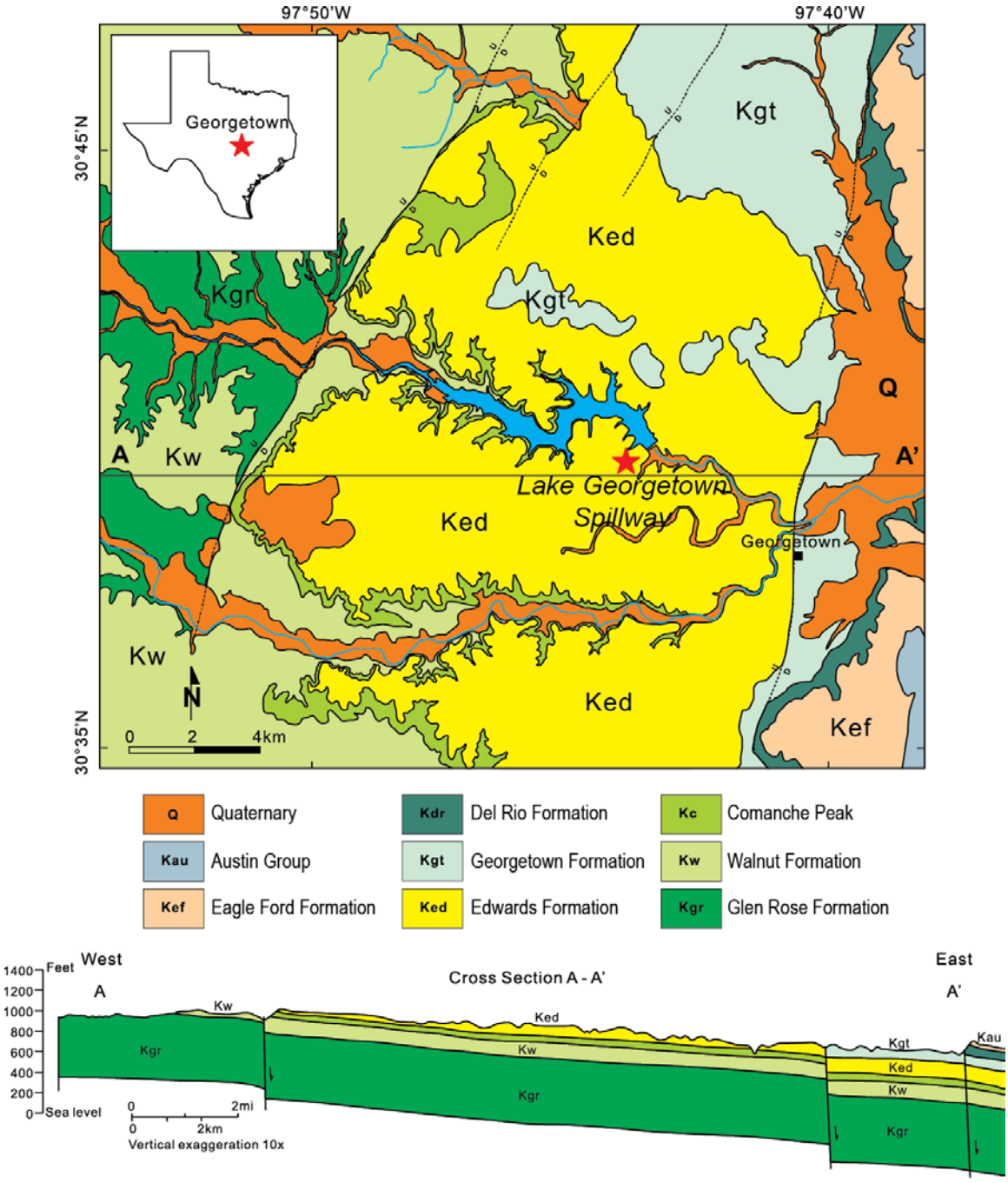


**Figure 4.1**: Geologic map of the spillway of Lake Georgetown and vicinity in central Texas, USA (modified from Collins, 2005). Also shown is a cross-section A-A' from west to east. Dashed line shows location of the Balcones fault zone that crosses the city of Georgetown in N-S direction.

Williamson County, in central Texas. The spillway exposes the upper part of the Edwards Formation. The section on the eastern side of the spillway is characterized by a shallowing-upward carbonate sequence that includes subtidal fossiliferous wackestone and thoroughly bioturbated mudstone, intertidal cross-stratified peloidal packstone and grainstone, and supratidal laminated grainstone with displacive evaporite nodules. Euhedral megaquartz crystals are found exclusively in a 15 cm thick horizon within the dolomitic grainstones (Fig. 4.2). The quartz appears as single euhedral crystals and crystal clusters. Most single crystals are prismatic, either with well-developed double terminations or well-defined crystal faces. Individual crystals range from 1 mm to 1 cm in length. After washing with hydrochloric acid (HCl) to remove carbonate, most quartz crystals appear to be clear with cloudy patches containing fluid and solid inclusions. Crystal clusters are composed of groups of quartz crystals that all developed from a common point of origin. When the quartz grains are viewed in thin sections, the textures and grain morphologies of the quartz found in the Cretaceous Edwards Formation strongly resemble the euhedral megaquartz crystals in Pleistocene sabkha dolomite from the Persian Gulf described by Chafetz and Zhang (1998) and the Herkimer Diamonds (HD, hereafter) in Cambrian Little Falls Dolomite in Herkimer County, New York (Zenger, 1976).

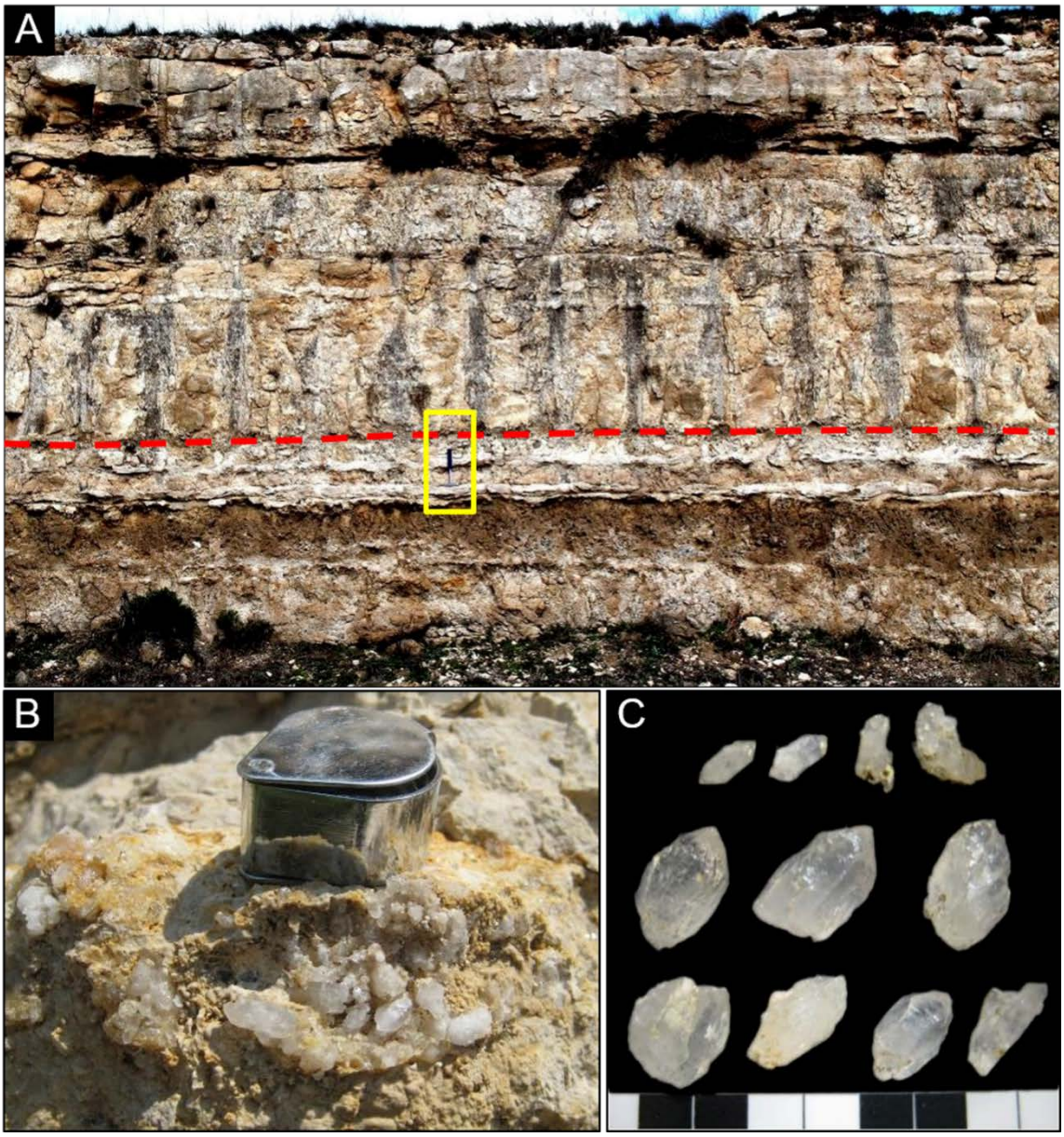


**Figure 4.2**: (A) Outcrop at the eastern side of the spillway of Lake Georgetown. Red dashed line indicates the horizon rich in euhedral megaquartz crystals and crystal clusters. Yellow box highlights the rock hammer for scale (28 cm). Total thickness of the section is about 3 m. (B) Euhedral megaquartz crystals can be readily recognized on the outcrop, hand lens for scale. (C) Single quartz crystals collected from the outcrop. Individual crystals range from 1 mm to 1 cm in size (full length of scale bar is 4.5 cm, small boxes are 0.5 cm long).

## 4.3 Analytical methods

### 4.3.1 Petrography

Thin sections of dolomitized limestone samples containing megaquartz crystals were studied by both optical and electron-beam techniques. For the electron-beam work, thin sections were carbon coated and imaged with a JEOL JSM 6400 scanning electron microscope (SEM) in backscattered electron (BSE) mode with an accelerating voltage of 15 kV and a working distance of 15 mm. Energy dispersive spectroscopy (EDS) was employed to determine the mineralogy of the inclusions in quartz crystals.

### 4.3.2 X-ray diffraction

Carbonate samples that host the quartz were crushed using an agate mortar and pestle. X-ray diffraction (XRD) analyses of host carbonate were performed with a Siemens D-5000 Diffractometer to determine the relative degree of dolomitization. A Cu Kα X-ray source with a wavelength of 1.54 Å was used with power settings of 40 kV and 30 mA. Diffraction data were collected for a wide range of 2θ angles from 20 to 70°. The peak intensity ratios of the principle dolomite (2.88 Å) and calcite (3.03 Å) reflections were measured. The results were then fit to the calibration curves of Royse et al. (1971) to determine the relative degree of dolomitization.

### 4.3.3 Mass spectrometry

Silicon isotopes ($^{28}Si$, $^{29}Si$, and $^{30}Si$) were analyzed simultaneously using a Nu-Plasma II multi-collector inductively coupled plasma mass spectrometer (MC-ICP-MS) at

the University of Houston. The polyatomic interferences derived from gaseous and dissolved molecular species $^{14}N_2^+$ and $^{12}C^{16}O^+$ (on $^{28}Si$), $^{13}C^{16}O^+$ and $^{28}Si^1H^+$ (on $^{29}Si$), and $^{12}C^{18}O^+$, $^{14}N^{16}O^+$, $^{28}Si^2H^+$, and $^{29}Si^1H^+$ (on $^{30}Si$) can be resolved in the NuPlasma II in medium mass resolution mode. This mode yields a resolving power of around 4000. All three stable Si isotopes were measured simultaneously on the flat plateau of the Si peak on the interference-free low mass side of the Si peaks. Instrumental mass fractionation was corrected using a standard-sample-standard bracketing technique (Georg et al. 2006). The results are reported relative to the standard reference material NBS28 in the delta notation according to Coplen (2011) in per mil (‰) by multiplication of equations (4.1) and (4.2) with a factor of $10^3$:

$$\delta^{30}Si = [(^{30}Si/^{28}Si_{sample})/(^{30}Si/^{28}Si_{standard})-1] \quad (4.1)$$

$$\delta^{29}Si = [(^{29}Si/^{28}Si_{sample})/(^{29}Si/^{28}Si_{standard})-1] \quad (4.2)$$

4.3.3.1 *In situ* Si isotope analysis

Centimeter-size megaquartz crystals collected from the field site were washed in HCl to remove carbonate prior to isotopic analysis. Four quartz crystals and two HD samples were cut in half parallel to their crystallographic c-axis using a low-speed water-cooled diamond blade saw to expose the longitudinal sections. Samples were cleaned with 18.2 MΩ water in an ultrasonic bath and air dried. For each quartz crystal, half of the sample was mounted in epoxy with standards while the other half was ground with an alumina pestle and mortar for bulk analysis. The sample mounts were then polished until a flat surface was obtained. Spot analyses were carried out using laser ablation (LA) MC-ICP-

MS with a PhotonMachines *Analyte.193* laser ablation system. Laser operating conditions are listed in Table 4.1.

**Table 4.1**: Operating parameters of LA-MC-ICP-MS system

| | A193-Nu Plasma II system |
|---|---|
| *Laser ablation parameters* | |
| Spot diameter | 83.8 μm |
| Repetition rate | 3 Hz |
| Total shots | 120 |
| Energy setting | 4.41 J/cm$^2$ |
| He ablation gas flow rate | 500 ml/min |
| | |
| *MC-ICP-MS parameters* | |
| Mix gas flow | 0.97-1.08 l/min |
| Aux gas flow | 0.85-1.02 l/min |
| RF power | 1300 W |
| Cool gas flow | 13 l/min |

For each measurement, on-peak-zero baseline was measured for 60 s followed by 40 s of data collection with integration cycles of 0.2 s. Previous studies by LA-MC-ICP-MS using nasosecond laser ablation systems have shown precision in natural and synthetic samples of ±0.40 ‰ (2SD) for $\delta^{30}$Si by Shahar and Young (2007) and Janey et al., 2011). Four quartz crystals and two HD samples were analyzed in three laser ablation sessions (Table 4.2). During the first two sessions, Caltech Rose Quartz (CRQ) was used as a bracketing standard instead of the widely used NBS28 (NIST RM8546) because of the insufficient average size of the fine-grained NBS28 standard for spot analysis. CRQ was used by Douthitt (1982) and De La Rocha et al. (1996) in their $\delta^{30}$Si measurements as the reference

standard. De La Rocha et al. (1997) measured both CRQ and NBS28 samples and concluded the $\delta^{30}Si$ values are identical within error. An in-house standard, Monadnock Bull Quartz (MBQ, Devonian pegmatitic white to milky quartz from Mount Monadnock, New Hampshire), was also analyzed alongside samples during analytical sessions to assess the accuracy and precision of the measurements. Fragments are available upon request. In session 3, the standard CRQ fragmented remarkably by laser ablation possibly due to the abundance of inclusions (Fig. 4.3), which failed to generate a stable signal for precise isotope ratio measurements. The in-house standard MBQ however, yielded more stable signal intensities in session 3 and was thus utilized as the reference material for sample standard bracketing. CRQ was measured alongside to check the accuracy.

**Table 4.2**: Samples and standards analyzed in this study

| Session# | Sample analyzed | Standard (‰) | | | | | In-house standard (‰) | | | | |
|---|---|---|---|---|---|---|---|---|---|---|---|
| | | | $\delta^{30}Si$ | 2SD | $\delta^{29}Si$ | 2SD | | $\delta^{30}Si$ | 2SD | $\delta^{29}Si$ | 2SD |
| 1 | Qtz_1 | CRQ | 0.00 | 0.67 | 0.00 | 0.29 | MBQ | -0.36 | 0.59 | -0.26 | 0.36 |
| 2 | Qtz_4 HD | CRQ | 0.00 | 0.39 | 0.00 | 0.39 | MBQ | -0.08 | 0.45 | -0.06 | 0.40 |
| 3 | Qtz_6 Qtz_7 HD | MBQ | 0.00 | 0.43 | 0.00 | 0.28 | CRQ | 0.22 | 0.41 | 0.03 | 0.16 |

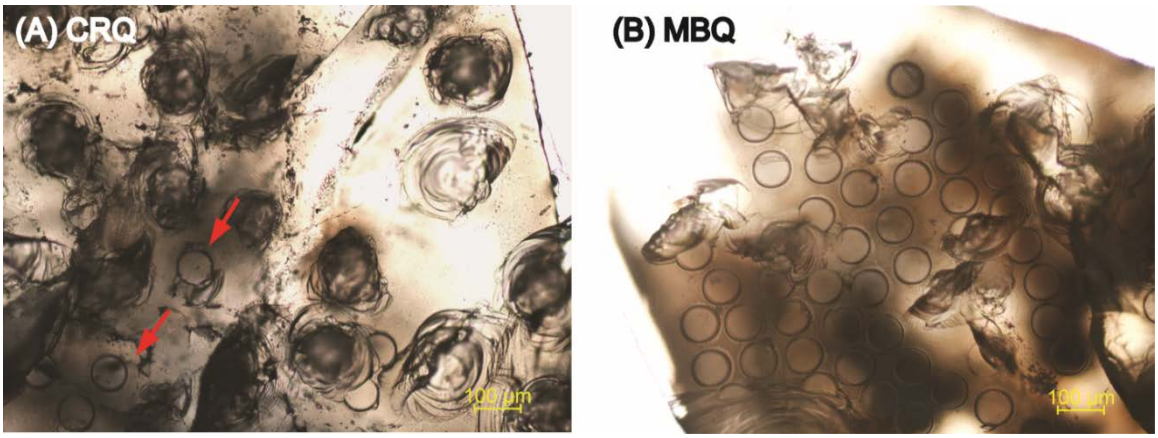


**Figure 4.3**: (A) Caltech Rose Quartz (CRQ) fragmented during *in situ* analysis session 3. Concoidal fractures generated by laser ablation were greater than normal laser pits (red arrows). Si isotope signals were inconsistent. In contrast, (B) Monadnock Bull Quartz (MBQ), generated stable and consistent laser pits for Si isotopic analysis.

The obtained average fractionation between CRQ and MBQ ($\Delta^{30}Si_{CRQ\text{-}MBQ}$) from 67 measurements was -0.24±0.60 ‰ for $^{30}Si$ and -0.17±0.43 ‰ for $^{29}Si$. Therefore, results from Run #3 was converted using the following equation:

$$\delta^{30}Si_{CRQ} = \delta^{30}Si_{MBQ} + \Delta^{30}Si_{CRQ\text{-}MBQ} \quad (4.3)$$

where $\delta^{30}Si_{CRQ}$ is the measured sample $\delta^{30}Si$ value relative to CRQ and $\delta^{30}Si_{MBQ}$ represents the measured sample $\delta^{30}Si$ value relative to MBQ. A long-term $\delta^{30}Si$ reproducibility of ±0.56 ‰ (2SD, n = 137) was obtained on CRQ standard and of ±0.43 ‰ (2SD, n = 83) on MBQ in three analysis sessions separated by 18 months (Supplement Fig S1). As both the samples and the standards are high purity quartz crystals, the matrix effect can be negligible. Inclusions in quartz samples were avoided during spot analyses.

In comparison to the gas-source mass spectrometry (GS-MS), which analyzes bulk composition of Si isotopes on various samples (e.g., total rock, seawater, river water, soil),

LA-MC-ICP-MS, though less precise than bulk measurements, can facilitate measurements in high spatial resolution. In addition, with *in situ* analysis the use of highly hazardous $F_2$ or $BrF_5$ gases are avoided. Furthermore, *in situ* Si isotope analysis using secondary-ion mass spectrometry (SIMS) on groundwater silcrete (Basile-Doelsch et al., 2005) and Archean and Paleoproterozoic BIFs (Heck et al., 2011) show similar analytical precision (2SD) of $\delta^{30}$Si with ±0.75 ‰ and ±0.30 ‰, respectively. Therefore, in spite of a lower precision, the *in situ* analysis of Si isotopes by LA-MC-ICP-MS provides fast and reliable measurements with great spatial resolution on individual quartz grains.

4.3.3.2 Bulk Si isotope analysis

Bulk Si isotope composition of quartz crystals were measured following the methods detailed by Georg et al. (2006). Between 2.5 to 10 mg of powdered sample was weighed into a silver crucible (made in-house from 99.99 % pure sheet Ag, Alfa-Aesar) along with ca. 200 mg of NaOH flux (analytical grade, pellet form, Merck). Alkaline fusion was carried out in the silver crucibles at 730 °C for 10 minutes in a muffle furnace. After fusion, crucibles were taken out and allowed to cool for 40 s. The fusion cakes, together with the crucibles, were subsequently dropped into 50-ml Teflon beakers containing 30 ml 18.2 MΩ water, capped and left to react for 24 h. The Teflon beakers were placed in an ultrasonic bath to assist the dissolution of fusion cakes before samples were transferred into pre-cleaned LDPE bottles. Crucibles were rinsed several times in 18.2 MΩ water to ensure all samples were transferred. Finally, the samples were diluted with additional water and acidified with 6 M $HNO_3$ to pH = 3.

Samples were purified for Si isotope analysis using ion-chromatography based on a cation-exchange process. Each 10 ml BioRAD column was loaded with 1.8 ml BioRAD AG50W X8 (200-400 mesh) cation-exchange resin for Si separation. This exchange method is made possible by the fact that between pH 2 - 8, Si is in the form of either anionic ($H_3SiO_4^-$) or neutral ($H_4SiO_4$) species, which is not retained by the cation resin, allowing a quantitative separation from other cations by elution with 18.2 MΩ water (Georg et al., 2006). The final solution was typically 5.3 ml with a Si concentration of 5 µg/g. Sample solutions were acidified to 0.2 % $HNO_3$ before analysis. Samples were introduced into the mass spectrometer by a Teledyne Cetac Technologies *Aridus II* desolvating nebulizer system with a 20 µl/min teflon nebulizer. Peak centering was done for every analysis after 60 s of on-peak-zero baseline measurement; each analysis consists of 400 s integration in 80 5 s cycles. NBS28 was used for standard-sample-standard bracketing in bulk analyses. Before each analysis, the solutions were checked to ensure that samples and standard have the same concentration by measuring the intensity of $^{28}Si$ beam.

## 4.4 Results

### 4.4.1 Microscopy

Thin sections of the quasi-hexagonal megaquartz crystals viewed under a petrographic microscope, appeared to have undulose extinction with sectors in different crystallographic orientations. Crystal clusters are composed of radiating prismatic euhedral quartz. These clusters have zoned cavities in the center that show fibrous microquartz cavity fillings. Petrographic observations reveal that many megaquartz crystals contain lath-shaped

crystal inclusions that are clear under plane-polarized light (Fig. 4.4A) and show second order birefringence under cross-polarized light (Fig. 4.4B, 4.4C, 4.4D). Proportions of inclusions vary considerably between quartz crystals. The inclusions are elongate with distinctive cleavage perpendicular to the growth axis as revealed by SEM and backscattered electron images (Fig. 4.5A, 4.5B, 4.5C). EDS analyses of the inclusions show high intensity peaks of calcium, sulfur, and oxygen. Semi-quantitative elemental results of the inclusions reveal a 1:1 atomic ratio of Ca:S and a 4:1 atomic radio of O:S, which coincides with the chemical formula of gypsum/anhydrite (Fig. 4.5D). The high birefringence combined with SEM-EDS analyses indicate that the inclusions are probably anhydrite rather than its hydrated form.

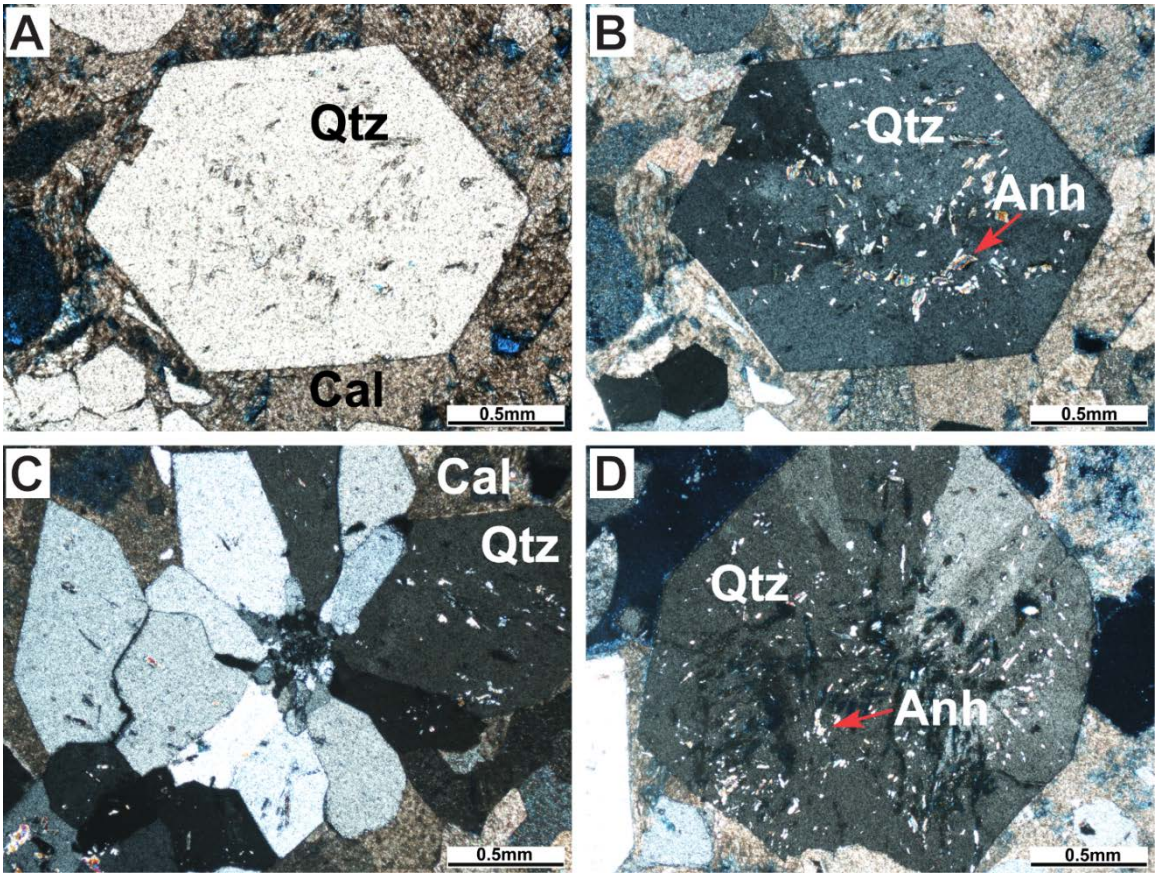


**Figure 4.4**: Euhedral megaquartz with quasi-hexagonal crystal habit: (A) plane-polarized light with calcite (Cal) surrounding quartz crystal; (B) cross-polarized image of the same field of view. Quartz (Qtz) crystals appear to have undulose extinction with anhydrite (Anh) inclusions, as indicated by red arrow; (C) drusy quartz with zoned holes in center which probably were produced by dissolution of anhydrite, cross-polarized light; (D) quartz with nearly fibrous extinction. Patches of elongate vacuoles and anhydrite laths are common (red arrow).

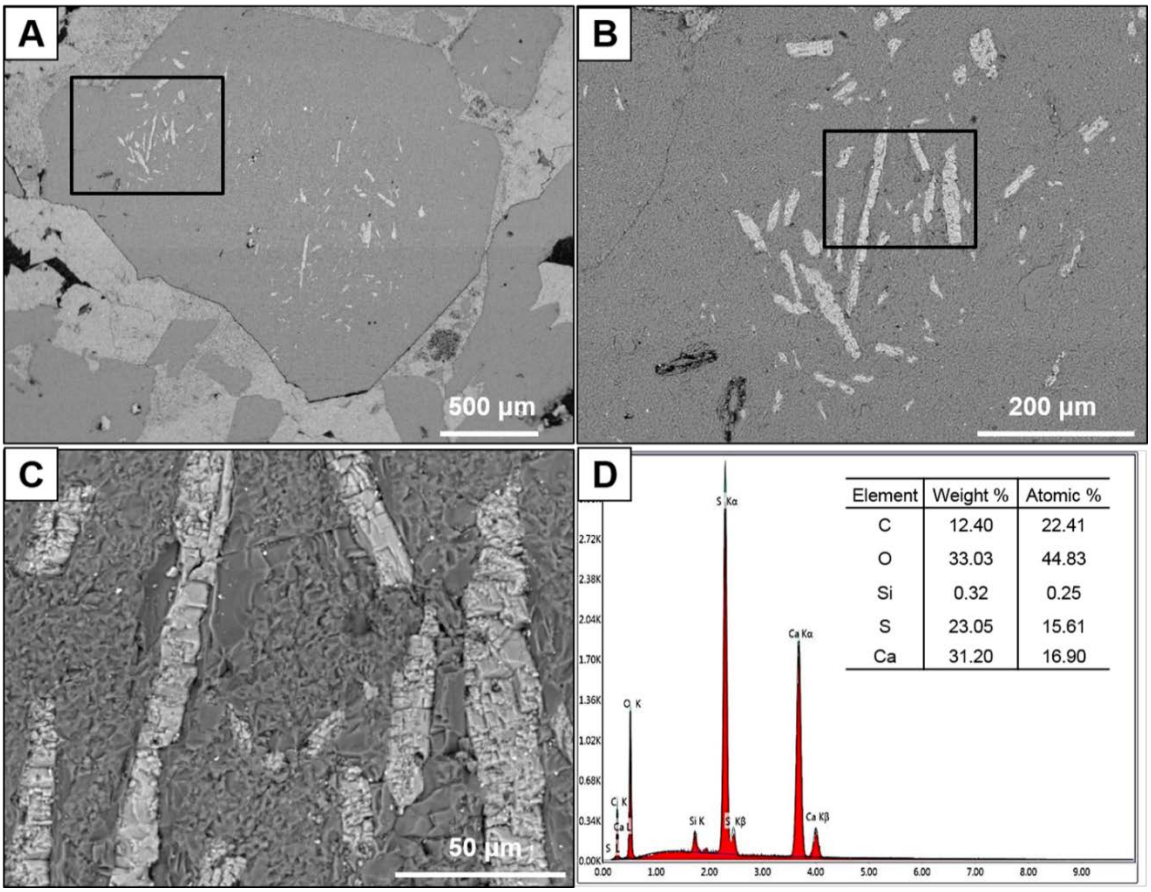


**Figure 4.5**: Backscattered electron (BSE) images of quartz crystals (A) with anhydrite inclusions; (B) close-up view of the black box in (A); and (C) close-up view of the black box in (B). The distinctive cleavage perpendicular to the long axis of the inclusions (light gray) in (C) is indicative of anhydrite ($CaSO_4$) crystals. (D) shows a typical EDS spectrum of the inclusions and the quantitative results are shown in the inserted table.

### 4.4.2 XRD

X-ray diffraction results indicate that the host carbonates, which were in direct contact with euhedral megaquartz crystals, have been partially dolomitized (60 % dolomite) (Fig. 4.6). Some cross-stratified carbonate samples that are subjacent to the quartz horizon however are composed almost 100 % of calcite, showing no sign of dolomitization.

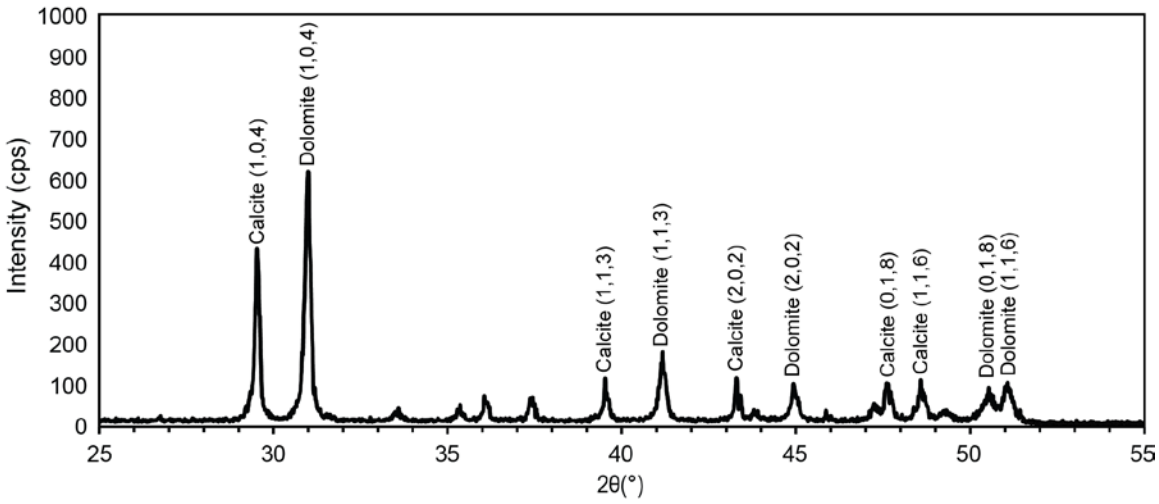


**Figure 4.6**: X-ray diffraction pattern of the carbonates in which authigenic quartz crystals were found. The peak intensity ratios of the principle dolomite (2θ = 30.96°) and calcite (2θ = 29.40°) reflections were measured and then fit to the calibration curves by Royse et al. (1971) to determine the relative degree of dolomitization.

### 4.4.3 Si isotopes

*In situ* and bulk silicon isotope data from four megaquartz samples of the Edwards Formation and two HD samples are shown in Fig. 4.7. The isotope compositions follow mass-dependent fractionation lines for all the samples (Supplement Fig. S2). The complete dataset is listed in Table 4.3. The $\delta^{30}$Si values of the euhedral megaquartz samples measured in this study show an approximate 6 ‰ range, from -2.90 to +2.94 ‰ with a mean value of -0.29 ‰ (n = 112). An Inverse Distance Weighting (IDW) interpolation method was employed to model the distribution of $\delta^{30}$Si values from a single grain. The results of the interpolation are shown in Fig. 4.8. The distribution of $\delta^{30}$Si values in each measured megaquartz sample show great heterogeneity even on a sub-millimeter scale. The $\delta^{30}$Si values range from -2.90 to +1.25 ‰ in Qtz1, from -2.72 to +2.94 ‰ in Qtz4, from -1.13 to +2.62 ‰ in Qtz6, and from -2.16 to +2.14 ‰ in Qtz7. Each quartz grain shows at least

individual quartz crystals resulted in similar slopes, which also suggests that the measurement by LA-ICP-MS is reliable. Qtz1 and Qtz4 have bulk compositions that are close to the mean value of the laser ablation measurements, while Qtz6 and Qtz7 have heavier bulk Si isotope composition than the mean value of their *in situ* measurements. It is important to note that the *in situ* measurements only represent a two-dimensional slice of the entire quartz crystal, therefore may not necessarily represent the bulk composition, especially with the great heterogeneity of $\delta^{30}$Si values in these authigenic quartz crystals. In contrast, the HD samples are relatively homogeneous which show $\delta^{30}$Si values (+0.85 to +2.08 ‰) with most measurements clustering around a mean value of +1.45±0.65 ‰ (2SD, n = 22), which is within error of the bulk value of +1.66±0.16 ‰. The result is in agreement with the observation by Douthitt (1982), who measured one HD quartz sample from New York and got a $\delta^{30}$Si value of +1.4±0.3 ‰, which also confirms the accuracy of the LA-MC-ICP-MS measurements in this study.

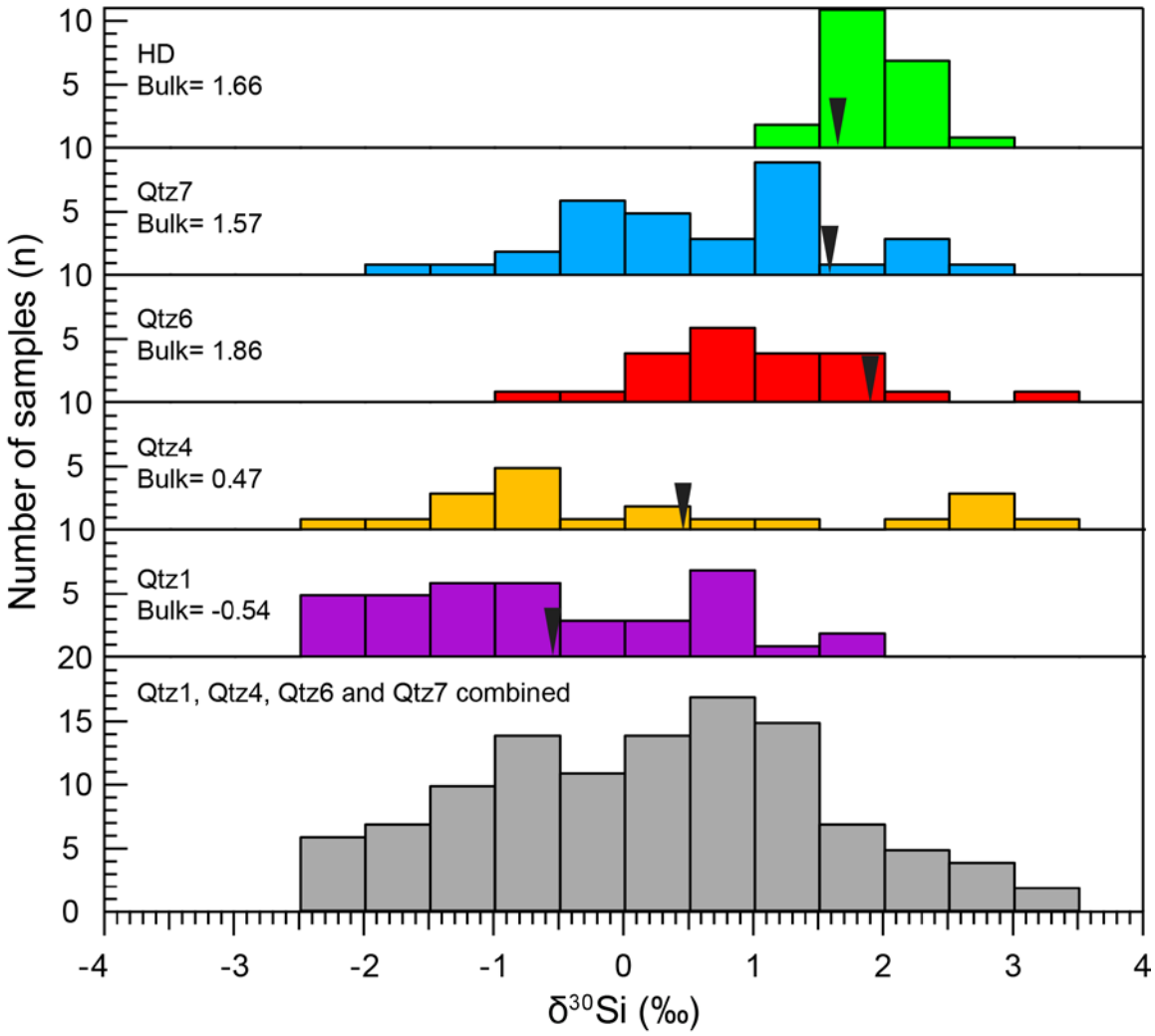


**Figure 4.7**: Plot shows the range of $\delta^{30}Si$ values for the four megaquartz crystals and the Herkimer Diamond (HD) samples measured in this study. $\delta^{30}Si$ values range from -2.91 to +1.25 ‰ in Qtz1, from -2.72 to +2.94 ‰ in Qtz4, from -1.13 to +2.62 ‰ in Qtz6, and from -2.16 to +2.14 ‰ in Qtz7. Herkimer Diamond is relatively homogeneous which shows only ~ 1 ‰ range of $\delta^{30}Si$ with a mean value of +1.45±0.65 ‰ (2SD, n = 22). Bars indicate the bulk values of each sample.

**Table 4.3**: *In situ* and bulk Si isotope data for megaquartz from the Edwards Formation.

| Sample spot | $\delta^{30}Si$ (‰) | 2S.E.** | $\delta^{29}Si$ (‰) | 2S.E. | Sample spot | $\delta^{30}Si$ (‰) | 2S.E. | $\delta^{29}Si$ (‰) | 2S.E. |
|---|---|---|---|---|---|---|---|---|---|
| Qtz1_p1 | -2.79 | 0.32 | -1.55 | 0.41 | Qtz1_p37 | 0.10 | 0.28 | -0.09 | 0.31 |
| Qtz1_p2 | -2.59 | 0.29 | -1.68 | 0.32 | Qtz1_p38 | -0.14 | 0.44 | -0.61 | 0.53 |
| Qtz1_p3 | -2.59 | 0.46 | -1.89 | 0.53 | Qtz4_p1 | 2.46 | 0.46 | 1.38 | 0.45 |
| Qtz1_p4 | -2.17 | 0.46 | -0.78 | 0.35 | Qtz4_p2 | 2.94 | 0.44 | 1.60 | 0.48 |
| Qtz1_p5 | -1.80 | 0.38 | -1.11 | 0.45 | Qtz4_p3 | 0.62 | 0.45 | 0.22 | 0.60 |
| Qtz1_p6 | 0.00 | 0.42 | -0.13 | 0.34 | Qtz4_p4 | 0.28 | 0.43 | 0.02 | 0.52 |
| Qtz1_p7 | -1.02 | 0.32 | -0.58 | 0.34 | Qtz4_p5 | -0.13 | 0.44 | 0.06 | 0.37 |
| Qtz1_p8 | -1.67 | 0.38 | -0.96 | 0.31 | Qtz4_p6 | -1.01 | 0.52 | -0.82 | 0.56 |
| Qtz1_p9 | -1.23 | 0.35 | -0.76 | 0.38 | Qtz4_p7 | -2.02 | 0.35 | -0.64 | 0.37 |
| Qtz1_p10 | -1.78 | 0.19 | -1.26 | 0.29 | Qtz4_p8 | -1.03 | 0.53 | -0.59 | 0.60 |
| Qtz1_p11 | -2.52 | 0.30 | -1.02 | 0.35 | Qtz4_p9 | -1.11 | 0.38 | -0.76 | 0.32 |
| Qtz1_p12 | -2.29 | 0.30 | -1.40 | 0.38 | Qtz4_p10 | -1.62 | 0.32 | -0.53 | 0.45 |
| Qtz1_p13 | 0.06 | 0.29 | -0.02 | 0.24 | Qtz4_p11 | -1.99 | 0.33 | -1.24 | 0.34 |
| Qtz1_p14 | -0.37 | 0.27 | -0.27 | 0.26 | Qtz4_p12 | -2.72 | 0.27 | -1.24 | 0.25 |
| Qtz1_p15 | 0.69 | 0.26 | 0.16 | 0.36 | Qtz4_p13 | -1.04 | 0.53 | -0.24 | 0.63 |
| Qtz1_p16 | 1.25 | 0.37 | 0.58 | 0.38 | Qtz4_p14 | -1.12 | 0.40 | -0.69 | 0.45 |
| Qtz1_p17 | 0.16 | 0.48 | 0.14 | 0.53 | Qtz4_p15 | 1.60 | 0.64 | 0.67 | 0.71 |
| Qtz1_p18 | -0.71 | 0.28 | -0.49 | 0.41 | Qtz4_p16 | 2.22 | 0.43 | 1.22 | 0.41 |
| Qtz1_p19 | -1.17 | 0.37 | -0.74 | 0.41 | Qtz4_p17 | 2.08 | 0.58 | 1.35 | 0.52 |
| Qtz1_p20 | -1.26 | 0.38 | -0.78 | 0.37 | Qtz4_p18 | -0.97 | 0.33 | -0.26 | 0.37 |
| Qtz1_p21 | 0.49 | 0.35 | 0.40 | 0.24 | Qtz4_p19 | -1.91 | 0.42 | -0.83 | 0.49 |
| Qtz1_p22 | -0.94 | 0.37 | -0.39 | 0.35 | Qtz4_p20 | -0.21 | 0.64 | -0.16 | 0.56 |
| Qtz1_p23 | -2.01 | 0.30 | -1.43 | 0.32 | Qtz6_p1 | -0.27 | 0.41 | -0.20 | 0.27 |
| Qtz1_p24 | -2.43 | 0.35 | -1.32 | 0.37 | Qtz6_p2 | -0.30 | 0.49 | -0.03 | 0.24 |
| Qtz1_p25 | -1.04 | 0.41 | -1.03 | 0.41 | Qtz6_p3 | 0.45 | 0.34 | 0.08 | 0.21 |
| Qtz1_p26 | -2.90 | 0.25 | -1.71 | 0.30 | Qtz6_p4 | 1.91 | 0.38 | 0.79 | 0.26 |
| Qtz1_p27 | -1.23 | 0.36 | -0.81 | 0.30 | Qtz6_p5 | -1.13 | 0.49 | -0.81 | 0.22 |
| Qtz1_p28 | -2.25 | 0.42 | -1.49 | 0.41 | Qtz6_p6 | 0.57 | 0.41 | 0.25 | 0.25 |
| Qtz1_p29 | -1.76 | 0.37 | -1.10 | 0.18 | Qtz6_p7 | 1.28 | 0.49 | 0.41 | 0.21 |
| Qtz1_p30 | -1.96 | 0.46 | -1.23 | 0.36 | Qtz6_p8 | 0.75 | 0.49 | 0.20 | 0.29 |
| Qtz1_p31 | 1.20 | 0.39 | 0.30 | 0.28 | Qtz6_p9 | -0.55 | 0.41 | -0.16 | 0.23 |
| Qtz1_p32 | -1.88 | 0.37 | -0.98 | 0.37 | Qtz6_p10 | 0.01 | 0.45 | 0.11 | 0.16 |
| Qtz1_p33 | -0.15 | 0.33 | 0.07 | 0.45 | Qtz6_p11 | 0.20 | 0.53 | 0.20 | 0.20 |
| Qtz1_p34 | -0.78 | 0.35 | -0.49 | 0.36 | Qtz6_p12 | 1.23 | 0.60 | 0.59 | 0.29 |
| Qtz1_p35 | 0.13 | 0.36 | -0.33 | 0.34 | Qtz6_p13 | 1.11 | 0.64 | 0.10 | 0.24 |
| Qtz1_p36 | 0.34 | 0.30 | 0.04 | 0.38 | Qtz6_p14 | 0.02 | 0.41 | -0.10 | 0.19 |

| Sample spot | $\delta^{30}Si$ (‰) | 2S.E. | $\delta^{29}Si$ (‰) | 2S.E. | Sample spot | $\delta^{30}Si$ (‰) | 2S.E. | $\delta^{29}Si$ (‰) | 2S.E. |
|---|---|---|---|---|---|---|---|---|---|
| Qtz6_p15 | 0.42 | 0.36 | 0.20 | 0.28 | Qtz7_p23 | -0.72 | 0.29 | -0.52 | 0.22 |
| Qtz6_p16 | 0.65 | 0.45 | 0.27 | 0.27 | Qtz7_p24 | -0.49 | 0.37 | -0.47 | 0.25 |
| Qtz6_p17 | 2.62 | 0.41 | 1.31 | 0.21 | Qtz7_p25 | 0.73 | 0.35 | 0.32 | 0.21 |
| Qtz6_p18 | 0.06 | 0.31 | 0.05 | 0.20 | Qtz7_p26 | -0.42 | 0.37 | -0.20 | 0.22 |
| Qtz6_p19 | 1.46 | 0.45 | 0.73 | 0.25 | Qtz7_p27 | 0.59 | 0.36 | 0.14 | 0.21 |
| Qtz6_p20 | -0.34 | 0.49 | -0.35 | 0.19 | Qtz7_p28 | 0.35 | 0.29 | -0.05 | 0.11 |
| Qtz6_p21 | -0.47 | 0.34 | -0.59 | 0.16 | Qtz7_p29 | 1.62 | 0.31 | 0.48 | 0.14 |
| Qtz6_p22 | 0.51 | 0.33 | 0.17 | 0.18 | Qtz7_p30 | 2.14 | 0.30 | 1.06 | 0.34 |
| Qtz7_p1 | 1.49 | 0.45 | 0.73 | 0.23 | Qtz7_p31 | -0.39 | 0.41 | -0.04 | 0.20 |
| Qtz7_p2 | -0.82 | 0.60 | -0.54 | 0.28 | Qtz7_p32 | 0.20 | 0.53 | 0.11 | 0.19 |
| Qtz7_p3 | -0.72 | 0.30 | -0.22 | 0.20 | HD1_1 | 1.97 | 0.36 | 0.80 | 0.37 |
| Qtz7_p4 | 0.21 | 0.64 | 0.15 | 0.24 | HD1_2 | 1.80 | 0.29 | 1.01 | 0.26 |
| Qtz7_p5 | -0.11 | 0.35 | -0.25 | 0.23 | HD1_3 | 1.31 | 0.37 | 0.72 | 0.49 |
| Qtz7_p6 | -0.96 | 0.32 | -0.53 | 0.28 | HD1_4 | 1.56 | 0.36 | 0.46 | 0.37 |
| Qtz7_p7 | 0.61 | 0.38 | 0.32 | 0.25 | HD1_5 | 1.85 | 0.37 | 0.81 | 0.45 |
| Qtz7_p8 | 0.95 | 0.45 | 0.46 | 0.22 | HD1_6 | 1.27 | 0.31 | 0.60 | 0.34 |
| Qtz7_p9 | -2.16 | 0.41 | -1.33 | 0.20 | HD1_7 | 1.61 | 0.30 | 1.11 | 0.19 |
| Qtz7_p10 | -1.22 | 0.45 | -0.59 | 0.21 | HD1_8 | 1.58 | 0.28 | 0.98 | 0.27 |
| Qtz7_p11 | 0.62 | 0.38 | 0.17 | 0.19 | HD1_9 | 1.81 | 0.40 | 0.82 | 0.32 |
| Qtz7_p12 | 0.62 | 0.26 | 0.38 | 0.22 | HD1_10 | 2.08 | 0.36 | 0.76 | 0.37 |
| Qtz7_p13 | -0.48 | 0.41 | -0.02 | 0.23 | HD2_1 | 1.42 | 0.19 | 0.71 | 0.25 |
| Qtz7_p14 | 1.53 | 0.30 | 0.83 | 0.13 | HD2_2 | 1.18 | 0.19 | 0.78 | 0.20 |
| Qtz7_p15 | -0.65 | 0.26 | -0.18 | 0.22 | HD2_3 | 1.19 | 0.14 | 0.54 | 0.18 |
| Qtz7_p16 | -1.14 | 0.41 | -0.46 | 0.28 | HD2_4 | 0.85 | 0.27 | 0.30 | 0.17 |
| Qtz7_p17 | 0.51 | 0.37 | 0.16 | 0.23 | HD2_5 | 0.95 | 0.23 | 0.27 | 0.26 |
| Qtz7_p18 | -0.56 | 0.38 | -0.18 | 0.23 | HD2_6 | 1.40 | 0.19 | 0.52 | 0.20 |
| Qtz7_p19 | 1.64 | 0.34 | 0.96 | 0.22 | HD2_7 | 1.48 | 0.27 | 0.55 | 0.28 |
| Qtz7_p20 | -1.56 | 0.60 | -1.22 | 0.34 | HD2_8 | 1.48 | 0.30 | 0.58 | 0.25 |
| Qtz7_p21 | 0.95 | 0.41 | 0.46 | 0.25 | HD2_9 | 1.00 | 0.33 | 0.76 | 0.21 |
| Qtz7_p22 | 0.90 | 0.45 | 0.26 | 0.19 | HD2_10 | 1.34 | 0.21 | 0.40 | 0.23 |
| | | | | | HD2_12 | 1.39 | 0.21 | 0.57 | 0.22 |

| Sample (Bulk) | $\delta^{30}Si$ (‰) | 2σ(n)** | $\delta^{29}Si$ (‰) | 2σ(n) | Sample (Bulk) | $\delta^{30}Si$ (‰) | 2σ(n) | $\delta^{29}Si$ (‰) | 2σ(n) |
|---|---|---|---|---|---|---|---|---|---|
| Qtz1 | -0.54 | 0.16(3) | -0.31 | 0.14(3) | Qtz4 | 0.47 | 0.29(2) | 0.14 | 0.13(2) |
| Qtz6 | 1.86 | 0.16(3) | 1.02 | 0.36(3) | Qtz7 | 1.57 | 0.20(2) | 1.07 | 0.19(2) |
| HD | 1.66 | 0.16(3) | 0.78 | 0.16(3) | | | | | |

*2 standard error from internal in-run statistics.

**2 standard deviation, number in parenthesis represents the number of analysis

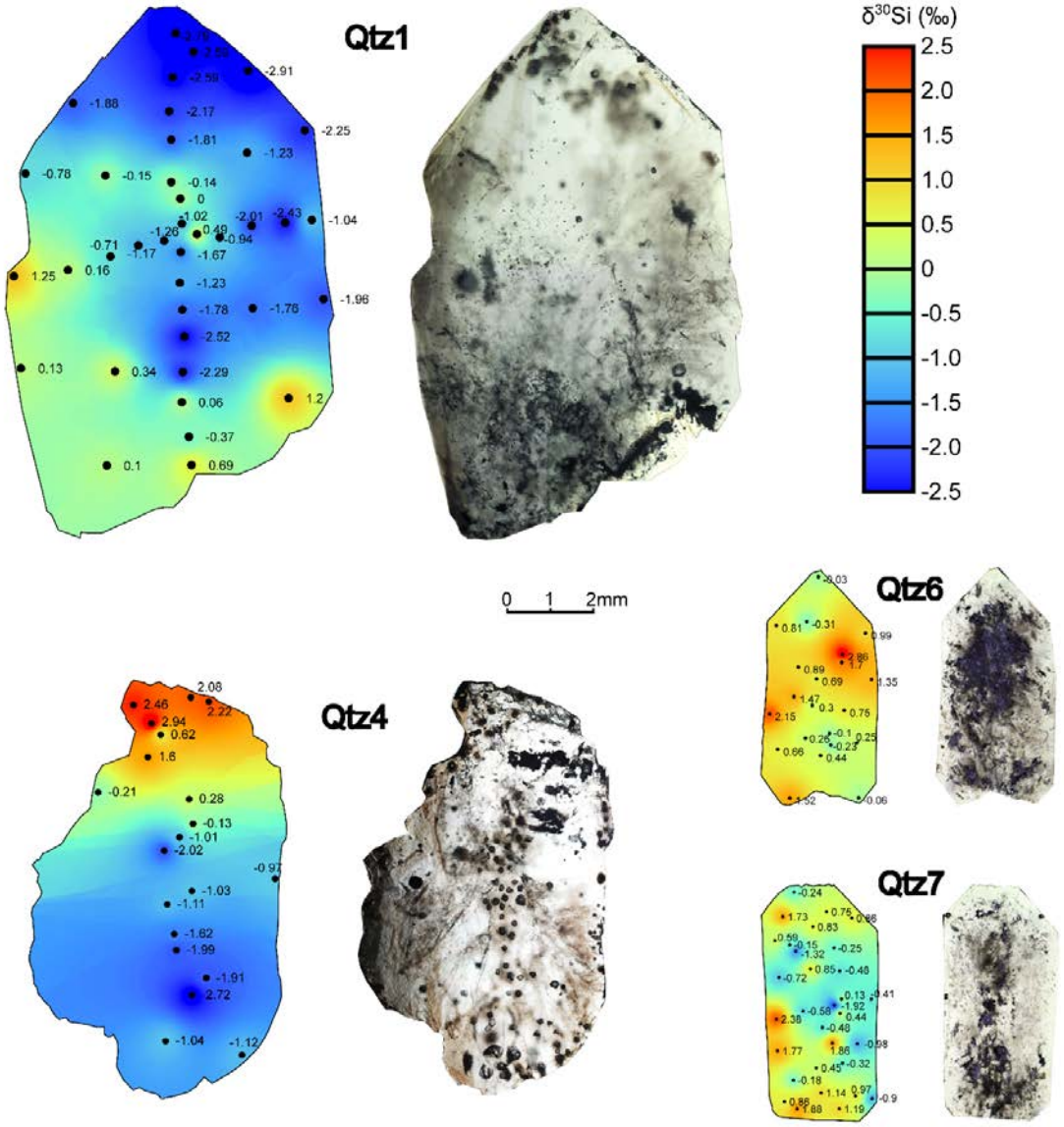


**Figure 4.8**: Inverse Distance Weighting interpolation of the $\delta^{30}Si$ values for the four megaquartz crystals depicted by the colors. Also shown for each sample is a transmitted light image. It can be seen that all four quartz crystals show quasi-hexagonal form.

## 4.5 Discussion

### 4.5.1 Depositional environment and source of Si

Petrographic observation and SEM analyses reveal the intimate relationship between silicification and evaporites formation for these samples. Chert nodules, silicified molluscan shells, length-slow chalcedony, and megaquartz have been widely documented in the Lower Cretaceous Edwards Formation in central Texas along the Balcones fault zone just south of the study area (Pittman, 1959; Folk and Pittman, 1971; Chowns and Elkins, 1974; Land and Prezbindowski, 1981; Woo et al., 1992). The presence of anhydrite and dolomite in the Edwards Formation suggests an arid evaporitive lagoonal environment. Fisher and Rodda (1969) noted that chert and dolomite in the Edwards Formation coexist in a belt marginal to the Kirschberg lagoon. The dolomite was thought to be formed by downward and outward migration of refluxing magnesium-enriched brines through reef-flank carbonate grainstones after the precipitation of anhydrite (Fisher and Rodda, 1969). Surface weathering may dissolve the primary dolomite and form pulverulite, as noted in previous studies (Rose, 1972; Chafetz and Butler, 1980). The anhydrite inclusions were leached to form open pores in some quartz crystals, indicating the silicification occurred after the primary precipitation of evaporite but prior to total dissolution of anhydrite. The association with evaporite has long been believed to have a causal relationship as precipitation and dissolution of sulfate altered the pH of the pore fluids and allowed the precipitation of quartz (Folk and Pittman, 1971; Milliken, 1979; Geeslin and Chafetz, 1982; Ulmer-Scholle et al., 1993; Chafetz and Zhang, 1998). The mixing of meteoric water with seawater can result in dissolution of dolomite and anhydrite and induce precipitation of silica (Knauth, 1992). Chert is absent from the quartz-rich layer but abundant within a few

meters in the underlying rudist-bearing carbonates. No siliciclastics have been found in the dolomitized facies, indicating the dissolution of siliciclastic fragments is not the source of the silica. The Lower Cretaceous carbonates in central Texas have been reported to contain abundant sponge spicules (Pittman, 1959), which is most likely to be the main source of silica in the silicification processes. The megaquartz likely originated from dissolution of sponge spicules from adjacent carbonates and reprecipitation in the porous dolomitized strata. The silicification likely took place during the early diagenesis prior to the total dissolution of evaporites.

### 4.5.2 Quartz formation mechanism

In this study, authigenic megaquartz crystals from Lake Georgetown Spillway display large variations of $\delta^{30}Si$ value, i.e., from -2.90 to +2.94 ‰. This range is interpreted using a two stage model modified from Marin et al. (2010) and Marin-Carbonne et al. (2012). In this model, amorphous silica from sponge spicules is dissolved until equilibrium concentration of amorphous silica is reached in pore fluids. These fluids are mixtures of meteoric water and seawater and oversaturated with respect to quartz. Thus, quartz starts to form until its equilibrium concentration is reached. The quartz crystals are found only in one particular very thin horizon in the carbonate strata, suggesting that they likely originated from the same parent pore fluids. If there were multiple generations of pore fluids, silicification would likely have taken place in multiple location.

In a closed system, dissolution of amorphous silica and crystallization of quartz will produce a range of $\delta^{30}Si$ values in a small length scale. Precipitation of quartz crystals

favors the light isotopes and the remaining fluids will be enriched in heavy isotopes. Therefore, the later stage of quartz precipitation will contain higher $\delta^{30}Si$ values until the solution reaches final quartz saturation (Marin-Carbonne et al., 2012). It is important to note that quartz crystals formed through this process may not necessarily grow continuously from core to rim. It is likely that megaquartz crystals accreted through nucleation and coalescence. The apparent random distribution of $\delta^{30}Si$ values in each quartz crystal implies that instead of slowly growing into a large crystal, it is likely that megaquartz crystals formed by accretion and aggregation from numerous nuclei that precipitate out of the pore fluids at different stages. Another line of evidence that supports this interpretation can be drawn from the fact that the anhydrite inclusions in the quartz crystals do not show preferred distribution. If the individual quartz crystals formed by continuous growths during early diagenesis while the evaporites were dissolving, the anhydrite would be incorporated more in the cores and less towards the rims. However, this is not observed in our quartz crystals. The undulose extinction pattern in quartz crystals also argues against a continuous growth origin. Therefore, the petrographic and isotopic evidence supports the hypothesis that these megaquartz crystals accreted by nucleation and aggregation from different stages of precipitation from the pore fluids that were enriched in silica from dissolution of sponge spicules.

The temperature of silicification is probably close to surface temperature or slightly higher due to the shallow burial depth. The surface air temperatures for the modern sabkhas in the Persian Gulf range from 16 to 44 °C and the annual temperatures at around 7 m depth range from 23 to 41 °C with an average of 32 °C (Butler, 1969). Milliken (1979) studied

the oxygen isotopes in similar megaquartz crystals associated with evaporites in Mississippian carbonate rocks from southern Kentucky and northern Tennessee and concluded that the temperature range of quartz formation varied from near-surface to less than 40 °C. The geothermal gradient in the Edwards is slightly higher than of the Mississippian carbonates (Milliken, 1979; Woodruff and Foley, 1985) so the temperature at shallow depth could have been somewhat higher. Similarly, oxygen isotopic ($\delta^{18}O$) analysis from well-preserved original calcite molluscs and cement in the Early Cretaceous Edwards Limestone revealed a relatively low paleotemperature (Land, 1977; Woo et al., 1992), in contrast to previously thought elevated Cretaceous temperatures. Woo et al. (1992) attributed the anomaly to the high salinity of the surface water in the ancestral Gulf of Mexico caused by evaporation and this interpretation is supported by the presence of anhydrite in the quartz crystals. Woo et al. (1992) used a temperature range of 23 to 30 °C as a representation for seawater temperature during the deposition of the Edwards Limestone. The exact temperature during quartz precipitation is unknown, but is likely in the range of 20 to 50 °C, slightly higher than the seawater temperature because the carbonate strata were never deeply buried.

### 4.5.3 Rayleigh-type kinetic fractionation model

At any temperature, the solubility of amorphous silica is always higher than that of quartz. Thus, the fraction of dissolved silica remaining in pore fluids (*f*) equals the ratio of the solubility ($R_s$) of quartz to amorphous silica (Marin-Carbonne et al., 2012). A successful model for the precipitation of megaquartz should meet two criteria. First, the kinetic process should reproduce the variation of $\delta^{30}Si$ values observed in the megaquartz samples

without *f* going to 0. Second, the final fraction (*f*) determined by the highest $\delta^{30}Si$ value in the megaquartz sample should correspond to a reasonable diagenetic temperature range.

The solubility reaction of both amorphous silica and quartz can be written as:

$$SiO_{2(s)} + 2H_2O_{(l)} = H_4SiO_{4(aq)} \quad (4.4)$$

Taking the activity of the solids and liquid water as unity, and the activity coefficient of $H_4SiO_4$ to be 1 because of its low concentration, being near the infinite dilution standard state, the equilibrium constant equals the solubility and is given by

$$K = m_{H_4SiO_4} \quad (4.5)$$

where $m_{H_4SiO_4}$ is in moles/l. At any given temperature, the solubility ratio of quartz vs. amorphous silica is

$$R_s = f = m_{quartz}/m_{am.silica} = K_{quartz}/K_{am.silica} \quad (4.6)$$

where $K_{am.silica}$ and $K_{quartz}$ are equilibrium constants for amorphous silica and quartz, respectively. Gunnarsson and Arnorsson (2000) calculated the solubility of amorphous silica and quartz at temperatures from 0 °C to 350 °C (Fig. 4.9) using the following equations:

$$\log K_{am.silica} = - 8.476 - 485.24 \times T^{-1} - 2.268 \times 10^{-6} \times T^2 + 3.068 \times \log T \quad (4.7)$$

$$\log K_{quartz} = - 34.188 + 197.47 \times T^{-1} – 5.851 \times 10^{-6} \times T^2 + 12.245 \times \log T \quad (4.8)$$

where T is temperature in Kelvin. Taking logarithms on both sides of equation (4.6) and substituting $\log K_{am.silica}$ and $\log K_{quartz}$ using equations (4.7) and (4.8) leads to:

$$\log R_s = \log f = -25.712 + 682.71 \times T^{-1} - 3.583 \times 10^{-6} \times T^2 + 9.177 \times \log T \quad (4.9)$$

Equation (4.9) links the diagenetic temperature with the solubility of silica. For instance, at 127 °C, a diagenetic fluid in which the dissolved silica is derived from dissolution of amorphous silica will saturate with respect to amorphous silica initially at around

514 µg/g. Precipitation of quartz will drive the fluid towards saturation of quartz at around 103 µg/g. The fraction of silica remaining in the solution at the end of the precipitation process (*f*) is determined by 102.7/513.5 = 0.2. Similarly, at 35 °C, the fraction of dissolved silica remaining in solution is 0.1 (Fig. 4.9).

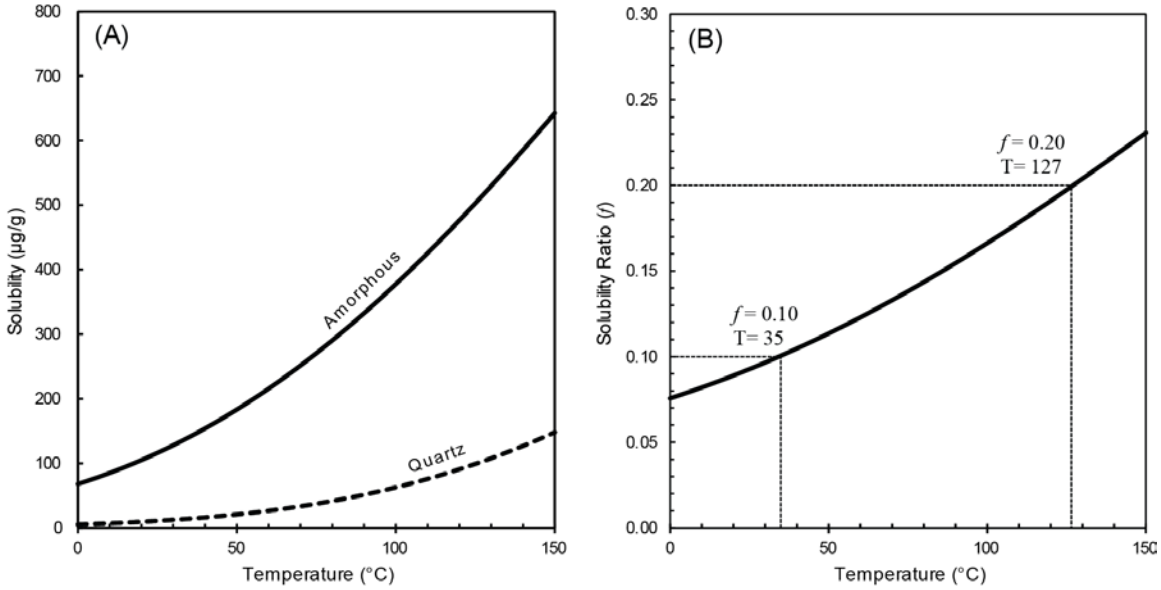


**Figure 4.9**: Plot (A) shows the solubility of both amorphous silica and quartz (Gunnarsson and Arnorsson, 2000). Plot (B) shows the relationship between solubility ratio (*f*) and temperature with examples showing diagenetic fluids at *f* = 0.10, and 0.20, which correspond to diagenetic temperature of 35 °C and 127 °C, respectively.

To further constrain the relationship between *f* and the $\delta^{30}Si$ in quartz precipitates, a Rayleigh-type kinetic fractionation model is applied which is based on the following equations:

$$\delta^{30}Si_{diss} = \delta^{30}Si_{initial} + \Delta^{30}Si_{prec\text{-}diss} \times \ln f \quad (4.10)$$

$$\delta^{30}Si_{prec} = \delta^{30}Si_{diss} + \Delta^{30}Si_{prec\text{-}diss} \quad (4.11)$$

where $\delta^{30}Si_{initial}$ is the $\delta^{30}Si$ value of the initial fluids before precipitation of quartz. $\delta^{30}Si_{prec}$ is the Si isotope composition of the precipitates at each particular increment, $\delta^{30}Si_{diss}$ is the Si isotope composition of the remaining fluids, $f$ is the fraction of Si remaining in the fluid, and $\Delta^{30}Si_{prec\text{-}diss}$ is the apparent isotopic fractionation between precipitated and dissolved silica. Previous models (van den Boorn et al., 2010; Chakrabarti et al., 2012) assumed $\delta^{30}Si_{initial}$ to be a known value and used that to calculate $\delta^{30}Si_{prec}$. Because of the difficulties in the estimation of the initial $\delta^{30}Si$ value, a reverse model is thus utilized by assuming a known value for the $\delta^{30}Si_{prec}$. Combining the above two equations will result:

$$\delta^{30}Si_{prec} = \delta^{30}Si_{initial} + \Delta^{30}Si_{prec\text{-}diss} \times (1 + \ln f) \quad (4.12)$$

Consider at the initial stage before precipitation occurs, all Si is in the solution and $f \approx 1$, thus $\ln f \approx 0$, and the first precipitate would have

$$\delta^{30}Si'_{prec} = \delta^{30}Si_{initial} + \Delta^{30}Si_{prec\text{-}diss} \quad (4.13)$$

where $\delta^{30}Si'_{prec}$ is the Si isotopic composition of the first precipitate. Substituting $\delta^{30}Si_{initial}$ in equation (4.12) using equation (4.13), we have

$$\delta^{30}Si_{prec} = \delta^{30}Si'_{prec} + \Delta^{30}Si_{prec\text{-}diss} \times (\ln f) \quad (4.14)$$

As discussed in Section 4.5.2, it is likely that the megaquartz crystals all originated from the same pore fluids. Multiple pulses of fluid migration may generate more than one zone of quartz crystals. The initial precipitate should have the lowest $\delta^{30}Si$ values as lighter isotopes are preferentially incorporated in the precipitates during chemical precipitation processes (Li et al., 1995; De La Rocha et al., 1997; Basile-Doelsch et al., 2005). Equation (4.14) thus can be used to calculate the $\delta^{30}Si$ composition for each incremental silica precipitation at given fraction ($f$). Using $f$ values from 0 to 1, the entire range of $\delta^{30}Si$ values

can be calculated. Precipitation stops when the solution reaches equilibrium with quartz. Equation (4.14) thus can be written as:

$$\delta^{30}Si''_{prec} = \delta^{30}Si'_{prec} + \Delta^{30}Si_{prec\text{-}diss} \times (\ln f'') \quad (4.15)$$

where $\delta^{30}Si''_{prec}$ represent the final increment of quartz precipitating from the solution and *f"* represent the fraction of silica remaining in the solution at that final stage, which is temperature dependent. Equation (4.15) can also be written as:

$$\ln f'' = (\delta^{30}Si''_{prec} - \delta^{30}Si'_{prec}) / \Delta^{30}Si_{prec\text{-}diss} \quad (4.16)$$

The lowest $\delta^{30}Si$ values observed in each megaquartz represents the initial precipitation of quartz from the solution and the highest $\delta^{30}Si$ value the final stage of quartz precipitation. Each individual spot in the quartz crystals represents one particular increment during precipitation. The value for $\Delta^{30}Si_{prec\text{-}diss}$ is unknown but can be modeled by iteration. Plugging in a range of values for $\Delta^{30}Si_{prec\text{-}diss}$ will result in a range of estimated values for *f"*, which is directly related to temperature during quartz precipitation (Fig. 4.9B). If the temperature can be well-constrained, the measured range of $\delta^{30}Si$ values in megaquartz crystals can help constrain the kinetic fractionation factor of Si isotopes during these shallow diagenetic processes using equation (4.16).

### 4.5.4 Constraints on abiotic Si fractionation factor $\Delta^{30}Si_{prec\text{-}diss}$

The kinetic Si isotope fractionation factor between precipitates and dissolved silica in fluids ($\Delta^{30}Si_{prec\text{-}diss}$) is still not well constrained in the literature. Large discrepancies exist between laboratory experiments and studies of natural samples (Li et al., 1995; Delstanche et al., 2009; van den Boorn et al., 2010; Chakrabarti et al., 2012; Geilert et al., 2014). Basile-Doelsch et al. (2005) used an average $\Delta^{30}Si_{prec\text{-}diss}$ value of -1.5 ‰ in their

pedogenic and groundwater silcrete studies. Other values of -2.3 ‰ (van den Boorn et al., 2010), -2.0 and -3.0 ‰ (Chakrabarti et al., 2012) have also been used in the literature for kinetic fractionation of Si isotopes between solids and fluids. Recent theoretical work by Dupuis (2015) suggested that $\Delta^{30}Si_{prec\text{-}diss}$ value at 27°C is +2.1 ‰ for equilibrium reactions, which is far from kinetic fractionation values.

During the quartz precipitation, the light isotopes are favored in the precipitates and the remaining fluids will be enriched in heavy isotopes. The $\Delta^{30}Si_{prec\text{-}diss}$ values therefore are negative as documented in previous studies. The Positive values for $\Delta^{30}Si_{prec\text{-}diss}$ are unlikely for kinetic processes as they will produce *f"* values higher than unity. In order to better constrain the abiotic fractionation factor $\Delta^{30}Si_{prec\text{-}diss}$, values from -3.0 to 0 ‰ are iteratively modeled using equation (4.16). The $\delta^{30}Si$ values for the initial to the final precipitates are given by the values observed from the four megaquartz crystals as well as the entire range for all the data combined. Extreme $\delta^{30}Si$ values in each megaquartz crystal are avoided by taking the 5 % and 95 % percentiles as representations for observed $\delta^{30}Si$ range. According to equation (4.16), each $\Delta^{30}Si_{prec\text{-}diss}$ value corresponds to a value for the fraction of silica remaining in the solution at that final stage (*f"*), which can be used to calculate the diagenetic temperature using equation (4.9) by iteration. The results are plotted in Figure 4.9. Equation (4.16) is not a temperature-dependent relationship for $\Delta^{30}Si_{prec\text{-}diss}$, but system dependent. For certain temperature, the model predicts the value for $\Delta^{30}Si_{prec\text{-}diss}$ required to reproduce the observed range of $\delta^{30}Si$ values in megaquartz crystals. Recent experimental study by Geilert et al. (2014) showed the true temperature-dependent relationship for $\Delta^{30}Si_{prec\text{-}diss}$.

As discussed in Section 4.5.2, based on the temperature range for quartz formation (20 to 50 °C), the $\Delta^{30}Si_{prec\text{-}diss}$ value is estimated to be between -1.8 to -2.1 ‰ using the whole range of $\delta^{30}Si$ values combined from all four quartz crystals from the Edwards Formation (Fig. 4.10). The models based on each individual quartz crystals seem to overestimate the values for $\Delta^{30}Si_{prec\text{-}diss}$. Individual crystals may have formed by aggregation of different stages during precipitation, which is unlikely to represent the whole range of $\delta^{30}Si$ values. Among the four crystals analyzed, Qtz4 displays the highest $\delta^{30}Si$ value (up to +2.94 ‰) as well as the widest range. Therefore, the model based on $\delta^{30}Si$ range of Qtz4 is in close agreement with the one using the whole range of $\delta^{30}Si$ values. Compared with previous estimation from natural samples, the fractionation factor estimated using the current model is in between the value of -1.5 ‰ used by Basile-Doelsch et al. (2005) and -2.3 ‰ used by van den Boorn et al. (2010). However, the current estimate is slightly lower compared to published experimental data. For example, Li et al. (1995) reported a range of -0.4 to -1.0 ‰ from silica gel precipitation. Geilert et al. (2014) suggested that the values for Si fractionation factor range from -1.1 to -1.5 ‰ at 20°C, and -1.2 ‰ at 35 °C based on flow-through experiments. Our estimation of $\Delta^{30}Si_{prec\text{-}diss}$ is on the same order of magnitude as Geilert et al. (2014). The discrepancy between the current estimation based on the *in situ* measurements on the quartz crystals can be partially explained by the differences in fluid salinities. The experimental studies were based on stock solution with significantly low salinity, whereas the pore fluids during quartz formation probably had much higher salinity. The reaction rate and saturation state of laboratory experiments are also likely different from the natural environments.

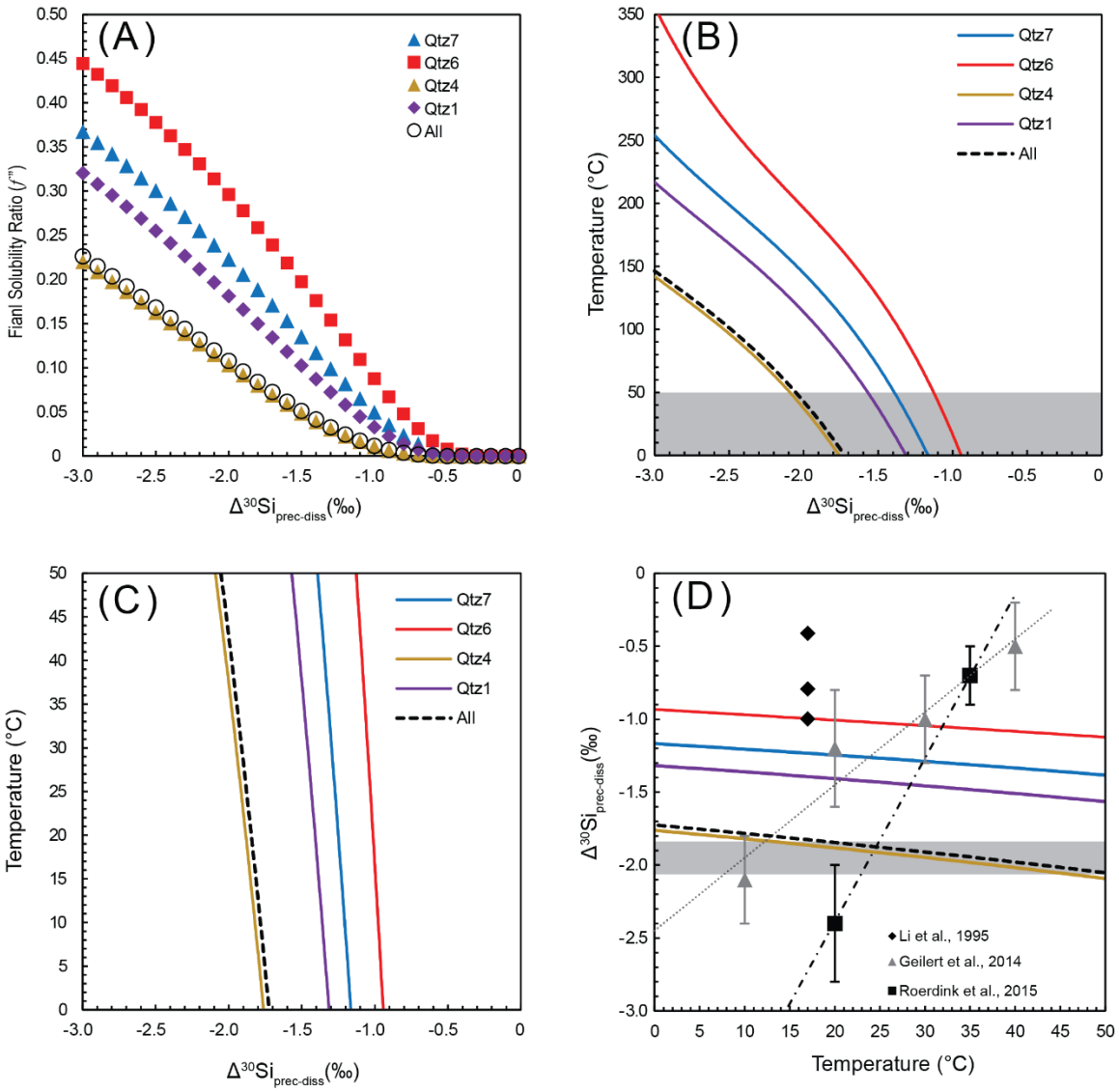


**Figure 4.10**: Rayleigh kinetic fractionation model using the $\delta^{30}Si$ values for all four megaquartz crystals as well as the entire range. Plot (A) shows the *f*' values with modeled $\Delta^{30}Si_{prec\text{-}diss}$ values using equation (16). Plot (B) shows the corresponding temperature calculated using equation (9), gray box represents temperature range from 0 to 50 °C, which is shown in plot (C). Plot (D) compares the current model and the published experimental data. Triangles represent data from Geilert et al. (2014) and squares are data from Roerdink et al. (2015) with dashed regression lines. Diamond represents silicon isotope fractionation from experimental precipitation of silica from Li et al. (1995). Gray box represents the best estimation of $\Delta^{30}Si_{prec\text{-}diss}$ values using the whole $\delta^{30}Si$ range combined from all four quartz crystals (Qtz1, Qtz4, Qtz6, and Qtz7).

### 4.5.5 Geochemical implications for Cretaceous seawater

Chakrabarti et al. (2012) reported a similar range of $\delta^{30}Si$ values in Precambrian chert samples (-4.29 to +2.85 ‰). They suggested that peritidal chert with relatively high $\delta^{30}Si$ values (-1.78 to +1.26 ‰) formed by early diagenetic replacement of shallow marine carbonates through precipitation from porewaters driven by evaporation. A closed system Rayleigh fractionation model (precipitate removed from the solution) was proposed to explain the 3 ‰ fractionation. In a study of Early Archean chert, van den Boorn et al. (2010) also observed a 3 ‰ variation in $\delta^{30}Si$ values (-2.4 to +1.3 ‰), which they also explained using a Rayleigh fractionation model. However, Chakrabarti et al. (2012) used a $\delta^{30}Si$ value of the initial fluids of +0.8 ‰ (thought to resemble the composition of dissolved Si in rivers), which differs from the value of -0.2 ‰ used by van den Boorn et al. (2010). Van den Boorn et al. (2010) concluded that a $\delta^{30}Si$ value of -0.2 ‰ was representative of Archean hydrothermal fluids. It is important to note that the Archean ocean Si cycle was not controlled by biologic activities, which is drastically different from the modern diatom dominated ocean and the "pre-diatom" ocean in the Phanerozoic, during which radiolaria and sponges were the main Si biomineralizing organisms (De La Rocha and Bickle, 2005). Average $\delta^{30}Si$ values of the dissolved silica from a "pre-diatom" ocean would have been much higher than the one in the modern ocean (De La Rocha and Bickle, 2005).

In the modern ocean, dissolved Si is dominantly in the form of silicic acid ($H_4SiO_4$). Marine silica-secreting organisms, particularly diatoms utilize the dissolved Si in seawater in assembling their opaline skeletons. The mean $\delta^{30}Si$ value of dissolved silica in modern seawater is +1.1 ‰ for surface waters (De La Rocha et al. 2000) and +0.9 ‰ for deep

waters. It is also been documented that the biologic uptake of Si is dependent on the concentration of $H_4SiO_4$ with greater fractionation in higher concentrations (Hendry and Robinson, 2012). Average concentration of $H_4SiO_4$ in modern seawater is only 2 µg/g, largely due to the draw down by diatoms (Treguer et al., 1995).

In contrast, Mesozoic oceans probably contained much higher concentrations of $H_4SiO_4$ as diatoms first appeared during the Jurassic and did not evolve to become the dominant marine producer of Si skeletons until the Oligocene (Wells, 1983; De La Rocha, 2007). This would result in a higher degree of fractionation between biogenic opal and dissolved silica in seawater. The fractionation factor between biologic opal and the dissolved silicic acid was estimated to be -1 ‰ for diatoms and -3.8 ‰ for marine sponges (De La Rocha et al., 1997; De La Rocha, 2003). The $\delta^{30}Si$ value of dissolved silica in seawater is probably variable in the geologic history (Robert and Chaussidon, 2006). Therefore, it is conceivable that a sponge dominated marine environment would have produced a different Si isotopic signature in dissolved silica in seawater. During the deposition of the Edwards Formation in the Cretaceous, the biogenic opal from sponge spicules dissolved and reprecipitated as authigenic quartz crystals during early diagenesis. The $\delta^{30}Si$ value of the quartz crystals may indirectly reflect the Si isotope composition of the dissolved silica in the seawater during the Cretaceous. Hence, the hypothesis that average $\delta^{30}Si$ values of the dissolved silica from a "pre-diatom" ocean is much higher than the one in the modern ocean can be tested.

The $\delta^{30}Si$ value of the initial fluids before precipitation of quartz ($\delta^{30}Si_{initial}$) can be computed using equation (4.13). The $\delta^{30}Si$ value of the initial increment of quartz precipi-

tate ($\delta^{30}Si'_{prec}$) can be represented by the lowest $\delta^{30}Si$ value observed (-2.90 ‰). The estimated range of $\Delta^{30}Si_{prec\text{-}diss}$ (-1.8 to -2.1 ‰), the $\delta^{30}Si$ value of the initial fluids is inferred to be between -1.1 to -0.8 ‰ ($\delta^{30}Si_{initial} = \delta^{30}Si'_{prec} - \Delta^{30}Si_{prec\text{-}diss}$). As discussed in Section 5.1, the initial Si content of the pore fluids likely derived from dissolution of sponge spicules in a shallow marine peritidal environment. The isotopic fractionation during dissolution of marine biogenic amorphous opal is negligible (Basile-Doelsch et al., 2005; Marin-Carbonne et al., 2012). Assuming that the Si fractionation factor for modern sponges (-3.8 ‰, De La Rocha, 2003) also applies to the Mesozoic sponges, it can be inferred that the seawater from which the sponges incorporate silica into their spicules must had an average $\delta^{30}Si$ value of +2.7 to +3.0 ‰. This value is within the range of estimated "pre-diatom" ocean waters by De La Rocha and Bickle (2005) (+1.9 to +4.6 ‰) but significantly higher than the average of modern seawaters (0.8 ‰). Although this range only reflects shallow marine seawaters in the peritidal areas, it is the first estimation of seawater Si composition in the Mesozoic.

## 4.6 Conclusions

The lithological association of evaporite-bearing dolomitized carbonate strata with rudist reefs suggests that the anhydrite likely developed in a back-reef tidal-flat environment. The occurrence of anhydrite inclusions in megaquartz crystals implies that precipitation of quartz crystals took place after the primary calcite cementation and only partial dissolution of evaporite, probably during very early stages of diagenesis. *In situ* silicon isotope measurements from four megaquartz samples of the Edwards Formation showed a

6 ‰ range, from -2.90 to +2.94 ‰. This large range of $\delta^{30}Si$ can be explained by a Rayleigh-type kinetic fractionation model, in which quartz precipitated from pore fluids that had an initial $\delta^{30}Si$ value of -1.1 to -0.8 ‰. Calculations of the solubility ratio between amorphous silica and quartz suggest that silicification occurred at surface temperature (20-50 °C). The fractionation factor of abiotic silica precipitation is estimated to be between -1.8 to -2.1 ‰, which is in strong agreement with previous estimates using natural silica samples. The source of Si is likely from the dissolution of amorphous opaline silica from sponge spicules. The estimated average $\delta^{30}Si$ value of the Early Cretaceous seawaters in the study area is +2.7 to +3.0 ‰, significantly higher than the average of modern seawaters.

# Chapter 5

# High temperature Si isotope geochemistry: Clues from the unique achondrite Northwest Africa 7325 (NWA 7325)

## Abstract

Ungrouped achondrite Northwest Africa (NWA) 7325 is a reduced, Mg-rich cumulate olivine gabbro that mainly consists of calcic plagioclase, diopside, and forsterite. The similarities in major elemental ratios and magnetic properties with the surface rocks of Mercury suggest that NWA 7325 may have originated from this planet. Oxygen isotope values of NWA 7325 differ from those of Earth, Mars, or known asteroids but are in the range of ureilites. However, Cr isotope compositions preclude a genetic link with ureilites. The U-Pb age of NWA 7325 is 4562.5±4.4 Ma, which is consistent with an Al-Mg age of 4562.8±0.3 Ma. This study analyzed the Si isotope compositions of NWA 7325 and a suite of meteorite and terrestrial rock samples to better understand its relationship to other planetary materials. NWA 7325 has a $\delta^{30}$Si value of -0.45±0.05 ‰ (n = 8), which is significantly lower than bulk silicate Earth (BSE) and angrites, but indistinguishable from chondrite. BSE has $\delta^{30}$Si values higher than chondrites, which led to the hypothesis that Si may have partitioned into the Earth's core during metal-silicate differentiation. However, angrites show $\delta^{30}$Si values even higher than BSE. Metal-silicate differentiation on the angrite parent body is unlikely because the relative small size and its oxidized conditions. Rather, it can be explained by nebular fractionation during forsterite condensation. Forsterite is

suggested to be the first solid to condense from the solar nebular, which can cause ~2 ‰ Si isotopic fractionation between solid and gas phases. Mixing between the forsterite and gas end-members can result in different $\delta^{30}$Si composition in planetesimals. The difference in $\delta^{30}$Si values between planetary materials could be caused by variable extents of forsterite and nebular gas mixing. Higher fraction of forsterite mixing with the nebular gas during APB accretion may have caused the higher $\delta^{30}$Si values observed in angrites. In this scenario, the $\delta^{30}$Si values for NWA 7325 may indicate that it accreted from materials that inherited similar proportions of early gas and condensates as chondrites, ureilites, Mars, and eucrites, but distinct from those of the angrite and aubrite parent bodies as well as the Earth-Moon system.

## 5.1 Introduction

Achondrites are stony meteorites that do not contain chondrules. They are relatively rare extraterrestrial materials, constituting about 4 % of known meteorites (Meteoritical Bulletin database). Achondrites typically form through various melting and crystallization processes in their parent bodies (e.g., asteroids) that have undergone different magmatic processes. As a result, studies of these meteorites can potentially provide insights into planetary differentiations and isotopic heterogeneity during the early stage of the solar system formation.

Achondrites are typically divided into the following two categories based on the degree of differentiation (i.e., textural and compositional similarities with chondrites): 1) primitive achondrites, those that have bulk chemical compositions similar to chondrites;

and 2) differentiated achondrites with highly fractionated bulk composition that originated from differentiated parent bodies. The silicate portion of some iron meteorites show many similarities with achondrites and therefore are also included in the classification (Mittlefehldt, 2014). The two main categories are further divided into several clans. A brief description of achondrite classification is given below.

### 5.1.1 Primitive achondrites

Primitive achondrites are derived from small parent bodies that experienced metamorphism and partial melting but never reached the temperature high enough for core-mantle differentiation. There are generally three clans in this supergroup: acapulcoite-lodranite clan, winonaite-IAB-iron silicate inclusion clan, and brachinites clan.

The acapulcoite-lodranite clan typically has chondritic composition but distinctive achondritic textures due to various degrees of high-temperature metamorphism and partial melting from original chondritic material. Oxygen isotopic compositions of acapulcoites and lodranites suggest that they form within a single parent body with isotopic heterogeneity (Clayton and Mayeda, 1996; Greenwood et al., 2012; Mettlefehldt, 2014). The winonaite-IAB-iron silicate inclusion clan contains members with chondritic compositions with metamorphic textures. The strong similarities in chemical, mineralogical, and oxygen isotopic compositions suggest that winonaites and IAB-iron silicate inclusions are from the same parent body that went through breakup and reassembly events during impact (Clayton and Mayeda, 1996; Benedix et al., 2000; Mittlefehldt, 2014). Brachinites are olivine-rich

primitive achondrites that originated from metamorphism and oxidation of chondritic material. Significant petrological and geochemical heterogeneity within the brachinites clan makes it difficult to interpret its petrogenesis.

### 5.1.2 Differentiated achondrites

Differentiated achondrites are igneous rocks that formed on asteroid bodies through partial to complete melting and magmatic crystallization processes (Mittlefehldt, 2014). This supergroup include angrites, aubrites, howardite-eucrite-diogenite (HED), mesosiderite silicates, shergottite-nakhlite-chassignite (SNC), and ureilites. Angrites are mafic igneous rocks formed in the crust of a differentiated asteroid as partial melting products under relatively oxidizing conditions (Mittlefehldt et al., 2002). Radiometric dating of angrites revealed that they are as old as the solar system, within ~2 Ma of CAI formation (Keil, 2012). Aubrites are reduced brecciated achondrites that have similar mineralogy and oxygen isotopic composition with enstatite chondrites (Clayton and Mayeda, 1996; Keil., 2010; Mittlefehld, 2014). The howardite-eucrite-diogenite clan is the most abundant suite of differentiated achondrites, which makes up about 75 % of all achondrites. Strong evidence suggests that 4 Vesta may be the parent body of HED meteorites, which may have undergone extensive melting and differentiation, forming a crust with eucritic composition in the shallow part and diogenitic components in the deeper region. The HEDs are mostly brecciated mafic and ultramafic igneous rocks that have been metamorphosed. Howardites are polymict breccias that represent the mixing of eucrites and diogenites (Mittlefehldt, 2014). Oxygen isotopic compositions of HEDs are identical, which is consistent with their origin

from a single parent body (Clayton and Mayede, 1996). Mesosiderite are stony iron meteorites with a silicate portion that has indistinguishable oxygen isotopic composition from that of the HEDs. The chemical composition and petrologic textures are highly similar to that of howardites, suggesting they may originated from the same parent body (Clayton and Mayede, 1996). Shergottite-nakhlite-chassignite (SNC) meteorites are commonly believed to be from Mars. They share the same oxygen isotopic composition, consistent with a single parent body origin. Ureilites are the second largest suite of achondrites, consisting of more than 20% of all achondrites, with characteristics of both primitive and diffentiated achondrites. Ureilites are ultramafic rocks, mostly unbrecciated, with a wide range of oxygen isotopic compositions, which is unique among all achondrites (Clayton and Mayede, 1996; Mittlefehldt, 2014).

### 5.1.3 Si isotope studies in meteorites

Previous studies of the chemical and oxygen isotopic compositions of achondrites have demonstrated that the different groups of achondrites originated from different parent bodies that underwent distinct differential processes (Clayton and Mayeda, 1996; Mittlefehldt, 2014). Whereas most achondrites can be grouped and associated with their parent bodies, there are others that have unique petrologic and compositional characteristics and are ungrouped. These ungrouped achondrites undoubtedly originated from previously unidentified differentiated parent bodies in the solar system and therefore, can provide valuable constraints for planet differentiation models and the chemical and isotopic evolution of the solar system.

Despite the ubiquity of Si in most terrestrial and meteorite samples, the application of stable silicon isotopic analysis ($^{28}Si$, $^{29}Si$, and $^{30}Si$) has been quite sparse compared to studies of oxygen isotopic composition. More recently, the advancements in analytical techniques, especially with the improvement of multi-collector inductively coupled plasma mass spectrometry (MC-ICP-MS), have allowed precise and accurate determination of small mass-dependent Si isotope fractionations resulting from high temperature planetary and magmatic processes. Recent studies of silicon isotope compositions have demonstrated significant $\delta^{30}Si$ variability among objects in the inner solar system (Georg et al., 2007; Fitoussi et al., 2009; Armytage et al., 2011; Zambardi et al., 2013). Bulk silicate Earth (BSE) and lunar rocks have similar $\delta^{30}Si$ values, both higher than the average of chondrites, whereas Martian and HED meteorites have near chondritic $\delta^{30}Si$ values (Georg et al., 2007; Fitoussi et al., 2009; Armytage et al., 2011; Zambardi et al., 2013; Savage et al., 2014; Dauphas et al., 2015). The difference in silicon isotope composition between BSE and chondrites has been attributed to Si isotopic fractionation between silicate and metals during core segregation on Earth, which can also explain the density deficit of the Earth's core relative to pure Fe-Ni alloy and the superchondritic Mg/Si ratio (Georg et al., 2007; Fitoussi et al., 2009; Armytage et al., 2011; Zambardi et al., 2013). However, angrites also display higher $\delta^{30}Si$ values relative to chondrites, but Si partitioned into the core of angrite parent body (APB) is unlikely because the redox conditions required for sufficient Si partitioning do not match that of APB (Pringle et al., 2014; Dauphas et al., 2015). The correlation between $\delta^{30}Si$ values and Mg/Si ratio in chondrites has led to the interpretation that the variation of $\delta^{30}Si$ among planetary bodies is caused by nebular fractionation during forsterite condensation rather than core segregation (Fitoussi et al., 2009; Dauphas et al., 2015). An

alternative explanation for the heavy Si isotope abundance in angrites is volatile loss during early accretional impacts (Pringle et al., 2014).

### 5.1.4 Ungrouped achondrite NWA 7325

The recently discovered ungrouped achondrite Northwest Africa (NWA) 7325 has drawn substantial attention because it was thought to be the first meteorite sample from planet Mercury (Irving et al., 2013). NWA 7325 is a reduced, Mg-rich cumulate olivine gabbro that mainly consists of calcic plagioclase, diopside, and forsterite (Irving et al., 2013) (Fig. 5.1). The similarities in major elemental ratios and magnetic properties with the surface rocks of Mercury suggest that NWA 7325 may have originated from this planet (Irving et al., 2013; Weiss et al., 2013). Bulk oxygen isotope compositions are in the range of ureilites, but texture and Cr isotope compositions preclude a genetic link with ureilites (Irving et al., 2013; Kita et al., 2014). Oxygen isotope values of mineral separates from NWA 7325 follow mass-dependent fractionations, but $\Delta^{17}O$ differs from those of Earth, Mars, and known asteroids (Jabeen et al., 2014; Kita et al., 2014). The U-Pb age of NWA 7325 is 4563.4±2.6 Ma, which is consistent with an Al-Mg age of 4563.09±0.26 Ma (Koefoed et al., 2016). The ancient formation age makes it unlikely that it originated from the evolved crust of a planetary-sized body (Dunlap et al., 2014). A recent study reported fractionated highly siderophile element (HSE) patterns of NWA 7325 relative to bulk chondrite; these data are interpreted to be the result of multi-stage metal-silicate partitioning on the parent body (Archer et al., 2015). Alternatively, an impact-melting of gabbroic material origin has been proposed to explain the HSE characteristics of NWA 7325 (Barrat et al.,

2015). Although the exact origin of NWA 7325 is still enigmatic, this rock remains interesting because of its unique petrologic and geochemical features. In this study, Si isotopic compositions of ungrouped achondrite NWA 7325 were measured to better understand its origin and its implications for early solar system processes.

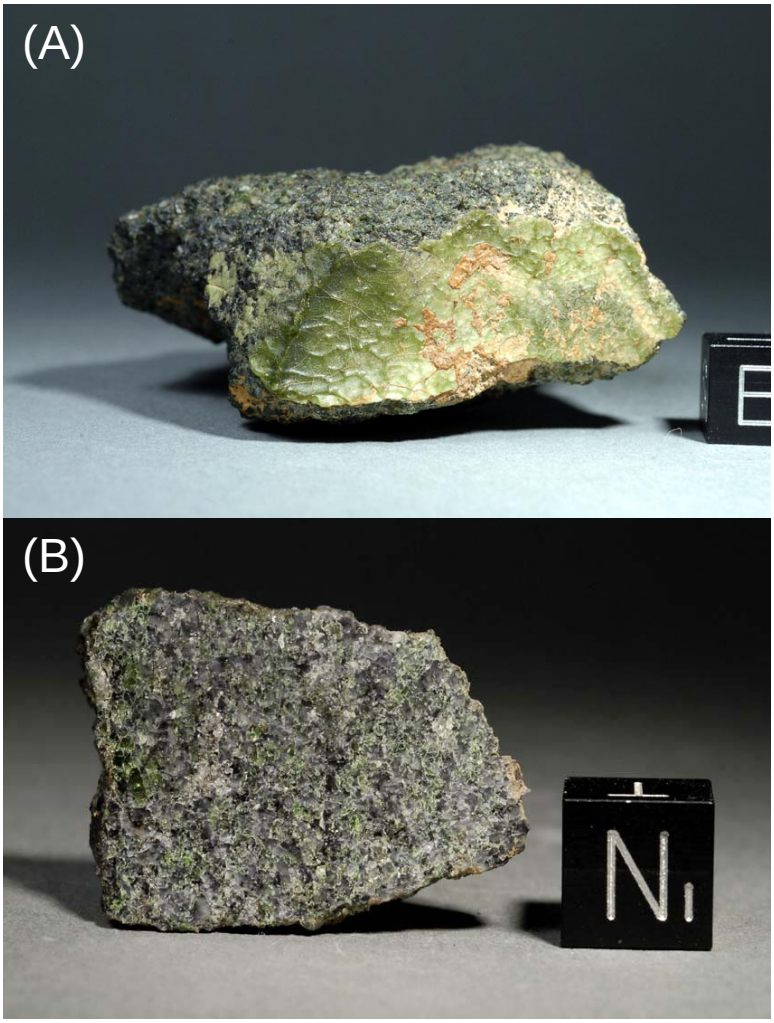


**Figure 5.1.** Photograph of NWA 7325. (A) One of the largest pieces of the meteorite showing distinctive green fusion crust; the size of the cube is 1 cm; (B) slice of NWA 7325 showing its unbrecciated structure; photo courtesy of Stefan Ralew.

## 5.2 Samples and analytical procedures

The silicon isotope compositions were measured using a MC-ICP-MS at University of Houston following the procedures detailed in previous chapters. Around 5 to 10 mg of sample material was mixed with one 200 mg NaOH pellet in a silver crucible (made in-house from 99.99% pure silver sheet, Alfa-Aesar) at 730 °C for 12 minutes. After slight cooling, the crucibles were dropped in 50 ml Teflon containers filled with 20 ml ultrapure water. After 24 hours, the containers were treated in an ultrasonic bath for 15 minutes to accelerate the dissolution process. Crucibles were subsequently removed and rinsed with ultrapure water, which was transferred into the Teflon container. The solution was then acidified using HCl (to avoid additional $NO^+$ polyatomic interference) and diluted. Bio-Rad (Bio-Rad laboratories Inc.) 50W-X8 (200-400 mesh) cation exchange resin was used to carry out the ion chromatography following the procedures described by Georg et al. (2006).

Si isotope analysis was conducted in medium resolution using a Nu Plasma II MC-ICP-MS with a resolving power of about 4000. Samples were introduced into the mass spectrometer by the Aridus II desolvating system (CETAC Technologies) with a micro-concentric Teflon nebulizer in dry plasma mode. The three Si isotopes ($^{28}Si$, $^{29}Si$, and $^{30}Si$) were measured simultaneously on the flat plateau of the Si peaks on the interference-free low mass end. A 60 s on-peak-zero baseline measurement was recorded for each analysis followed by peak centering. The typical background signal in $^{28}Si$ was ~ 3 mV. Each measurement consisted of 80 cycles each with 5 s of integration time, for a total of 400 s of on-

peak measurement. Instrumental mass bias and drift were corrected using a standard-sample-standard bracketing approach with NBS 28 as the bracketing standard, taken through the same digestion and chemical separation procedure as the samples. The results are reported with δ notation in per mil (‰) relative to NBS 28.

In addition to NWA 7325, Si isotope ratios were measured for a suite of geostandards and meteorite samples that include BHVO-2 (basalt, USGS), BIR-1a (basalt, USGS), Allende (CV3), NWA 3134 (EL6), Pena Blanca Springs (aubrite), EET 87520 (eucrite), NWA 1068 (shergottite), and NWA 4931 (angrite). Enstatite chondrite (EC) and aubrite samples were selected because they have lower $\delta^{30}$Si values relative to the average of carbonaceous chondrites (CC) and ordinary chondrites (OC) (Georg et al., 2007; Fitoussi et al., 2009; Armytage et al., 2011; Zambardi et al., 2013). These meteorite types and the terrestrial rock standards have been extensively analyzed for Si isotopes by various laboratories (Georg et al., 2007; Fitoussi et al., 2009; Armytage et al., 2011; Zambardi et al., 2013), giving a robust framework for the interpretation of our Si isotope data. Uncertainties are reported as 2SE.

## 5.3 Results

The complete dataset is given in Table 5.1. The $\delta^{30}$Si values of geostandards, chondrites, aubrite, and eucrite agree well with those reported in previous studies (Fig. 5.2) (Georg et al., 2007; Fitoussi et al., 2009; Armytage et al., 2011; Zambardi et al., 2013; Pringle et al., 2014; Dauphas et al., 2015). Si isotopic compositions of NWA 7325 and all other samples follow a mass-dependent fractionation line, which is expected as no mass-

independent fractionation has been reported for Si isotopes (Fig. 5.3). The two basalt standards BHVO-2 and BIR-1a yielded $\delta^{30}$Si values of -0.28±0.03 ‰ and -0.33±0.03 ‰, respectively. The shergottite sample yielded a $\delta^{30}$Si value of -0.37±0.04 ‰, which is within uncertainties of the range reported by (Armytage et al., 2011). The angrite sample NWA 4931 has the highest $\delta^{30}$Si value of -0.19±0.04 ‰ and the aubrite sample Pena Blanca Spring showed the lowest $\delta^{30}$Si value of -0.59±0.03 ‰. The ungrouped achondrite NWA 7325 has a $\delta^{30}$Si value of -0.45±0.05 ‰, which is significantly lower than for BSE and angrites, but indistinguishable from values for chondrites measured in this study or average $\delta^{30}$Si value for carbonaceous chondrites reported in the literature (Fig. 5.2) (Georg et al., 2007; Fitoussi et al., 2009; Armytage et al., 2011; Zambardi et al., 2013; Pringle et al., 2014; Dauphas et al., 2015). The Si isotope composition of NWA 7325 is also not resolvable from average $\delta^{30}$Si compositions of HEDs and Martian meteorites (Georg et al., 2007; Fitoussi et al., 2009; Armytage et al., 2011; Zambardi et al., 2013).

**Table 5.1**: $\delta^{30}$Si values for samples in this study. Uncertainties are given as 2SE. BSE=bulk silicate Earth, CC=carbonaceous chondrite, EC=enstatite chondrite, PBS=Peña Blanca Spring.

| Sample | Description | $\delta^{30}$Si (±2SE) | $\delta^{29}$Si (±2SE) | n |
|---|---|---|---|---|
| BHVO-2 | BSE | -0.27 (0.03) | -0.14 (0.02) | 22 |
| BIR-1a | BSE | -0.33 (0.03) | -0.16 (0.01) | 22 |
| Allende | CC | -0.42 (0.04) | -0.21 (0.02) | 22 |
| EET 87520 | Eucrite | -0.46 (0.05) | -0.23 (0.03) | 21 |
| PBS | Aubrite | -0.59 (0.03) | -0.29 (0.02) | 22 |
| NWA 3134 | EC | -0.52 (0.03) | -0.27 (0.02) | 22 |
| NWA 1068 | Shergottite | -0.37 (0.03) | -0.20 (0.02) | 9 |
| NWA 4931 | Angrite | -0.19 (0.04) | -0.07 (0.02) | 8 |
| NWA 7325 | Achondrite | -0.45 (0.05) | -0.23 (0.02) | 8 |

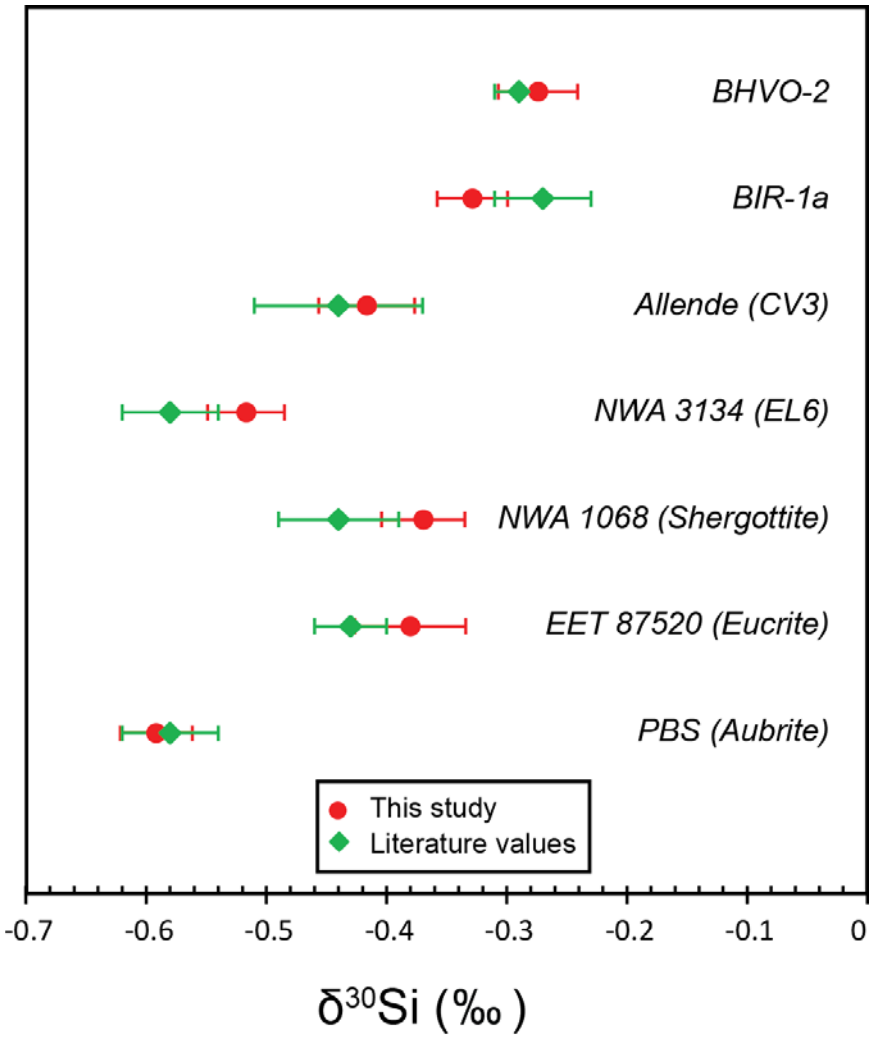


**Figure 5.2.** $\delta^{30}$Si values for geostandards and meteorite samples measured in this study agree well with literature data. BHVO-2: Fitoussi et al. (2009); Armytage et al. (2011); Savage et al. (2013); Zambardi et al. (2013). BIR-1a: Zambardi et al. (2013). CV3: Fitoussi et al. (2009); Armytage et al. (2011); Savage et al. (2013). EL6: Armytage et al. (2011); Savage et al. (2013). Shergottite: Armytage et al. (2011); Zambardi et al. (2013). Eucrite: Fitoussi et al. (2009); Armytage et al. (2011); Zambardi et al. (2013). Aubrite: Armytage et al. (2011); Savage et al. (2013).

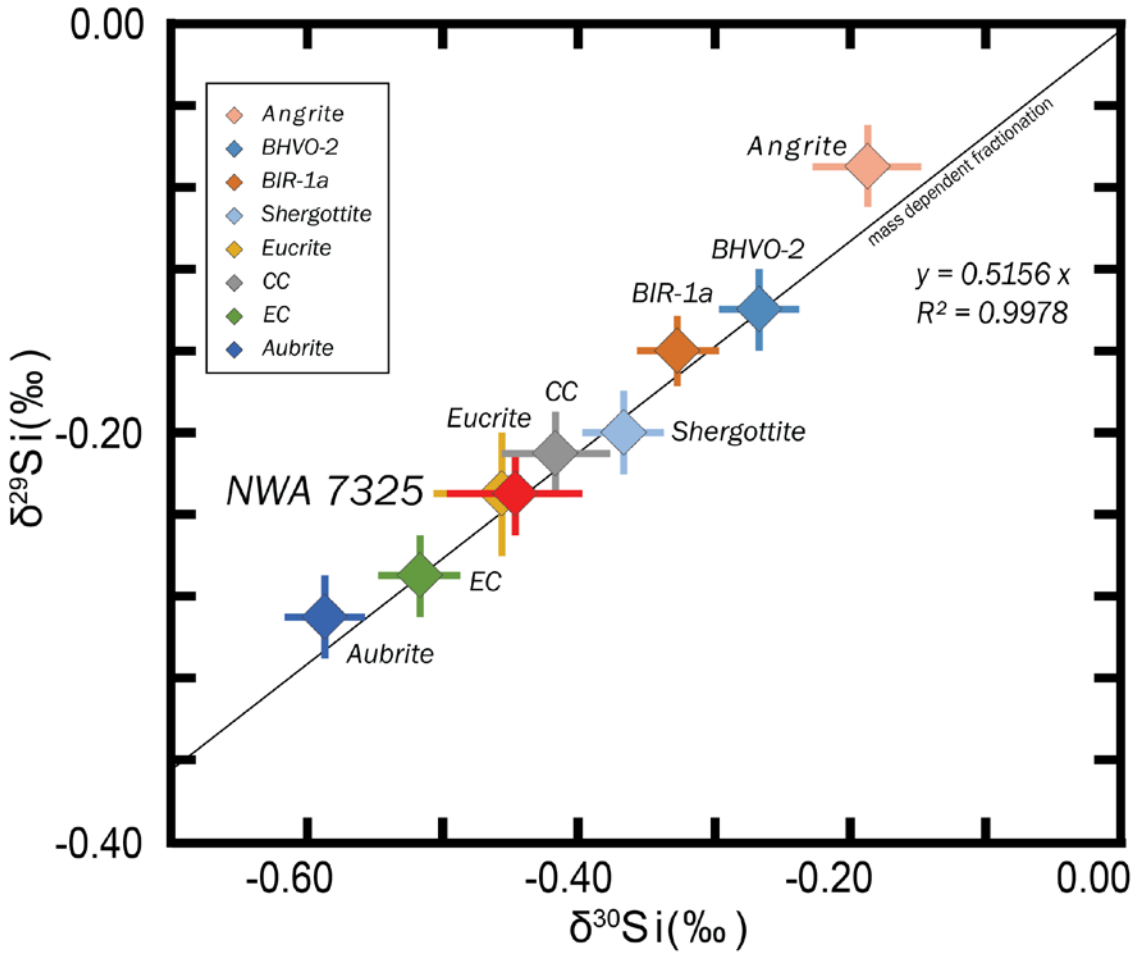


**Figure 5.3**: Si isotopic compositions of NWA 7325 and all other samples follow a mass-dependent fractionation line, which is expected as no mass-independent fractionation has been reported for Si isotopes. CC = carbonaceous chondrite, EC = enstatite chondrite.

## 5.4 Discussion

### 5.4.1 Silicon isotopic variations in the inner solar system

Recent studies by Savage et al. (2011) suggested that only mafic and ultramafic rocks are representative of the BSE. The basalt standard BHVO-2 yields $\delta^{30}$Si value of -0.28±0.03 ‰, which is in excellent agreement with the value of -0.29±0.07 ‰ (2SD) of

BSE proposed by Savage et al. (2014). BIR-1a yields a $\delta^{30}$Si value of -0.33±0.03 ‰, which is within uncertainty of BHVO-2 measured in this study. The average of the two basalt standards yield a $\delta^{30}$Si value of -0.30±0.03 ‰ as the representation of BSE.

Georg et al. (2007) first reported a significant offset in the silicon isotopic compositions between BSE and the average of all meterorites, including carbonaceous, ordinary, and enstatite chondrites, Martian meteorites, HEDs, and ureilites. Studies since then have not all agreed on the exact magnitude of the offset, which may be due to different analytical procedures. But most studies suggested that BSE has a higher $\delta^{30}$Si values than the average of chondrites. Chondrites have not experienced large scale melting or metal-silicate differentiation, and therefore are thought to represent the building blocks of many planetesimals during the early solar system formation.

Subsequent work by Fitoussi et al. (2009) further suggested a heterogeneous distribution of Si isotopes within chondrite groups, with enstatite chondrite having the lowest $\delta^{30}$Si values. Enstatite chondrites formed in relatively reducing conditions, which may have facilitated Si isotope fractionation between metal and silicate, resulting in extremely low $\delta^{30}$Si values in the metal phase and the bulk enrichment of light Si isotopes in enstatite chondrites. This makes the estimation of the Si isotopic composition of chondrite more challenging. Fitoussi et al. (2009) only used carbonaceous chondrites as the average for chondrites with a $\delta^{30}$Si value of -0.36±0.04 ‰ (1SD). Savage et al. (2014) suggested using the average of carbonaceous chondrites, ordinary chondrites, and achondrites as the representation of average for meteorites with a $\delta^{30}$Si value of -0.46±0.09 ‰ (2SD), which is identical to the average of carbonaceous chondrites in their study. Although Martian meteorites and HEDs show chondritic $\delta^{30}$Si values, several studies have demonstrated variation

of $\delta^{30}$Si values within achondrite groups (Fitoussi et al., 2009; Armytage et al., 2011; Pringle et al., 2014; Dauphas et al., 2015). Furthermore, study by Fitoussi et al. (2009) reported small but distinguishable difference in $\delta^{30}$Si values between carbonaceous and ordinary chondrites, which may be correlated to the difference in the elemental Mg/Si ratio. Thus in this study, the average $\delta^{30}$Si values of carbonaceous chondrites from the literature are taken as the representation for the average of chondrites, which yields an average $\delta^{30}Si_{cc}$ of -0.44±0.07 ‰. The only carbonaceous chondrite sample measured in this study was Allende (CV3) which yielded a $\delta^{30}$Si value of -0.42±0.04 ‰, within the estimated range of $\delta^{30}Si_{cc}$ (Fig. 5.4).

Martian meteorites (SNC) and HEDs have been demonstrated to have bulk $\delta^{30}$Si values indistinguishable from the average of chondrites (Armytage et al., 2011; Zambardi et al., 2013). The shergottite sample NWA 1068 in this study showed a slightly higher $\delta^{30}$Si value of -0.37±0.04 ‰, but is within uncertainties of the range reported by (Armytage et al., 2011). The eucrite sample EET 87520 also has chondritic $\delta^{30}$Si value -0.46±0.05 ‰ (Fig. 5.3). However, other achondrites groups show greater variation in Si isotopic compositions. For example, studies have shown that aubrites have a much lower $\delta^{30}$Si values (-0.58±0.02 ‰) than chondrites (Armytage et al., 2011; Savage et al., 2013) whereas angrites show higher $\delta^{30}$Si values (-0.21±0.03 ‰) than chondrites and BSE (Dauphas et al., 2015). The $\delta^{30}$Si value of -0.59±0.03 ‰ for aubrite sample Pena Blanca Spring and the value of -0.19±0.04 ‰ for the angrite sample NWA 4931 agree well with previous studies (Fig. 5.3) (Armytage et al., 2011; Savage et al., 2013; Zambardi et al., 2013; Dauphas et al., 2015).

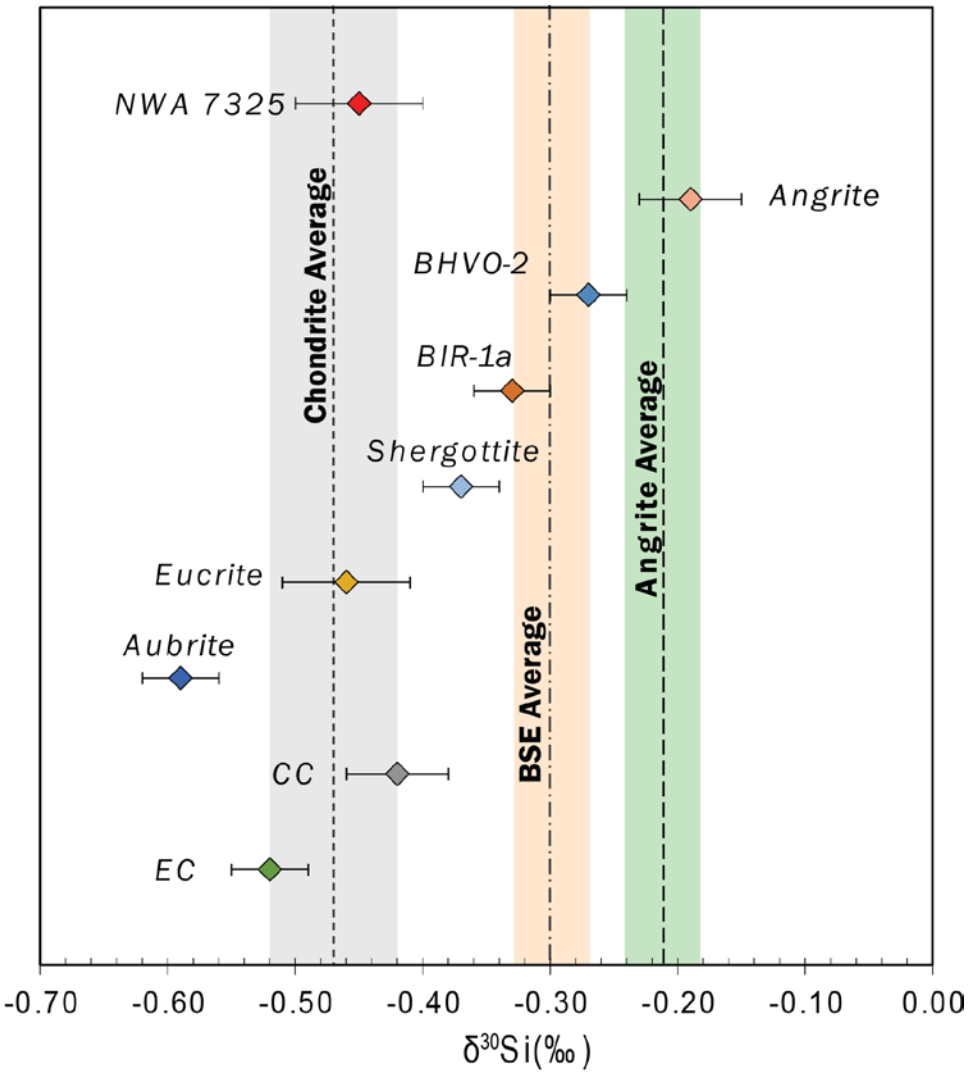


**Figure 5.4**: Silicon isotopic composition of NWA 7325 compared with values for the bulk silicate Earth (BSE) and other meteorite samples (CC=carbonaceous chondrite, EC=enstatite chondrite). Data with error bars are from this study. Data for BSE and chondrite average is taken from Georg et al. (2007); Fitoussi et al. (2009); Armytage et al. (2011) and Zambardi et al. (2013). Angrite average is from Dauphas et al. (2015). Uncertainties are reported as 2SE.

### 5.4.2 Metal-silicate differentiation or nebular fractionation?

The offset in silicon isotope composition between BSE and chondrites can be explained by equilibrium Si isotopic fractionation between silicate and metals during core-

mantle differentiation if a significant amount of Si entered the core. This hypothesis also explains the density deficit of the Earth's core relative to pure Fe-Ni alloy and the super-chondritic Mg/Si ratio (Georg et al., 2007; Fitoussi et al., 2009; Armytage et al., 2011; Zambardi et al., 2013). The chondrite-like $\delta^{30}$Si compositions of Mars and 4-Vesta have been ascribed to the lack of Si isotopic fractionation between silicate and metals due to the relative small sizes of these bodies (Armytage et al., 2011; Zambardi et al., 2013).

However, several lines of evidence have been proposed that argue against core-mantle fractionation being the main reason why BSE has higher $\delta^{30}$Si values. Firstly, BSE displays distinctive signatures in several elements, such as O, Ca, Cr, Ti and Ni (Clayton, 1993; Dauphas et al., 2014), which can be explained by mixing of different proportions of chondritic material. But no plausible mixing model can explain the offset in the Si isotopes because it would require a reservoir with very high $\delta^{30}$Si values. Enstatite chondrites have the closest elemental compositions to BSE but extremely low $\delta^{30}$Si values, which would require more than 20 wt.% of Si in Earth's core (Fitoussi and Bourdon, 2012; Zambardi et al., 2013). Secondly, core segregation in early accreted planetesimals may be unlikely to reach the temperature and pressure required for sufficient Si partitioning into a metal phase (Armytage et al., 2011; Zambardi et al., 2013; Dauphas et al., 2015). For example, angrites display higher $\delta^{30}$Si values relative to chondrites, but Si partitioned into the core of angrite parent body (APB) is unlikely because the redox conditions required for sufficient Si partitioning do not match that of APB (Pringle et al., 2014; Dauphas et al., 2015). The conditions for Si to become siderophile, i.e., partitioning into the core during metal-silicate differentiation, must either be high temperature or low oxygen fugacity (Dauphas et al., 2015). Angrites formed within the first 4 Myr after the start of the solar system, which probably

indicate that they originated from a small parent body as the igneous processes in a larger parent body would erase the earlier magmatic history. The estimated temperature and oxygen fugacity for APB was around 1400 °C and IW-1, respectively (Righter, 2008; Scott and Bottke, 2011; Dauphas et al., 2015). Based on experiments and theoretical calculations, Si would not have partitioned into the core of APB under such low temperature and high $f O_2$ conditions (Ziegler et al., 2010). Core-mantle differentiation is unable to explain the high $\delta^{30}$Si values of angrites compared to chondrites.

The correlation between $\delta^{30}$Si values and Mg/Si ratio in chondrites has led to the interpretation that the variation of $\delta^{30}$Si among planetary bodies is caused by nebular fractionation during forsterite condensation rather than core segregation (Fitoussi et al., 2009; Dauphas et al., 2015). Forsterite, with a Mg/Si ratio of ~2, is one of the earliest solid phase to condense from high temperature solar nebular, which was also abundant enough to alter the Mg/Si ratio in the protoplanetary disk. Yoneda and Grossman (1995) predicted that the nebular gas before forsterite condensation has a solar Mg/Si ratio of ~1.07. By the time forsterite finished condensing from the nebular gas, nearly all Mg and about half of Si was in forsterite, leaving the nebular gas with half of Si but depleted in Mg. The equilibrium fractionations between solid and gas during forsterite condensation were estimated to be +1.2 ‰ for $\delta^{26}$Mg and +2.3 ‰ for $\delta^{30}$Si, respectively (Méheut et al., 2009; Schauble, 2011). The CI chondrites are believed to be the closest representation of the solar Mg and Si isotopic composition, with $\delta^{26}$Mg = -0.27 ‰ and $\delta^{30}$Si = -0.44 ‰ (Fitoussi et al., 2009; Armytage et al., 2011; Teng et al., 2010; Zambardi et al., 2013). When forsterite is completely condensed from the nebular, equilibrium fractionation would have caused the isotopic compositions of both the solid and the remaining gas to be altered. Mass balance

calculation predicts that the solid forsterite would have $\delta^{30}$Si value of +0.71 ‰, while the remaining nebular gas has $\delta^{30}$Si value of -1.59 ‰. Since the solid and the gas have nearly equal amounts of Si, mixing of those two phases in different proportions during planetary formation would have resulted in a different $\delta^{30}$Si value in the solar system. As for Mg, since the condensation of forsterite retains almost all the Mg, mixing with the nebular gas has no impact on the $\delta^{26}$Mg values (Fig. 5.5). The nebular fractionation model successfully explains the variation of Mg/Si ratio and $\delta^{30}$Si value in meteorites, as well as the homogeneous stable Mg isotopic compositions (Dauphas et al., 2015).

### 5.4.3 Implications for the origin of NWA 7325

Oxygen isotope values of mineral separates from NWA 7325 follow mass-dependent fractionations, but $\Delta^{17}$O differs from those of Earth, Mars, or known asteroids, suggesting that it originated from a previously unsampled differentiated parent body (Jabeen et al., 2014; Kita et al., 2014). Bulk oxygen isotope compositions measured by previous studies showed that NWA 7325 are distinct from most achondrites groups, but in the range of ureilites (Irving et al., 2013; Jabeen et al., 2014; Barrat et al., 2015; Weber et al., 2016) (Fig. 5.6). But NWA 7325 displays drastically different texture compared to ureilites. In addition, Cr isotope compositions for NWA 7325 differs from that of ureilites and therefore preclude a genetic link with ureilites (Irving et al., 2013; Kita et al., 2014) (Fig. 5.7). Chronologic studies of NWA 7325 revealed a U-Pb age of 4563.4±2.6 Ma and an Al-Mg age of 4563.09±0.26 Ma (Koefoed et al., 2016). The ancient formation age indicates that NWA 7325 formed contemporaneously with many of the oldest achondrites, such as angrites,

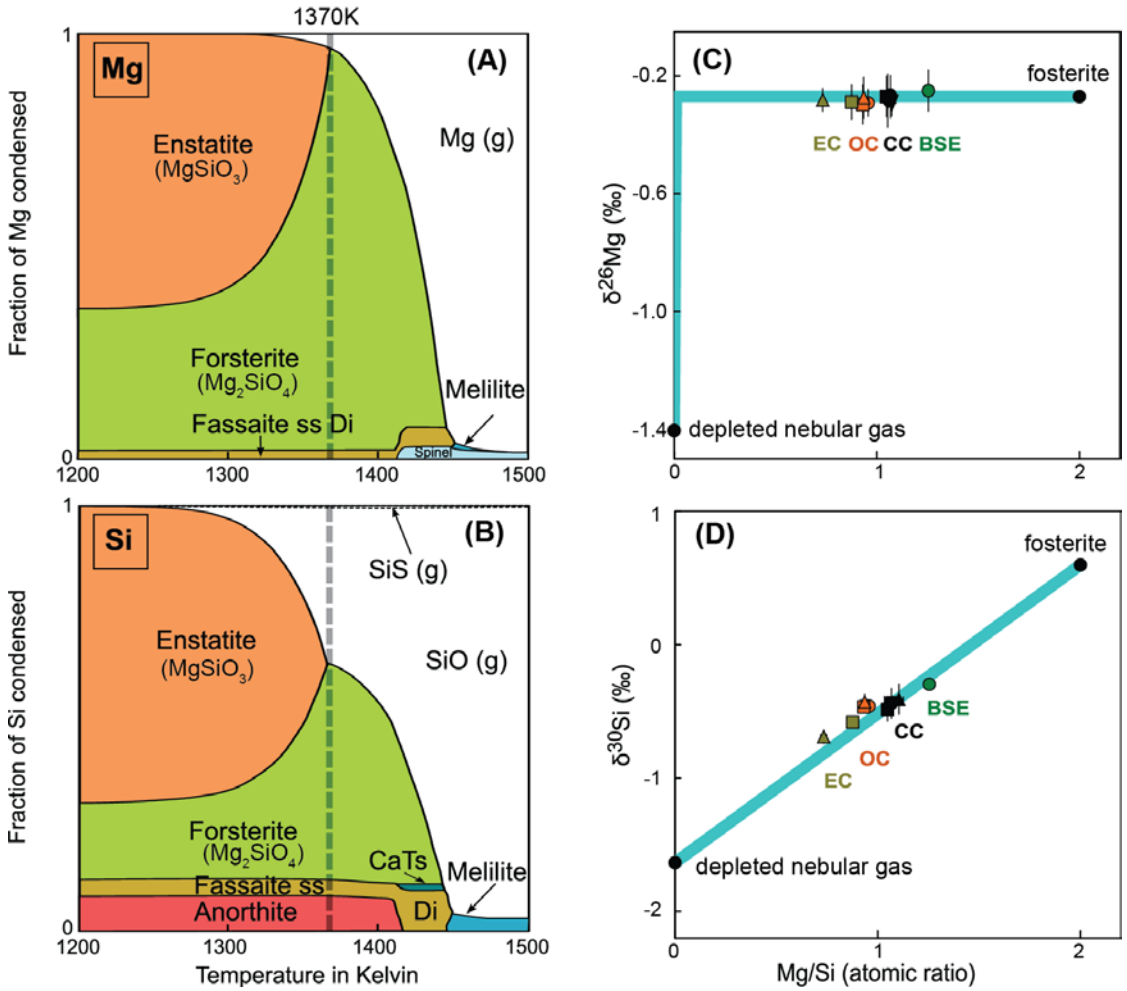


**Figure 5.5**: (A) and (B) show the distribution of Mg and Si between nebular gas and condensed phase with respect to temperature (in K) at a total pressure of $10^{-3}$ atm (reproduced after Davis and Richter, 2014). At high temperature, Mg and Si are in gas phase. Upon cooling, forsterite condensed and thereby lowers the Mg/Si ratio in the remaining nebular gas. At ~1370K, forsterite is fully condensed, leaving the gas with about half of Si and nearly no Mg. Fractionation and remixing of forsterite solid with the depleted nebular gas explains the the lack of it in $\delta^{26}$Mg values (C) and variations in $\delta^{30}$Si values (D) among inner solar system objects (reproduced after Dauphas et al., 2015). As a result of forsterite condensation and mixing with the gas, the Mg/Si ratio is well correlated with $\delta^{30}$Si values, which forms a well-defined mixing trend in planetary bodies.

which makes it highly unlikely to be originated from the evolved crust of a planetary-sized body (Dunlap et al., 2014). A recent study reported fractionated highly siderophile element (HSE) patterns of NWA 7325 relative to bulk chondrite; these data are interpreted to be the result of multi-stage metal-silicate partitioning on the parent body (Archer et al., 2015). NWA 7325 is extremely Fe poor and HSE depleted (Irving et al., 2013; Archer et al., 2015; Barrat et al., 2015), suggesting that its parent body may have experienced effective core formation. But metal-silicate differentiation did not shift its $\delta^{30}$Si composition from that of chondrites, suggesting that core segregation in the NWA 7325 parent body did not likely reach the pressure necessary for significant Si partitioning into the metal phase. This is in agreement with the low pressure metal-silicate partitioning model for HSE pattern of NWA 7325 (Archer et al., 2015). As demonstrated by Dauphas et al. (2015), metal-silicate differentiation on the APB is unlikely to be the cause of the heavy $\delta^{30}$Si compositions of angrites. The difference in $\delta^{30}$Si values between planetary materials could be caused by variable forsterite and nebular gas mixing. Higher fraction of forsterite mixing with the nebular gas during APB accretion may have caused the higher $\delta^{30}$Si values observed in angrites. In this scenario, the $\delta^{30}$Si values for NWA 7325 may indicate that it accreted from materials that inherited similar proportions of early gas and condensates as chondrites, ureilites, shergottites, and eucrites, most likely in the asteroid belt, but distinct from those of the angrite and aubrite parent bodies as well as the Earth-Moon system.

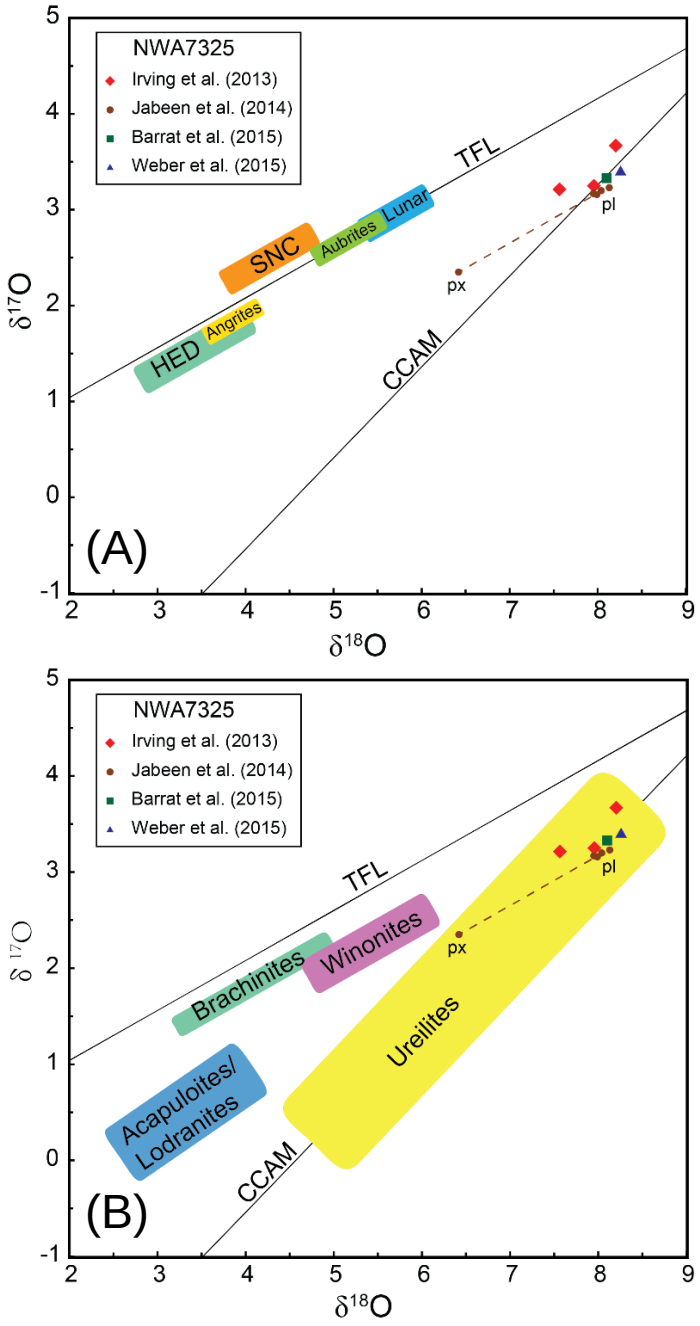


**Figure 5.6**: Oxygen isotope composition of NWA 7325 compared with differtiated achondrites (A) and primitive achondrites (B). Oxygen isotope values of mineral separates from NWA 7325 follow mass-dependent fractionations, but $\Delta^{17}O$ differs from those of Earth, Mars, or known asteroids, except for ureilites (Clayton and Mayede, 1996; Irving et al., 2013; Jabeen et al., 2014; Barrat et al., 2015; Weber et al., 2015), suggesting that it originated from a previously unsampled differentiated parent body (Jabeen et al., 2014; Kita et al., 2014).

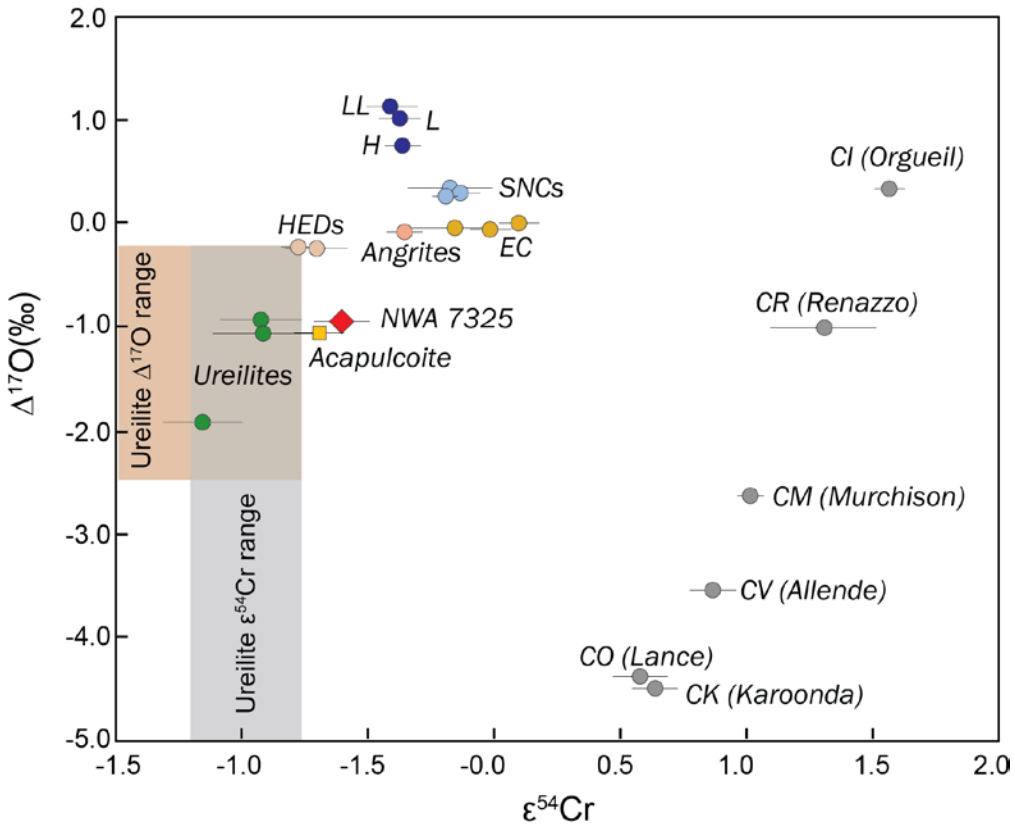


**Figure 5.7**: Cr isotope compositions for NWA 7325 differs from that of ureilites and therefore preclude a genetic link with ureilites (Irving et al., 2013; Kita et al., 2014). Figure modified after Kita et al. (2014).

## 5.5 Conclusions

NWA 7325 is a unique ungrouped achondrite that was thought to be possibly originated from Mercury. Stable Si isotopic compositions meteorites show that the $\delta^{30}$Si values for the inner solar system objects are heterogeneous. Angrites and BSE have higher $\delta^{30}$Si values than carbonaceous chondrites, whereas enstatite chondrites and aubrites have $\delta^{30}$Si values lower than carbonaceous chondrites. Martian meteorites and HEDs are essentially chondritic. NWA 7325 yielded a $\delta^{30}$Si value of -0.45±0.05 ‰, indistinguishable from that

of chondrite average, Martian meteorites and HEDs. The metal-silicate fractionation of Si isotopes during core formation is not believed to be responsible for the high $\delta^{30}$Si value in angrites and may only partially explain why BSE is high. The plausible explanation for the variations of Si isotopic compositions in meteorites is nebular fractionation during forsterite condensation. Forsterite is suggested to be the first solid to condense from the solar nebular, which significantly altered the Mg/Si ratio and $\delta^{30}$Si composition of the remaining nebular gas. Equilibrium fractionation during forsterite condensation can cause ~2.3 ‰ Si isotopic fractionation between solid and gas phases. Mixing between the forsterite and gas end-members can result in different $\delta^{30}$Si composition in planetesimals. The difference in $\delta^{30}$Si values between planetary materials could be caused by variable forsterite and nebular gas mixing. NWA 7325 has chondritic $\delta^{30}$Si values, which may suggest that it originated from materials that mixed similar proportions of early gas and condensates as chondrites, ureilites, Mars, and HED parent body, but distinct from those of the angrite and aubrite parent bodies as well as the Earth-Moon system.

# Summary and future work

The aims of this dissertation were to reappraise some of the potential matrix effects during Si isotope analysis, establish accurate and precise analytical routines, regardless of the sample matrix and apply it to both low and high temperature geochemistry.

By measuring well-characterized geologic reference materials and meteorite sample, it is confirmed that sulfur can cause significantly biased Si isotopic measurements. Results of pure Si standard solutions with addition of sulfate show shifts of up to +1.04±0.10‰ (2SD) in $\delta^{30}$Si values. Meteorite samples yield anomalous $\delta^{30}$Si values, which may be partially explained by the presence of sulfur. The experiments show that the precipitation of Fe hydroxide during sample preparation may be another process that causes shift in $\delta^{30}$Si values. A relative simple approach can eliminate the effects of sulfur and Fe hydroxide by a combination of sulfur-doping and careful pH adjustments. This technique ensures quantitative recovery of Si and also has the benefit of increasing Si ion intensity during MC-ICP-MS analysis. The modified method was proven to be suitable for S- and Fe-rich samples.

One of the goals of the dissertation was to better understand the mechanism of silicification in carbonate strata using a combination of Si isotope analysis and petrologic studies with a hope to better constrain the Si isotope fractionation factor in surface conditions. Authigenic megaquartz crystals collected from the Cretaceous Edwards Formation in central Texas provide such a unique opportunity to study these processes. The occurrence of anhydrite inclusions in megaquartz crystals implies that precipitation of quartz crystals took place after the primary calcite cementation and only partial dissolution of the

evaporite, probably during very early stages of diagenesis. *In situ* silicon isotope measurements from four megaquartz samples of the Edwards Formation showed a 6 ‰ range, from -2.90 to +2.94 ‰. This large range of $\delta^{30}$Si can be explained by a Rayleigh-type kinetic fractionation model, in which quartz precipitated from pore fluids that had an initial $\delta^{30}$Si value of -1.1 to -0.8 ‰. Calculations of the solubility ratio between amorphous silica and quartz suggest that silicification occurred at surface temperature (20-50°C). The fractionation factor of abiotic silica precipitation is estimated to be between -1.8 to -2.1 ‰, which is in strong agreement with previous estimates using natural silica samples. The source of Si is likely from the dissolution of amorphous opaline silica from sponge spicules. The estimated average $\delta^{30}$Si value of the Early Cretaceous seawaters in the study area is +2.7 to +3.0 ‰, significantly higher than the average of modern seawaters.

In addition to the application of Si isotopes in low temperature sedimentary realm, this dissertation also analyzed a number of meteorite samples, including a unique ungrouped achondrite NWA 7325 to help deciphering physical and chemical processes that occurred during the early solar system formation. The results show that the inner solar system objects are heterogeneous in terms of the $\delta^{30}$Si values. Angrites and BSE have higher $\delta^{30}$Si values than carbonaceous chondrites, whereas enstatite chondrites and aubrites have $\delta^{30}$Si values lower than carbonaceous chondrites. Martian meteorites and HEDs are essentially chondritic. NWA 7325 yielded a $\delta^{30}$Si value of -0.45±0.05 ‰, indistinguishable from that of chondrite average, Martian meteorites, and HEDs. The metal-silicate fractionation of Si isotopes during core formation is likely not responsible for the high $\delta^{30}$Si value in angrites and may only partially explain why BSE is high. The plausible explanation for

the variations of Si isotopic compositions in meteorites is nebular fractionation during forsterite condensation. Equilibrium fractionation during forsterite condensation can cause ~2.3 ‰ Si isotopic fractionation between solid and gas phases (Dauphas et al., 2015). Mixing between the forsterite and gas end-members can result in different $\delta^{30}$Si composition in planetesimals. The difference in $\delta^{30}$Si values between planetary materials could be caused by variable extents of forsterite and nebular gas mixing. The chondritic $\delta^{30}$Si values for NWA 7325 may imply that its parent body inherited similar proportions of mixed gas and condensates as chondrites, ureilites, Mars, and eucrites, whereas the angrite, aubrite and the Earth-Moon system originated from materials with different compositions.

There are several topics not covered at the time of this dissertation and have potential merits for future research. Interpretations of Si isotope signatures in Si-rich deposits rely on a well-characterized isotope fractionation factor. Experimental constraints on silicon isotope fractionation between precipitates and dissolved silica in fluids ($\Delta^{30}Si_{prec\text{-}diss}$) is still not well constrained. There is a large discrepancy between laboratory experiments and studies of natural samples. Additionally, studies have shown that the physicochemical properties of the solution in which the Si-bearing deposits precipitate have profound influence on isotope fractionation. The presence of Al hydroxides (Oelze et al., 2015) or Fe oxides (Delstanche et al., 2009) have been demonstrated to fractionate Si isotopes upon adsorption. Equilibrium Si isotope fractionations have been calculated using first principle simulations and the results show very limited fractionation at surface temperatures (Méheut et al., 2009; Dupuis et al., 2015). It is the kinetic effects that control the fractionation of Si isotopes between Si-rich deposits and it seems to be system dependent. Future work are

needed to simulate the natural environment conditions in laboratory experiments to further quantify the fractionation behavior of Si isotopes.

Another potential application of Si isotope is to test whether microbial activities facilitate the formation of siliceous deposits in hot spring. Previous interpretations of the hot spring deposits have assumed that the rocks have only been the product of straight physicochemical process such as evaporation, cooling, change in pH, and cation effects, i.e., abiotic precipitation (Guidry and Chafetz, 2002; Yee et al., 2003; Geilert et al., 2015). However, it has been well-documented that some biota do fractionate silica isotopes during precipitation of their hard parts, e.g., diatoms, sponges, and radiolarians (De La Rocha et al., 1997, 2000; De La Rocha, 2003; Hendry et al., 2010). Whether the microbes in the siliceous systems actively induce silica precipitation or passively act as nucleation sites remain an open question. It is likely that active induced precipitation will be accompanied with isotope fractionation. These studies will have significant implications for the study of silica deposits in the rock record.

# Appendix A

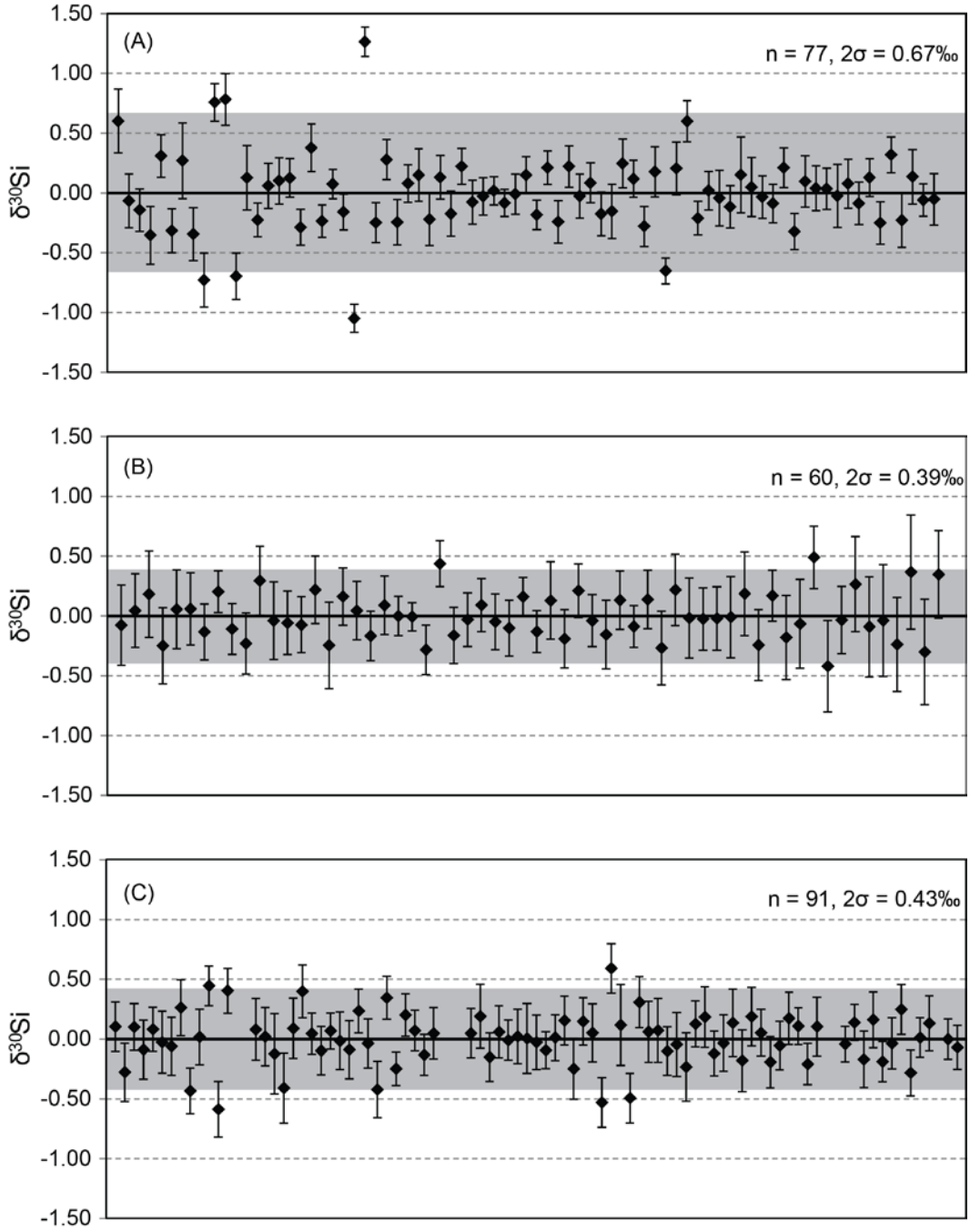


**Supplement Figure S1**: Long-term reproducibility of ±0.56 ‰ (2σ, n = 137) was obtained on CRQ standard (A) and (B) and of ±0.43 ‰ (2σ, n = 83) on MBQ (C) in three analysis sessions separated by 18 months.

# Appendix B

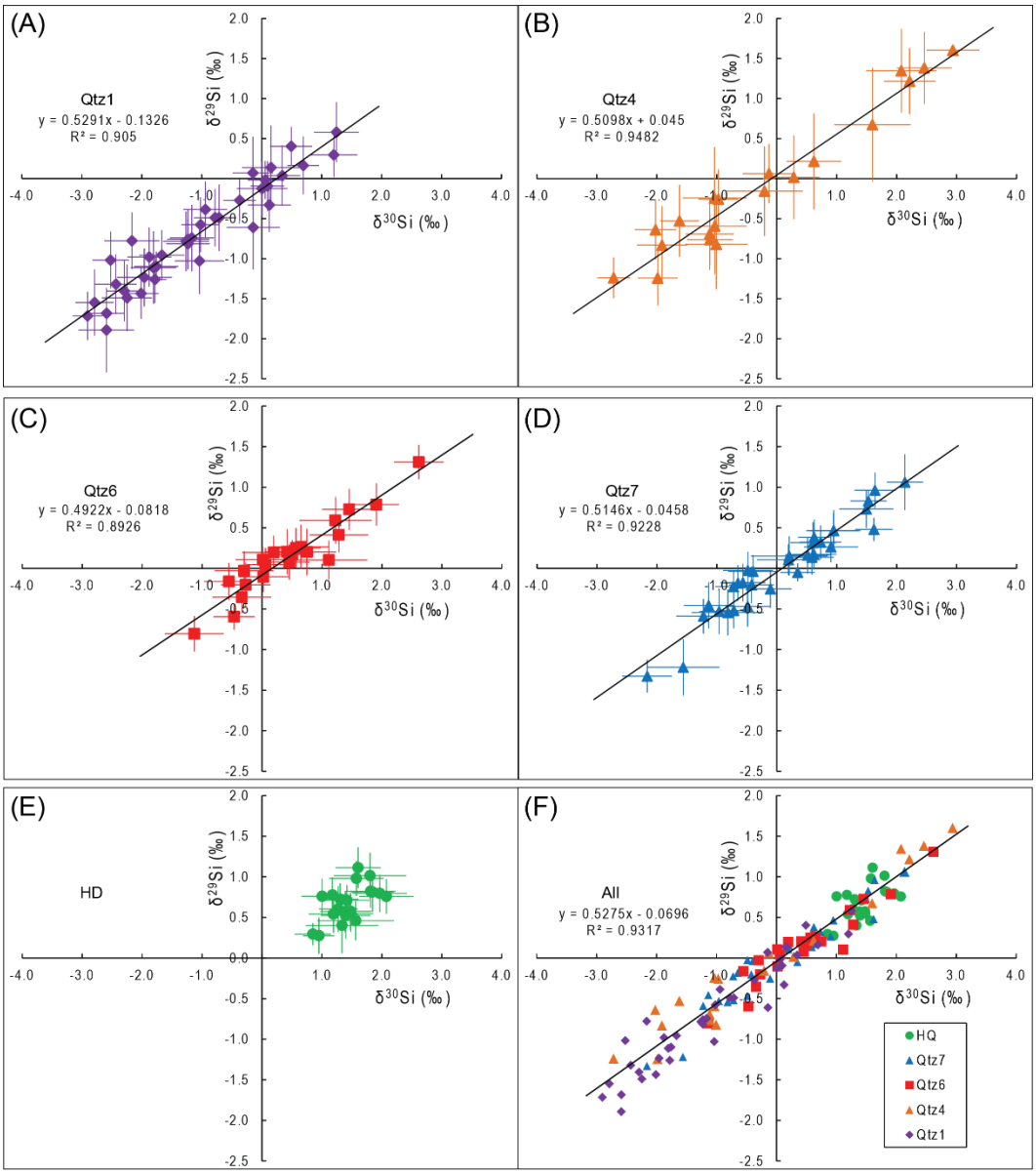


**Supplement Figure S2**: Three isotope ($^{28}Si$, $^{29}Si$, $^{30}Si$) plot for each of the four megaquartz samples (A) Qtz1; (B) Qtz4; (C) Qtz6; (D) Qtz7, and (E) Herkimer Diamond (HD) as well as the overall plot for all the data points (F). All data points in the four quartz grains follow a mass dependent fractionation line with an average slope of 0.528.

# References


Abraham, K., Opfergelt, S., Fripiat, F., Cavagna, A.J., de Jong, J. T. M., Foley, S. F., André, L. and Cardinal, D., 2008, $\delta^{30}Si$ and $\delta^{29}Si$ determinations on USGS BHVO-1 and BHVO-2 reference materials with a new configuration on a Nu Plasma Multi-Collector ICP-MS. Geostandards and Geoanalytical Research, v. 32, p. 193-202.

Alexander, G.B., 1954. The polymerization of monosilicic acid. Journal of the American Chemical Society, v. 76, p. 2094-2096.

Archer, G. J., Walker, R. J. and Irving, A. J., 2015. Highly siderophile element and $^{187}Re$-$^{187}Os$ isotopic systematics of ungrouped achondrite Northwest Africa 7325. 46$^{th}$ Lunar and Planetary Science Conference, Abstract #1987.

Armytage, R.M.G., Georg, R.B., Savage, P.S., Williams, H.M. and Halliday, A.N., 2011. Silicon isotopes in meteorites and planetary core formation. Geochimica et Cosmochimica Acta, v. 75, p, 3662-3676.

Armytage, R.M.G., Georg, R.B., Williams, H.M. and Halliday A.N., 2012. Silicon isotopes in lunar rocks: Implications for the Moon's formation and the early history of the Earth. Geochimica et Cosmochimica Acta, v. 77, p. 504-514.

Barrat, J.A., Greenwood, R.C., Verchovsky, A.B., Gillet, P., Bollinger, C., Langlade, J.A., Liorzou, C. and Franchi, I.A., 2015. Crustal differentiation in the early solar system: Clues from the unique achondrite Northwest Africa 7325 (NWA 7325). Geochimica et Cosmochimica Acta, v. 168, p. 280-292.

Basile-Doelsch, I., Meunier, J.D. and Parron, C., 2005. Another continental pool in the terrestrial silicon cycle. Nature, v. 433, p. 399-402.

Basile-Doelsch, I., 2006. Si stable isotopes in the Earth's surface: A review. Journal of Geochemical Exploration, v. 88, p. 252-256.

Benedix, G. K., McCoy, T. J., Keil, K. and Love, S. G., 2000. A petrologic study of the IAB iron meteorites: constraints on the formation of the IAB-Winonaite parent body. Meteoritics and Planetary Science, v. 35, p. 1127-1141.

Bustillo, M.A., 2010. Silicification of continental carbonates, in Alonso-Zarza, A. M. and Tanner, L. H. eds., Developments in Sedimentology, v. 62, Elsevier, p. 153-178.

Butler, G.P., 1969. Modern evaporite deposition and geochemistry of coexisting brines, the Sabkha, Trucial coast, Arabian Gulf. Journal of Sedimentary Research, v. 39, p. 70-89.

Cardinal, D., Alleman, L.Y., de Jong, J., Ziegler, K. and André, L., 2003. Isotopic composition of silicon measured by multicollector plasma source mass spectrometry in dry plasma mode. Journal of Analytical Atomic Spectrometry, 18, 213-218.

Chafetz, H.S. and Butler, J.C., 1980. Petrology of recent caliche pisolites, spherulites, and speleothem deposits from central Texas. Sedimentology, v. 27, p. 497-518.

Chafetz, H.S. and Zhang, J., 1998. Authigenic euhedral megaquartz crystals in a Quaternary dolomite. Journal of Sedimentary Research, v. 68, p. 994-1000.

Chakrabarti, R. and Jacobsen, S.B., 2010. Silicon isotopes in the inner Solar System: Implications for core formation, solar nebular processes and partial melting. Geochimica et Cosmochimica Acta, 74, 6921-6933.

Chakrabarti, R., Knoll, A.H., Jacobsen, S.B. and Fischer, W.W., 2012. Si isotope variability in Proterozoic cherts. Geochimica et Cosmochimica Acta, v. 91, p. 187-201.

Chen, X., Chafetz, H. S., Andreasen, R., and Lapen, T. J., 2016. Silicon isotope compositions of euhedral authigenic quartz crystals: Implications for abiotic fractionation at surface temperatures. Chemical Geology, v. 423, p. 61-73.

Chowns, T.M. and Elkins, J.E., 1974. The origin of quartz geodes and cauliflower cherts through the silicification of anhydrite nodules. Journal of Sedimentary Research, v. 44, p. 885-903.

Clayton, C.J., 1986. The chemical environment of flint formation in Upper Cretaceous chalk. In: The Scientific Study of Flint and Chert (eds. Sieveking, G.D.G. and Hart, M.B). Cambridge Cambridge University Press p. 43-54.

Clayton, R. N., 1993. Oxygen isotopes in meteorites. Annual Review of Earth and Planetary Science, v. 21, p. 115-149.

Clayton, R. N. and Mayeda, T. K., 1996. Oxygen isotope studies of achondrites. Geochimica et Cosmochimica Acta v. 60, p. 1999–2017.

Coplen, T.B., 2011. Guidelines and recommended terms for expression of stable-isotope-ratio and gas-ratio measurement results. Rapid Communications in Mass Spectrometry, v. 25, p. 2538-2560.

Collins, E.W., 2005. Geologic map of the west half of the Taylor, Texas, 30 X 60 minute quadrangle, University of Texas at Austin, Bureau of Economic Geology, Miscellaneous Map 43, scale 1:100,000

Dauphas, N., Poitrasson, F., Burkhardt, C., Kobayashi, H. and Kurosawa, K., 2015. Planetary and meteoritic Mg/Si and $\delta^{30}$Sivariations inherited from solar nebula chemistry. Earth and Planetary Science Letters, v. 427, p. 236-248.

Davis, A. and Richter, F., 2014. Condensation and evaporation of solar system materials. In: Meteorites and Cosmochemical Processes. Treatise on Geochemistry (2nd Edition), (eds. Holland, H. D. and Turekian, K.K), Elsevier, Oxford, pp.335–360.

De La Rocha, C.L., Brzezinski, M.A. and DeNiro, M.J., 1996. Purification, recovery, and laser-driven fluorination of silicon from dissolved and particulate silica for the measurement of natural stable isotope abundances. Analytical Chemistry, v. 68, p. 3746-3750.

De La Rocha, C.L., Brzezinski, M.A. and DeNiro, M.J., 1997. Fractionation of silicon isotopes by marine diatoms during biogenic silica formation. Geochimica et Cosmochimica Acta, v. 61, p. 5051-5056.

De La Rocha, C.L., Brzezinski, M.A. and DeNiro, M.J., 2000. A first look at the distribution of the stable isotopes of silicon in natural waters. Geochimica et Cosmochimica Acta, v. 64, p. 2467-2477.

De La Rocha, C.L., 2003. Silicon isotope fractionation by marine sponges and the reconstruction of the silicon isotope composition of ancient deep water. Geology, v. 31, p. 423-426.

De La Rocha, C.L. and Bickle, M.J., 2005. Sensitivity of silicon isotopes to whole-ocean changes in the silica cycle. Marine Geology, v. 217, p. 267-282.

Degens, E. T. and Epstein, S., 1962. Relationship between $O^{18}$ /$O^{16}$ ratios in coexisting carbonates, cherts, and diatomites. American Association of Petroleum Geologist Bulletin, v. 46, p. 534-542.

Delstanche, S., Opfergelt, S., Cardinal, D., Elsass, F., André, L. and Delvaux, B., 2009. Silicon isotopic fractionation during adsorption of aqueous monosilicic acid onto iron oxide. Geochimica et Cosmochimica Acta, v. 73, p, 923-934.

Demarest, M.S., Brzezinski, M.A. and Beucher, C.P., 2009. Fractionation of silicon isotopes during biogenic silica dissolution. Geochimica et Cosmochimica Acta, v. 73, p. 5572-5583.

Ding, S., Dasgupta, R., Lee, C.-T.A. and Wadhwa, M., 2015. New bulk sulfur measurements of Martian meteorites and modeling the fate of sulfur during melting and crystallization – Implications for sulfur transfer from Martian mantle to crust–atmosphere system. Earth and Planetary Science Letters, v. 409, p. 157-167.

Ding, T.P., Jiang, S.Y., Wan, D.F., Li, Y., Li, J., Song, H., Liu, Z. and Yao, X., 1996. Silicon Isotope Geochemistry. Geological Publishing House, Beijing, China. 125 p.

Ding, T.P., Ma, G.R., Shui, M.X., Wan, D.F. and Li, R.H., 2005. Silicon isotope study on rice plants from the Zhejiang province, China. Chemical Geology, v. 218, p. 41-50.

Ding, T.P., Gao, J.F., Tian, S.H., Wang, H.B. and Li, M., 2011. Silicon isotopic composition of dissolved silicon and suspended particulate matter in the Yellow River, China, with implications for the global silicon cycle. Geochimica et Cosmochimica Acta, v. 75, p. 6672-6689.

Douthitt, C.B., 1982. The geochemistry of the stable isotopes of silicon. Geochimica et Cosmochimica Acta, v. 46, p. 1449-1458.

Dunlap, D.R., Wadhwa, M. and Romaneillo, S.R., 2014. $^{26}$Al-$^{26}$Mg systematics in the unusual ungrouped achondrite NWA 7325 and the eucrite juvinas. 45$^{th}$ Lunar and Planetary Science Conference, Abstract #2186.

Dupuis, R., Benoit, M., Nardin, E. and Méheut, M., 2015. Fractionation of silicon isotopes in liquids: the importance of configurational disorder. Chemical Geology, v. 396, p. 239-254.

Engström, E., Rodushkin, I., Baxter, D.C. and Öhlander, B., 2006. Chromatographic Purification for the Determination of Dissolved Silicon Isotopic Compositions in Natural Waters by High-Resolution Multicollector Inductively Coupled Plasma Mass Spectrometry. Analytical Chemistry, v. 78, p. 250-257.

Erdman, M.E., Lee, C.-T.A., Yang, W. and Ingram, L., 2014. Sulfur Concentration in Geochemical Reference Materials by Solution Inductively Coupled Plasma-Mass Spectrometry. Geostandards and Geoanalytical Research, v. 38, p. 51-60.

Fisher, W. L. and Rodda, P. U., 1969. Edwards Formation (Lower Cretaceous), Texas: dolomitization in a carbonate platform system. American Association of Petroleum Geologist Bulletin, v. 53, p. 55-72.

Fitoussi, C. and Bourdon, B., 2012. Silicon isotope evidence against an enstatite chondrite Earth. Science, v. 335, p. 1477–1480.

Fitoussi, C., Bourdon, B., Kleine, T., Oberli, F. and Reynolds, B.C., 2009. Si isotope systematics of meteorites and terrestrial peridotites: implications for Mg/Si fractionation in the solar nebula and for Si in the Earth's core. Earth and Planetary Science Letters, v. 287, p. 77-85.

Folk, R. L. and Pittman, J. S., 1971. Length-slow chalcedony; a new testament for vanished evaporites. Journal of Sedimentary Research, v. 41, p. 1045-1058.

Fripiat, F., Cardinal, D., Tison, J.-L., Worby, A. and André, L., 2007. Diatom-induced silicon isotopic fractionation in Antarctic sea ice. Journal of Geophysical Research, v. 112, G02001.

Geeslin, J.H. and Chafetz, H.S., 1982. Ordovician Aleman ribbon cherts; an example of silicification prior to carbonate lithification. Journal of Sedimentary Research, v. 52, p. 1283-1293.

Geilert, S., Vroon, P.Z., Roerdink, D.L., Van Cappellen, P. and van Bergen, M.J., 2014. Silicon isotope fractionation during abiotic silica precipitation at low temperatures: Inferences from flow-through experiments. Geochimica et Cosmochimica Acta, v. 142, p. 95-114.

Geilert, S., Vroon, P.Z., Keller, N.S., Gudbrandsson, S., Stefánsson, A. and van Bergen, M.J., 2015. Silicon isotope fractionation during silica precipitation from hot-spring waters: Evidence from the Geysir geothermal field, Iceland. Geochimica et Cosmochimica Acta, v. 164, p. 403-427.

Georg, R.B., Reynolds, B.C., Frank, M. and Halliday, A.N., 2006. New sample preparation techniques for the determination of Si isotopic compositions using MC-ICPMS. Chemical Geology, v. 235, p. 95-104.

Georg, R.B., Halliday, A.N., Schauble, E.A. and Reynolds, B.C., 2007. Silicon in the Earth's core. Nature, v. 447, p. 1102-1106.

Georg, R.B., Zhu, C., Reynolds, B.C. and Halliday, A.N., 2009. Stable silicon isotopes of groundwater, feldspars, and clay coatings in the Navajo Sandstone aquifer, Black Mesa, Arizona, USA. Geochimica et Cosmochimica Acta v. 73, p. 2229-2241.

Gibson, E.K., Moore, C.B., Primus, T.M. and Lewis, C.F., 1985. Sulfur in Achondritic Meteorites. Meteoritics, v. 20, p. 503-511.

Greenwood, R. C., Franchi, I. A., Gibson, J. M. and Benedix, G. K., 2012. Oxygen isotope variation in primitive achondrites: the influence of primordial, asteroidal and terrestrial processes. Geochimica et Cosmochimica Acta, v. 94 p. 146–163.

Guidry, S.A. and Chafetz, H.S., 2002. Factors governing subaqueous siliceous sinter precipitation in hot springs: examples from Yellowstone National Park, USA. Sedimentology v. 49, p. 1253-1267.

Gunnarsson, I. and Arnórsson, S., 2000. Amorphous silica solubility and the thermodynamic properties of $H_4SiO_4$ in the range of 0° to 350°C at $P_{sat}$. Geochimica et Cosmochimica Acta, v. 64, p. 2295-2307.

Heck, P.R., Huberty, J.M., Kita, N.T., Ushikubo, T., Kozdon, R. and Valley, J.W., 2011. SIMS analyses of silicon and oxygen isotope ratios for quartz from Archean and Paleoproterozoic banded iron formations. Geochimica et Cosmochimica Acta, v. 75, p. 5879-5891.

Hendry, K.R., Georg, R.B., Rickaby, R.E.M., Robinson, L.F. and Halliday, A.N., 2010. Deep ocean nutrients during the Last Glacial Maximum deduced from sponge silicon isotopic compositions. Earth and Planetary Science Letters, v. 292, p. 290-300.

Hendry, K.R. and Robinson, L.F., 2012. The relationship between silicon isotope fractionation in sponges and silicic acid concentration: Modern and core-top studies of biogenic opal. Geochimica et Cosmochimica Acta, v. 81, p. 1-12.

Hesse, R., 1989. Silica diagenesis: origin of inorganic and replacement cherts. Earth-Science Reviews, v. 26, p. 253-284.

Hughes, H.J., Delvigne, C., Korntheuer, M., de Jong, J., André, L. and Cardinal, D., 2011. Controlling the mass bias introduced by anionic and organic matrices in silicon isotopic measurements by MC-ICP-MS. Journal of Analytical Atomic Spectrometry, v. 26, p. 1892-1896.

Iler, R.K., 1979. The chemistry of silica: solubility, polymerization, colloid and surface properties, and biochemistry. John Wiley, Chichester, 896 p.

Irving, A. J., Kuehner, S. M., Bunch,T. E., Ziegler, K., Chen, G., Herd, C. D. K., Conrey, R. M. and Ralew, S., 2013. Ungrouped mafic achondrite northwest Africa 7325: a reduced, iron-poor cumulate olivine gabbro from a differentiated planetary parent body. 44th Lunar and Planetary Science Conference, Abstract #2164.

Jabeen I., Ali, A., Banerjee, N. R., Osinski, G. R., Ralew, S. and DeBoer, S., 2014. Oxygen isotope compositions of mineral separates from NWA 7325 suggest a planetary (Mercury?) origin. 45th Lunar and Planetary Science Conference, Abstract #2215.

Janney, P.E., Richter, F.M., Mendybaev, R.A., Wadhwa, M., Georg, R.B., Watson, E.B. and Hines, R.R., 2011. Matrix effects in the analysis of Mg and Si isotope ratios in natural and synthetic glasses by laser ablation-multicollector ICPMS: A comparison of single- and double-focusing mass spectrometers. Chemical Geology, v. 281, p. 26-40.

Jones, L.H.P. and Handreck, K.A., 1963. Effects of Iron and Aluminium Oxides on Silica in Solution in Soils. Nature, v. 198, p. 852-853.

Kita, N.T., Sanborn, M. E., Yin, Q.-Z., Nakashima, D. and Goodrich, C. A., 2014. The NWA 7325 ungrouped achondrite - possible link to ureilites? Oxygen and chromium isotopes and trace element abundances. 45th Lunar and Planetary Science Conference, Abstract #1455.

Keil, K., 2010. Enstatite achondrite meteorites (aubrites) and the histories of their asteroidal parent bodies. Chemie der Erde - Geochemistry, v. 70, p. 295–317.

Keil, K., 2012. Angrites, a small but diverse suite of ancient, silica undersaturated volcanic–plutonic mafic mafic meteorites, and the history of their parent asteroid. Chemie der Erde - Geochemistry, v. 72, p. 191–218.

Knauth, L.P. and Epstein, S., 1976. Hydrogen and oxygen isotope ratios in nodular and bedded cherts. Geochimica et Cosmochimica Acta, v. 40, p. 1095-1108.

Knauth, L.P., 1979. A model for the origin of chert in limestone. Geology, v. 7, p. 274-277.

Knauth, L.P., 1994. Petrogenesis of chert. Reviews in Mineralogy and Geochemistry, v. 29, p. 233-258.

Knauth, L.P. and Lowe, D.R., 2003. High Archean climatic temperature inferred from oxygen isotope geochemistry of cherts in the 3.5 Ga Swaziland Supergroup, South Africa. Geological Society of America Bulletin, v. 115, p. 566-580.

Koefoed, P., Amelin, Y., Yin, Q.-Z., Wimpenny, J., Sanborn, M. E., Iizuka, T., and Irving, A. J. 2016. U-Pb and Al-Mg systematics of the ungrouped achondrite Northwest Africa 7325. Geochimica et Cosmochimica Acta, v. 183, p. 31-45.

Krot, A. N., Keil, K., Scott, E. R. D., Goodrich, C. A. and Weisberg, M. K., 2014. Classification of meteorites. In: Meteorites and Cosmochemical Processes. Treatise on Geochemistry (2nd Edition), (eds. Holland, H. D. and Turekian, K.K), Elsevier, Oxford, pp. 1-63.

Land, L.S., 1977. Hydrogen and oxygen isotopic composition of chert from the Edwards Group, Lower Cretaceous, Central Texas. Gulf Coast Association of Geological Societies Transactions, v. 27, p. 440-440

Li, Y., Ding, T. and Wan, D., 1995. Experimental study of silicon isotope dynamic fractionation and its application in geology. Chinese Journal of Geochemistry, v. 14, p. 212-219.

Mackenzie, F.T. and Gees, R., 1971. Quartz: Synthesis at Earth-surface conditions. Science, v. 173, p. 533-535.

Marin, J., Chaussidon, M. and Robert, F., 2010. Microscale oxygen isotope variations in 1.9 Ga Gunflint cherts: Assessments of diagenesis effects and implications for oceanic paleotemperature reconstructions. Geochimica et Cosmochimica Acta, v. 74, p.116-130.

Marin-Carbonne, J., Chaussidon, M. and Robert, F., 2012. Micrometer-scale chemical and isotopic criteria (O and Si) on the origin and history of Precambrian cherts: Implications for paleo-temperature reconstructions. Geochimica et Cosmochimica Acta, v. 92, p. 129-147.

Méheut, M., Lazzeri, M., Balan, E. and Mauri, F., 2009. Structural control over equilibrium silicon and oxygen isotopic fractionation: A first-principles density-functional theory study. Chemical Geology, v. 258, p. 28-37.

Milliken, K.L., 1979. The silicified evaporite syndrome; two aspects of silicification history of former evaporite nodules from southern Kentucky and northern Tennessee. Journal of Sedimentary Research, v. 49, p. 245-256.

Mittlefehldt, D.W., 2014. Achondrites. In: Meteorites and Cosmochemical Processes. Treatise on Geochemistry (2nd Edition), (eds. Holland, H. D. and Turekian, K.K), Elsevier, Oxford, pp. 235-266.

Mittlefehldt, D. W., Killgore, M. and Le,e M. T., 2002. Petrology and geochemistry of D'Orbigny, geochemistry of Sahara 99555, and the origin of angrites. Meteoritics and Planetary Science, v. 37, p. 345–369.

Mukherjee, D., Heggy, E. and Khan, S.D., 2010. Geoelectrical constraints on radar probing of shallow water-saturated zones within karstified carbonates in semi-arid environments. Journal of Applied Geophysics, v. 70, p. 181-191.

Nelson, H.F., 1973. The Edwards Reef Complex and associated sedimentation in Central Texas, Bureau of Economic Geology, University of Texas at Austin, Austin, Texas. 34 p.

Nielsen, S.G., Rehkämper, M., Baker, J. and Halliday, A.N., 2004. The precise and accurate determination of thallium isotope compositions and concentrations for water samples by MC-ICPMS. Chemical Geology, v. 204, p. 109-124.

Oelze, M., von Blanckenburg, F., Hoellen, D., Dietzel, M. and Bouchez, J., 2014. Si stable isotope fractionation during adsorption and the competition between kinetic and equilibrium isotope fractionation: Implications for weathering systems. Chemical Geology, v. 380, p. 161-171.

Opfergelt, S., de Bournonville, G., Cardinal, D., André, L., Delstanche, S. and Delvaux, B., 2009. Impact of soil weathering degree on silicon isotopic fractionation during adsorption onto iron oxides in basaltic ash soils, Cameroon. Geochimica et Cosmochimica Acta, v. 73, p. 7226-7240.

Pittman, J.S., Jr., 1959. Silica in Edwards Limestone, Travis County, Texas. SEPM Special Publication, v. 7, p. 121-134.

Pringle, E. A., Moynier, F., Savage, P.S., Badro, J. and Barrat, J.A., 2014. Silicon isotopes in angrites and volatile loss in planetesimals. Proceedings of the National Academy of Sciences, v. 111, p. 17029-17032

Reynolds, B.C., Aggarwal, J., André, L., Baxter, D., Beucher, C., Brzezinski, M.A., Engström, E., Georg, R.B., Land, M., Leng, M.J., Opfergelt, S., Rodushkin, I., Sloane, H.J., van den Boorn, S.H.J.M., Vroon, P.Z. and Cardinal, D., 2007. An inter-laboratory comparison of Si isotope reference materials. Journal of Analytical Atomic Spectrometry, v. 22, p. 561-568.

Reynolds, B.C., Georg, R.B., Oberli, F., Wiechert, U. and Halliday, A.N., 2006. Re-assessment of silicon isotope reference materials using high-resolution multi-collector ICP-MS. Journal of Analytical Atomic Spectrometry, v. 21, p. 266-269.

Righter, K., 2008. Siderophile element depletion in the angrite parent body (APB) mantle: due to core formation? 39th Lunar and Planetary Science Conferenc, Abstract #2164

Robert, F. and Chaussidon, M., 2006. A palaeotemperature curve for the Precambrian oceans based on silicon isotopes in cherts. Nature, v. 443, p. 969-972.

Roerdink, D.L., van den Boorn, S.H.J.M., Geilert, S., Vroon, P.Z. and van Bergen, M.J., 2015. Experimental constraints on kinetic and equilibrium silicon isotope fractionation during the formation of non-biogenic chert deposits. Chemical Geology, v. 402, p. 40-51.

Rose, P.R., 1972. Edwards Group, surface and subsurface, Central Texas, Report of Investigations 74, Bureau of Economic Geology, The University of Texas, Austin, Texas. 198 p.

Royse, C.F., Wadell, J.S., and Petersen, L.E., 1971. X-ray determination of calcite-dolomite: An evaluation. Journal of Sedimentary Research, v. 41, p. 483-488.

Rudnick, R. and Gao, S., 2014. Composition of the continental crust. In: The Crust. Treatise on Geochemistry (2nd Edition), (eds. Holland, H. D. and Turekian, K.K), Elsevier, Oxford, pp. 1-51.

Savage, P.S., Georg, R.B., Armytage, R.M.G., Williams, H.M. and Halliday, A.N., 2010. Silicon isotope homogeneity in the mantle. Earth and Planetary Science Letters, v. 295, p. 139-146.

Savage, P.S., Georg, R.B., Williams, H.M. and Halliday, A.N., 2013. The silicon isotope composition of the upper continental crust. Geochimica et Cosmochimica Acta, v. 109, p. 384-399.

Savage, P.S., Georg, R.B., Williams, H.M., Turner, S., Halliday, A.N. and Chappell, B.W., 2012. The silicon isotope composition of granites. Geochimica et Cosmochimica Acta, v. 92, p. 184-202.

Savage, P.S. and Moynier, F., 2013. Silicon isotopic variation in enstatite meteorites: Clues to their origin and Earth-forming material. Earth and Planetary Science Letters, v. 361, p. 487-496.

Schauble, E.A., 2011. First-principles estimates of equilibrium magnesium iso-tope fractionation in silicate, oxide, carbonate and hexaaquamagnesium (2+) crystals. Geochimica et Cosmochimica Acta, v. 75, p. 844–869.

Scholle, P.A. and Ulmer-Scholle, D.S., 2003. A Color Guide to the Petrography of Carbonate Rocks: Grains, Textures, Porosity, Diagenesis. American Association of Petroleum Geologist, Memoir v. 77, 474 p.

Scott, E.R., and Bottke, W.F., 2011. Impact histories of angrites, eucrites, and their parent bodies. Meteoritics and Planetary Sciences, v. 46, p. 1878–1887.

Sedaghatpour, F. and Teng, F.-Z., 2016. Magnesium isotopic composition of achondrites. Geochimica et Cosmochimica Acta, v. 174, p. 167-179.

Shahar, A. and Young, E.D., 2007. Astrophysics of CAI formation as revealed by silicon isotope LA-MC-ICPMS of an igneous CAI. Earth and Planetary Science Letters, v. 257, p. 497-510.

Siever, R., 1962. Silica solubility, 0°-200° C., and the diagenesis of siliceous sediments. The Journal of Geology, v. 70, p. 127-150.

Steinhoefel, G., Breuer, J., von Blanckenburg, F., Horn, I., Kaczorek, D. and Sommer, M., 2011. Micrometer silicon isotope diagnostics of soils by UV femtosecond laser ablation. Chemical Geology, v. 286, p. 280-289.

Teng, F.-Z., Li, W.-Y., Ke, S., Marty, B., Dauphas, N., Huang, S., Wu, F.-Y. and Pourmand, A., 2010. Magnesium isotopic composition of the Earth and chondrites. Geochimica et Cosmochimica Acta, v. 74, p. 4150-4166.

Tréguer, P., Nelson, D.M., Bennekom, A.J.V., DeMaster, D.J., Leynaert, A. and Quéguiner, B., 1995. The silica balance in the world ocean: A reestimate. Science, v. 268, p. 375-379.

van den Boorn, S.H.J.M., Vroon, P.Z., van Belle, C.C., van der, Wagt B., Schwieters, J. and van Bergen, M.J., 2006. Determination of silicon isotope ratios in silicate materials by high-resolution MC-ICP-MS using a sodium hydroxide sample digestion method. Journal of Analytical Atomic Spectrometry, v. 21, p. 734-742.

van den Boorn, S.H.J.M., van Bergen, M.J., Nijman, W. and Vroon, P.Z., 2007. Dual role of seawater and hydrothermal fluids in Early Archean chert formation: Evidence from silicon isotopes. Geology, v. 35, p. 939-942.

van den Boorn, S.H.J.M., Vroon, P.Z. and van Bergen, M.J., 2009. Sulfur-induced offsets in MC-ICP-MS silicon-isotope measurements. Journal of Analytical Atomic Spectrometry, v. 24, p. 1111-1114.

van den Boorn, S.H.J.M., van Bergen, M.J., Vroon, P.Z., de Vries, S.T. and Nijman, W., 2010. Silicon isotope and trace element constraints on the origin of ~3.5 Ga cherts: Implications for Early Archaean marine environments. Geochimica et Cosmochimica Acta, v. 74, p. 1077-1103.

Wasson, J.T. and Kallemeyn, G.W., 1988. Compositions of chondrites. Philosophical Transactions of the Royal Society of London. Series A, Mathematical and Physical Sciences, v. 325, p. 535-544.

Weber, I., Morlok, A., Bischoff, A., Hiesinger, H., Ward, D., Joy, K.H., Crowther, S.A., Jastrzebski, N.D., Gilmour, J.D., Clay, P.L. and Wogelius, R.A., 2015. Cosmochemical and spectroscopic properties of Northwest Africa 7325-A consortium study. Meteoritics and Planetary Science, v. 51, p. 3-30.

Weiss, B. P., Shuster, D. L., Gattacceca, J., Suavet, C. R., Irving, A. J. and Fu, R. R., 2013. A nonmagnetic differentiated planetary body. American Geophysical Union, Fall Meeting, Abstract #P51H-04

Wells, N.A., 1983. Carbonate deposition, physical limnology and environmentally controlled chert formation in Paleocene-Eocene Lake Flagstaff, central Utah. Sedimentary Geology, v. 35, p. 263-296.

Wetzel, F., de Souza, G.F. and Reynolds, B.C., 2014. What controls silicon isotope fractionation during dissolution of diatom opal? Geochimica et Cosmochimica Acta, v. 131, p. 128-137.

Woo, K.-S., Anderson, T.F., Railsback, L.B. and Sandberg, P.A., 1992. Oxygen isotope evidence for high-salinity surface seawater in the Mid-Cretaceous Gulf of Mexico: Implications for warm, saline deepwater formation. Paleoceanography, v. 7, p. 673-685.

Woodruff, C.M., Jr. and Foley, D., 1985. Thermal regimes of the Balcones/Ouachita trend, central Texas. Gulf Coast Associated Geological Societies Transactions, v. 35, p. 287-292.

Yee, N., Phoenix, R., Konhauser, K. O., Benning, L. G., and Ferris, F. G., 2003. The effect of cyanobacteria on silica precipitation at neutral pH: implications for bacterial silicification in geothermal hot springs. Chemical Geology, v. 199, p. 83-90.

Yoneda, S. and Grossman, L., 1995. Condensation of CaO MgO $Al_2O_3$ $SiO_2$ liquids from cosmic gases. Geochimica et Cosmochimica Acta, v. 59, p. 3413-3444.

Zambardi, T. and Poitrasson, F., 2011. Precise determination of silicon isotopes in silicate rock reference materials by MC-ICP-MS. Geostandards and Geoanalytical Research, v. 35, p. 89-99.

Zambardi, T., Poitrasson, F., Corgne, A., Méheut, M., Quitté, G. and Anand, M., 2013. Silicon isotope variations in the inner solar system: Implications for planetary formation, differentiation and composition. Geochimica et Cosmochimica Acta, v. 121, p. 67-83.

Zenger, D.H., 1976. Definition of type Little Falls Dolostone (late Cambrian), East-central New York. American Association of Petroleum Geologist Bulletin, v. 60, p. 1570-1575.

Ziegler, K., Young, E.D., Schauble, E.A. and Wasson, J.T., 2010. Metal–silicate silicon isotope fractionation in enstatite meteorites and constraints on Earth's core formation. Earth and Planetary Science Letters, v. 295, p. 487-496.